



Universiteit  
Leiden  
The Netherlands

## Photon detection at subwavelength scales

Wang, Q.

### Citation

Wang, Q. (2015, October 27). *Photon detection at subwavelength scales*. Retrieved from <https://hdl.handle.net/1887/35972>

Version: Not Applicable (or Unknown)

License: [Leiden University Non-exclusive license](#)

Downloaded from: <https://hdl.handle.net/1887/35972>

**Note:** To cite this publication please use the final published version (if applicable).

Cover Page



Universiteit Leiden



The handle <http://hdl.handle.net/1887/35972> holds various files of this Leiden University dissertation.

**Author:** Wang, Qiang

**Title:** Photon detection at subwavelength scales

**Issue Date:** 2015-10-27

# Photon Detection at Subwavelength Scales



# Photon Detection at Subwavelength Scales

Proefschrift

ter verkrijging van  
de graad van Doctor aan de Universiteit Leiden,  
op gezag van Rector Magnificus prof. mr. C.J.J.M. Stolker,  
volgens besluit van het College voor Promoties  
te verdedigen op dinsdag 27 oktober 2015  
klokke 11:15 uur

door

Qiang Wang

geboren te Dezhou (China)  
in 1985

Promotor: Prof. dr. E. R. Eliel  
Co-promotor: Dr. M. J. A. de Dood

Promotiecommissie: Prof. dr. A. Fiore  
(Technische Universiteit Eindhoven )  
Prof. dr. A. F. Koenderink  
(FOM-Instituut voor Atoom- en Molecuulfysica  
& Universiteit van Amsterdam)  
Prof. dr. M. Dogterom  
(Technische Universiteit Delft  
& Universiteit Leiden)  
Dr. J. J. A. Baselmans  
(Ruimteonderzoeksinstituut SRON  
& Technische Universiteit Delft)  
Prof. dr. E. J. J. Groenen  
Prof. dr. J. Aarts  
Prof. dr. M. P. van Exter

Casimir PhD series Delft-Leiden 2015-21  
ISBN 978-90-8593-229-1

The work described in this thesis is part of the research programme of the Foundation for Fundamental Research on Matter (FOM), which is part of the Netherlands Organization for Scientific Research (NWO).

Cover design by Jieke Lei.

*To my family and Lu Xun*



# Contents

<b>1</b>	<b>Introduction</b>	<b>1</b>
1.1	Single photons and single-photon detection . . . . .	1
1.2	Superconducting single-photon detectors . . . . .	3
1.3	Quantum detector tomography . . . . .	5
1.4	Photon detection mechanism of SSPDs . . . . .	7
1.5	Subwavelength microscopy with nano SSPDs . . . . .	9
<b>2</b>	<b>How Noise Affects Quantum Detector Tomography</b>	<b>13</b>
2.1	Introduction . . . . .	13
2.2	Experiment . . . . .	16
2.3	Quantum detector tomography . . . . .	17
2.4	Overall noise and tomography results . . . . .	20
2.5	Uncertainty budget . . . . .	24
2.6	Conclusions . . . . .	32
<b>3</b>	<b>Position-Dependent Detection Efficiency of a Single NbN Nanowire SSPD</b>	<b>35</b>
3.1	Introduction . . . . .	35
3.2	Separation of fit parameters . . . . .	37
3.3	Polarization-dependent IDE . . . . .	38
3.4	Optical absorption . . . . .	40
3.5	Position-dependent LDE . . . . .	43
3.6	Conclusions . . . . .	47
3.7	Appendix I: Photon detection mechanism . . . . .	48
3.8	Appendix II: Fit to visibility . . . . .	52
<b>4</b>	<b>Optimal Design of NbN Superconducting Single-Photon Detectors</b>	<b>55</b>
4.1	Introduction . . . . .	55
4.2	Photon detection process in SSPDs . . . . .	57
4.3	Optical absorption and detector response . . . . .	59

4.4	Results . . . . .	63
4.5	Conclusions . . . . .	68
<b>5</b>	<b>An Absorption-Based Superconducting Nanodetector as a Near-Field Optical Probe</b>	<b>71</b>
5.1	Introduction . . . . .	71
5.2	Scattering and absorption . . . . .	72
5.3	Dipole and nanodetector interaction . . . . .	76
5.4	Influence on the emitter . . . . .	80
5.5	Conclusions . . . . .	84
<b>6</b>	<b>Near-Field Single-Photon Detection in a Scattering SNOM</b>	<b>85</b>
6.1	Introduction . . . . .	86
6.2	Absorption spectrum . . . . .	88
6.3	$E$ -field enhancement by the bare tip . . . . .	89
6.4	Absorption of the nanowire with the tip . . . . .	91
6.5	Conclusions . . . . .	92
<b>7</b>	<b>Local Detection Efficiency of a NbN SSPD Explored by a Scattering SNOM</b>	<b>93</b>
7.1	Introduction . . . . .	93
7.2	Simulation configuration . . . . .	95
7.3	Enhanced electric field and absorption . . . . .	98
7.4	Local detection efficiency . . . . .	102
7.5	Detector response in an s-SNOM . . . . .	105
7.6	Conclusions . . . . .	109
	<b>Bibliography</b>	<b>111</b>
	<b>Summary</b>	<b>123</b>
	<b>Samenvatting</b>	<b>127</b>
	<b>List of publications</b>	<b>131</b>
	<b>Curriculum vitae</b>	<b>133</b>
	<b>Acknowledgement</b>	<b>135</b>

# Chapter 1

## Introduction

### 1.1 Single photons and single-photon detection

In classical theories light is considered to be an electromagnetic wave that interacts with matter by driving the electrons of the constituent atoms. Such a description that uses either classical optics, or Maxwell's equations is proven to be highly successful and is most often sufficient for practical applications. However, these classical theories have great difficulty in explaining the photoelectric effect originally described by H. Hertz in 1887 [1]. The photoelectric effect is the observation that electrons are ejected from a metal provided that the frequency of the light exceeds a certain threshold. An elegant explanation of this effect was given by A. Einstein in 1905 [2], proposing that light consists of discrete wave packets with an energy equal to  $\hbar\omega$ , where  $\omega$  is the angular frequency of the light and  $\hbar$  is the reduced Planck constant.

These wave packets or quanta of light are commonly called photons and, for visible light, carry a discrete amount of energy of the order  $10^{-19}$ J. This energy can be detected by extremely sensitive single-photon detectors that generate a “click” whenever detection takes place. The concept of photons as particles of light, the description of physical phenomena based on the statistical description of these particles and our ability to detect these particles with modern technology have lead to the development of the field of quantum optics. This field has been key to many scientific discoveries and has spawned multiple applications based on single-photon detector technology [3–5].

Our ability to detect single photons allows measuring light at extremely low levels, with applications in sensing [6], medical imaging [7], astronomy [8], thermal detection [9] and spectroscopy [10]. Naturally, it is extremely relevant when the quantum nature of light itself becomes important. For instance, the field of quantum information processing deals with the production, manipulation and detection of single photons with wide applications in quantum key

distribution [11] and quantum random number generators [12]. High-speed, efficient detectors with low electronic jitter and low noise or dark count rate are essential to the development of these applications.

Traditionally, photo-multipliers and semiconductor avalanche photodiodes have been used for single-photon detection [5,13]. More recently, thin superconducting nanowires have been developed as a novel platform for single-photon detection [14]. These superconducting single-photon detectors (SSPDs) have become the prime candidate for demanding single-photon counting applications, exhibiting dark count rates below  $10 \text{ s}^{-1}$  [15], electronic jitter below 20 ps [16], detection efficiencies of more than 90% [17] and an extremely broad spectral range, extending to  $\lambda = 5 \mu\text{m}$  [18]. In addition, with proper electronic design, an array of SSPDs can be used to achieve photon number resolution [19] or for camera applications [20,21].

Further technological improvements and use of these detectors require a better understanding of the photon-detection mechanism. Different detection models [14,22–25] have been introduced that all contain assumptions that may or may not be valid for a specific choice of wavelength and superconducting material. Comparison of these models with experimental data on technologically relevant devices is difficult because these devices are based on long, meandering wires that introduce potential problems, such as current crowding in bends [26], fabrication errors and/or inhomogeneity in the superconductor [27].

In this thesis we aim to study the detection mechanism of NbN SSPDs using a simple device structure. It consists of a short section of superconducting wire made by nanofabrication techniques. To analyze the process of photon detection and to separate the internal, microscopic, detection efficiency from optical coupling efficiency we make use of a technique known as quantum detector tomography [28,29] throughout this thesis. This method separates the response of the detector into distinguishable contributions of a well-defined photon number. Therefore we gain access to the energy or photon number dependence of the detection mechanism [30]. The wires studied in this thesis have typical dimensions that are smaller than the wavelength of light and hence the study of the details of the microscopic detection model takes place on a subwavelength scale.

Nano-sized SSPDs offer yet another new and exciting opportunity that is not possible with conventional detectors. Because of their nanoscale dimensions they can be used as a subwavelength probe in the optical near field to replace current near-field probes that all transport the radiation from the optical near field to a bucket style single-photon detector placed in the far field. A fundamental difference arises because the SSPD based probe is based on near-field absorption instead of scattering [31,32]. In the second part of this thesis we study the possibility of subwavelength near-field probing with an SSPD to either probe nanoscale emitters or to explore the physics of the detection

mechanism in a direct way using a near-field probe.

## 1.2 Superconducting single-photon detectors

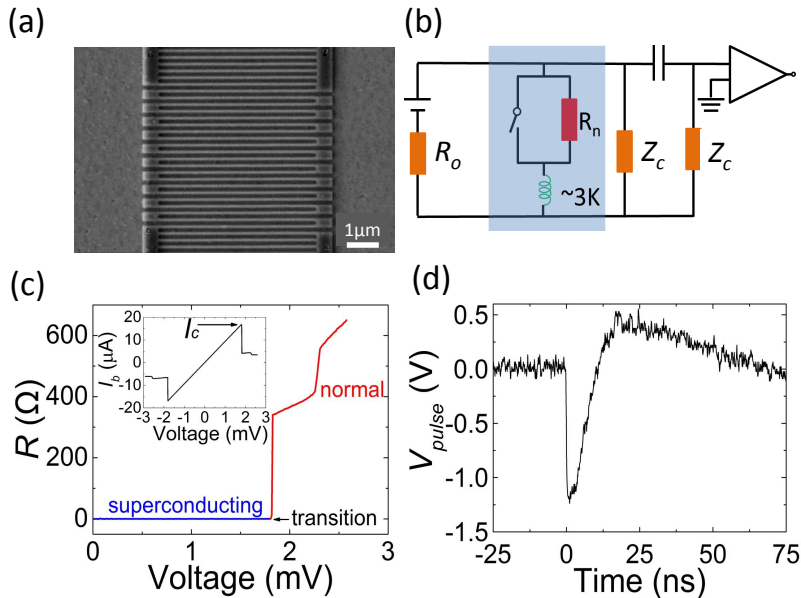


Figure 1.1: Various aspects of SSPDs. (a) shows an SEM image of a meandering NbN SSPD on a GaAs substrate. (b) shows a schematic of the measurement circuit. The resistor of  $R_o = 100 \Omega$  is used for limiting the bias current. The electric model of the SSPD is shown in the light-blue area, which corresponds to the cryostat at a temperature of  $\sim 3$  K. A photon detection event where the SSPD transits from the superconducting to the normal state after the absorption of a photon is equivalent to the switch going from closed to open. The bias current is diverted to  $Z_c = 50 \Omega$ , which is the impedance of the BNC cable. As a result, a voltage pulse is transmitted to the amplifier and recorded by an electronic counter (not shown) as a count. (c) shows the dependence of the resistance of the detector as a function of the driving DC voltage. The blue line and red step-like curve indicate the superconducting and normal states, respectively. The inset shows the bias current as a function of the voltage output, and the maximum point corresponds to the experimental critical current  $I_c$ . (d) shows a typical pulse with its polarity inverted after 60 dB amplification. The width of the pulse is about 5 ns and is limited by the detection electronics; this determines the reset time and maximum speed of the SSPD.

Throughout this thesis we use or investigate NbN SSPDs with the goal to gain a better understanding of photon detection at the nanoscale. These detectors consist of a thin and narrow strip of superconducting material to which a bias current is applied that is comparable to the critical current of the

device. Under those conditions absorption of the energy of a single photon is sufficient to drive the nanowire from the superconducting state to the normal state. Once the wire is in a resistive state a voltage difference over the wire is generated that can be amplified and read out with pulse counting electronics.

Figure 1.1 introduces the basic concepts of single-photon detection with an SSPD. An SEM image of a meandering wire on a GaAs substrate is shown in Fig. 1.1(a)<sup>1</sup>. The NbN film with a thickness of  $\sim 4$  nm is first grown on a GaAs substrate by DC magnetron sputtering. Afterwards, the  $\sim 100$  nm wide meandering wire is defined through a procedure of electron beam lithography followed by reactive ion etching. During the fabrication, a HSQ (Hydrogen silsesquioxane) layer with a thickness of  $\sim 80$  nm is left on the wire.

An equivalent electronic circuit that explains the electronic operation of an SSPD and the photon counting mechanism is depicted in Fig. 1.1(b). The part of the circuit enclosed in the light blue area represents the equivalent circuit of the detector and is kept at a temperature of  $\sim 3$  K, well below the transition temperature of the superconducting material ( $T_c \sim 10$  K for the thin NbN films used in this thesis). A constant bias current is supplied by the voltage source with a resistor  $R_0 = 100 \Omega$  in series. Figure 1.1(c) shows the measured resistance of the wire as a function of the applied voltage, showing the transition from the superconducting state to the resistive state. The inset shows the measured voltage as a function of bias current through the detector. The linear regime with a slope set by the resistor  $R_0$  corresponds to the superconducting state that survives until the device critical current  $I_c \approx 18 \mu\text{A}$ .

The equivalent circuit contains an inductance to represent the kinetic inductance of the current-carrying superconductor. Absorption of a photon that induces a transition from the superconducting state to the normal state is equivalent to opening of the switch to create a finite resistance value. The start of a resistive state of the current-carrying wire leads to additional Joule heating in the wire that drives part of the wire to the normal state with a resistance  $R_n$  of several  $\text{k}\Omega$ . Once the detector is resistive the current is diverted to the load (cable) impedance  $Z_c = 50 \Omega \ll R_n$  where a voltage pulse is generated that is amplified by the amplifier. The characteristic timescale for this process is set by  $L_k/R_n$ , where  $L_k$  is the kinetic inductance set by the geometry and material properties of the superconductor [33]. Since the current through the SSPD is now reduced, its Joule heating stops and the SSPD becomes superconducting again. The current in the wire returns at a timescale  $L_k/50\Omega$ . For typical device dimensions  $L_k \approx 100$  nH and the reset time of the detector is several nanoseconds.

A typical voltage pulse after amplification with a total gain  $g = 60$  dB is

---

<sup>1</sup>The sample and image are provided by Eindhoven University of Technology

shown in Fig. 1.1(d). The negative polarity is a consequence of the internal details of the amplifier. The AC coupled amplifier creates a pulse with a response time of  $\sim 5$  ns, which is limited by the speed of this detector-amplifier combination that couples the  $50 \Omega$  load impedance of the coaxial cable. It is important to note that most of the electric energy in the pulse is generated when the detector has returned to the superconducting state. This power is stored in the kinetic inductance of the superconductor. The energy in the pulse of Fig. 1.1(d) can be estimated as  $(1/g^2)(V_p^2/Z_c)\tau = 2.8 \times 10^{-16}$  J = 1750 eV, where  $g = 60$  dB =  $10^3$  is the total voltage gain of the amplifiers. This energy is  $10^3$  times larger than the energy stored in the photon and any information from the detection mechanism is erased in the process of generating the pulse. Chapters 3, 4 and 7 of this thesis aim to understand the detection mechanism in SSPDs and use different methods: quantum detector tomography in Chapters 3 and 4, and near-field optics in Chapter 7.

### 1.3 Quantum detector tomography

Significant progress towards understanding the detection mechanism of SSPDs has been made through quantum detector tomography (QDT) [28, 34]. This method characterizes the response of the detector in an agnostic way allowing for unbiased physical interpretation. QDT has been applied to retrieve the intrinsic quantum response of SSPDs to different photon numbers [29, 35–37], which allows us to unravel the physics of the detection mechanism [30, 38].

To perform QDT, the detector is illuminated using a set of coherent states of different average powers. In the experiment these states are obtained by attenuating the output of a pulsed laser. In this way the total detection probability as a function of average input power is recorded. An algorithm that takes into account the photon number distribution of the coherent states used to probe the detector converts this information to an internal detection efficiency expressed in the photon-number or Fock-state basis. This completely describes the detector.

For single-photon detectors with low efficiency, many parameters are needed to completely describe the response of the detector in the photon-number basis [28]. Finding the number-basis representation corresponds to an inversion of coherent state statistics from the measured count rates and is an intrinsically ill-conditioned problem [28, 34]. To overcome this problem some amount of smoothing or regularization needs to be applied to avoid that small fluctuations in the measured data lead to large changes in the characterization of the detector [28]. In this thesis we implement this smoothing by noting that an attenuated coherent state remains a coherent state with a lower average

photon number. We subsequently perform the tomography by separating the linear loss from the response in the number basis of photons absorbed by the detector instead of photons incident on the detectors [29].

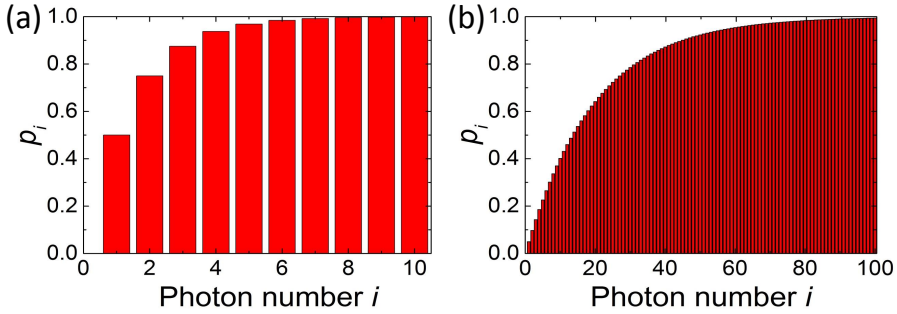


Figure 1.2: Detection probability  $p_i$  of an APD for  $i$  input photons. (a) and (b) show the probabilities that are required to describe the APD with values of single-photon detection efficiency  $p_1$  equal to 0.5 and 0.05, respectively.

To illustrate this modified scheme, let us consider two avalanche photodiodes (APDs)  $a$  and  $b$ . We assume that the internal detection efficiencies for single-photon detection are  $p_{a,1} = 0.5$  and  $p_{b,1} = 0.05$ , respectively. For APDs the multi-photon detection probability is known to be binomial [5, 13] and hence the detection probability for  $i$  photons is given by  $p_i = 1 - (1 - p_1)^i$ . The corresponding multi-photon detection probabilities are plotted in Fig. 1.2. Without prior knowledge of the operation of an APD (which is the purpose of QDT) about 10 probabilities  $p_i$  are needed to characterize the detector with 50% efficiency, while the 5% efficient detector requires 100 probabilities  $p_i$ . By factoring out the linear efficiency  $\eta$  in the modified tomography scheme we reduce the computational complexity from determining order  $\eta^{-1}$  parameters to less than 10 parameters.

The number of parameters that are needed to describe the operation of an SSPD depends on the experimental settings such as bias current and temperature. Noise in experimental data may reduce the amount of information that can be meaningfully extracted [34]. In Chapter 2 we investigate in detail the relation between the linear efficiency  $\eta$  and the internal detection efficiencies  $p_i$  for a meandering wire NbN SSPD and achieve an estimated relative uncertainty of 2%. We determine the influence of shot noise and four other technical noise sources on the outcome of quantum detector tomography, and we find that for long integration time ( $> 1$  s) shot noise in the measured count rates no longer dominates the accuracy.

## 1.4 Photon detection mechanism of SSPDs

The question of how photons are detected in SSPDs, and in NbN based SSPDs in particular, is a scientific question that has been investigated since the discovery of single-photon detection by an SSPD [14]. As an initial model, a “hotspot” has been introduced where a core of normal material is created that diverts the supercurrent around the normal-state material. As a result the current density locally exceeds the critical current density and a detection event occurs. While this detection model should prevail for very large excitation energies [39], experiments show that this model fails to explain data for photon energies of a few electron volts (visible and near-infrared wavelengths) [30]. Most notably, the hotspot model predicts a nonlinear energy-current relation and a sharp transition in the count rate as a function of bias current because detection events are impossible below a certain current density [40].

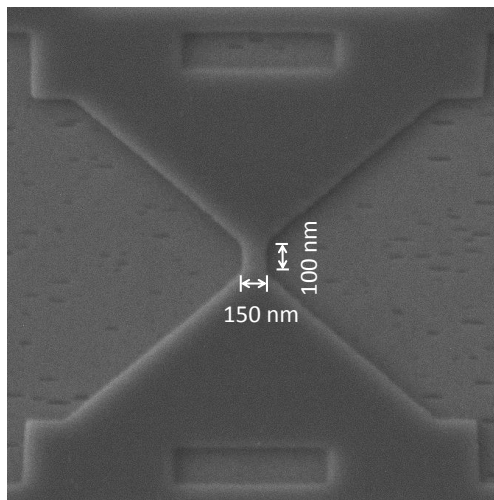


Figure 1.3: SEM image of a NbN single wire SSPD. A  $\sim 4$  nm thick, 150 nm wide and 100 nm long nanowire in between two tapered parts is fabricated on a GaAs substrate.

An important and open question in the field of SSPDs is thus the microscopic detection mechanism that causes photon detection. Understanding of the microscopic mechanism may help to design better detectors and is essential when operating these detectors in quantum-optical experiments. Various models have been proposed as an alternative to the hotspot model to describe the interaction between light and a current-carrying superconducting nanowire [22–25]. The challenge remains to perform experiments that either confirm or exclude a specific model. So far, a linear dependence of the internal detection efficiency  $p_i$  as a function of photon energy has been found for NbN detectors in the energy range from 0.7–8 eV [30]. These measurements use the

modified quantum detector tomography (as outlined in the previous section and Chapter **2** of this thesis) and are consistent with a detection model that involves photon-assisted vortex entry [25].

Our current understanding of the detection mechanism based on photon-assisted vortex entry implies that the response of the detector depends on the position where the photon has been absorbed. Controlled experiments with a simple detector geometry are needed to investigate the photon detection mechanism on the nanoscale. Figure 1.3 shows an SEM image of a short NbN single wire in between two tapered contact areas, nominally identical to the sample used in Chapter **3** of this thesis<sup>2</sup>. For this simple geometry, the active area is the short wire section and issues with current crowding due to bends [41] and inhomogeneities that reduce the critical current in a long wire [27] are largely avoided. As we show in Chapters **3** and **4** the optical response of this short section of wire is identical to that of the meander and can be calculated numerically using the known dielectric constant of NbN. Hence, tomography performed on this wire comprises a measurement of the linear, effective absorption efficiency  $\eta$  and the internal detection efficiencies  $p_i$ .

In Chapter **3** we demonstrate that the measured values of  $p_i$  together with the calculated electromagnetic field distribution in the wire comprise a method to experimentally probe the spatial variation in the detection efficiency within the wire. The field distribution in the wire is due to the properties of the material and boundary conditions depending both on polarization and wavelength of the incident light. Because the measured internal detection efficiencies depend on polarization of the incident light, this immediately implies that the internal efficiencies  $p_i$  are position dependent. We find that the edges of the wire are much more effective than the center, and that high detection efficiencies are achieved for distances  $\sim 30$  nm from the edge. Our result is logically consistent with the model of photon-assisted vortex entry [25].

To illustrate that the local detection efficiency determined in Chapter **3** is technologically relevant we calculate the polarization-dependent response of various meandering nanowire structures and compare these to experimental results from Anant et al. [42] in Chapter **4**. These calculations show that the internal detection efficiency of meandering wire structures is less than 100% for typical bias currents and wire widths used for state-of-the-art devices. The model detailed in Chapter **3** allows us to explain some intrinsic features that were hitherto not understood.

---

<sup>2</sup>The sample and image are provided by Eindhoven University of Technology

## 1.5 Subwavelength microscopy with nano SSPDs

Two essential experimental steps towards a detailed understanding of the photon detection event in SSPDs have been made in Chapters 2–4 of this thesis, namely the use of quantum detector tomography combined with the simplest possible detector geometry. Armed with the newly obtained knowledge, questions arise if these detectors can be probed via near-field scanning microscopy and whether the nanoscale detectors can be used as a near-field probe. We investigate these questions in detail in Chapters 5, 6 and 7.

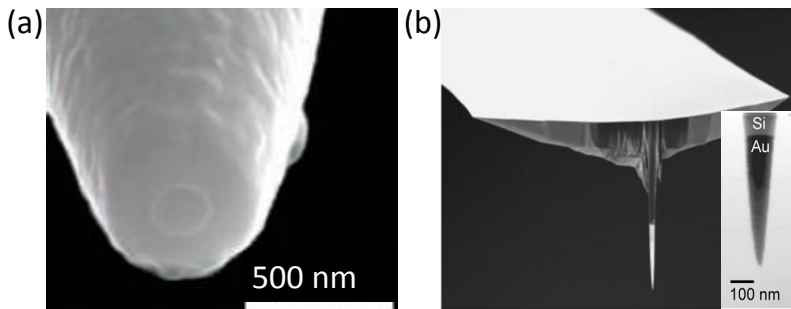


Figure 1.4: Two examples of SNOMs used by other groups. (a) shows the aluminum-coated probe of an aperture-SNOM [43]. The diameter of the aperture is about 200 to 230 nm. (b) shows the single gold tip attached to a silicon cantilever used in a scattering-SNOM [44].

Subwavelength imaging can be realized by scanning near-field optical microscopes (SNOMs), which beat the standard diffraction limit of conventional optical microscopes by scattering a small part of the optical near field to a large optical detector in the far field. Two methods for scattering the near field to a far-field detector have been developed. Figure 1.4(a) shows an example of an aperture based SNOM (a-SNOM) where light is scattered through an aperture into an optical fiber [45]. In the example, the fiber is coated with a 150 nm thick aluminum film and the subwavelength aperture has a diameter of 200–230 nm [43]. Figure 1.4(b) shows a tip on a cantilever used to realize what is called a scattering-SNOM (s-SNOM) [44]. The end of the sharp tip of a silicon cantilever is coated with gold (see inset of Fig. 1.4(b)). When illuminated from the side the optical response of this tip concentrates the electromagnetic field at the apex of the tip. When such a tip is placed in close vicinity of a sample, the optical near field is scattered by the tip and can be collected by a far-field detector.

Conventional SNOMs are intrinsically inefficient because they attempt to resolve subwavelength features using the physical mechanism of light scatter-

ing, which is characterized by strong size and wavelength dependence of the scattering efficiency. For scatterers much smaller than the wavelength, the Rayleigh limit applies and scattering cross section of the aperture or the tip apex is proportional to  $a^6/\lambda^4$ , where  $a$  is the size of the scatterer and  $\lambda$  is the wavelength of light [31]. A resolution of  $\sim \lambda/10$  requires  $a/\lambda \sim 0.1$ , lowering the efficiency of the detector per unit area by 4 orders of magnitude. This low efficiency severely limits the application of SNOMs to quantum optics because the optical loss associated with the low efficiency erases the underlying photon statistics of non-classical light [46].

In Chapter 5 we explore the possibility to use a nanoscale NbN SSPD as an efficient probe based on the experimental observation of a working detector of  $50 \times 50 \text{ nm}^2$  size. Because of the strongly absorbing nature of NbN material [47], characterized by the dominant imaginary part of the dielectric constant, this probe functions as a near-field absorber that is capable of detecting single photons. To estimate the performance of this novel near-field probe we calculate the interaction between a radiative dipole source and the detector. Both the detection efficiency and the influence on an emitter is compared to that of a SNOM probe made out of a well-conductive metal such as gold or silver. We find that the absorption cross section proportional to  $a^3/\lambda$  ( $a$  is the dimension of the nanoscale SSPD) is at least two orders of magnitude higher than the scattering cross section in SNOMs while the influence on the properties of the emitter are less than that of conventional SNOMs.

To directly measure the nanoscale response of an SSPD with the aim to independently confirm the detection model we design a scattering tip based SNOM. The design of the scattering tip above the NbN detector is detailed in Chapter 6 that discusses the influence of the tip geometry on the localization of field at the tip apex. The field localization of a tip with finite length is due to a plasmonic resonance in combination with a singularity or lightning-rod effect at the apex [48, 49]. We determine the role of this resonance in the absorption of the detector and determine the perturbing effect of a resistive load due to the detector in the near field of the antenna (tip). We find that the absorption of the detector as a function of wavelength is qualitatively similar to the field enhancement calculated for a tip without detector if the distance between tip and sample is comparable to the radius of curvature of the tip apex.

To resolve the local detection efficiency, an s-SNOM with a spatial resolution better than  $\sim 30 \text{ nm}$  needs to be designed based on the results of Chapter 4. This resolution is outside the regime of conventional aperture based SNOMs because this length scale is smaller than twice the skin depth in metals used as a cladding material of the fiber tip. Calculations in Chapter 7 show that a realistic design of a tip leads to an s-SNOM with the desired resolution and we calculate the expected response of the detector when illuminating the tip-detector system from the side. We observe that the detector response exhibits

two narrow peaks on the edge of the nanowire due to the distribution of both optical absorption and internal detection efficiency near the edges. Realizing this configuration in an actual experiment will give valuable information on the detection mechanism, and holds promise for new applications in near-field optics. For instance a nanodetector that is efficiently coupled to a tip could be used as an efficient multi-photon detector that samples the statistics of various quantum states of light.



## Chapter 2

# How Noise Affects Quantum Detector Tomography

We determine the full photon number response of a NbN superconducting nanowire single-photon detector via quantum detector tomography, and the results show the separation of linear, effective absorption efficiency from the internal detection efficiencies. In addition, we demonstrate an error budget for the complete quantum characterization of the detector. We find that for short times, the dominant noise source is shot noise, while laser power fluctuations limit the accuracy for longer timescales. The combined standard uncertainty of the internal detection efficiency derived from our measurements is about 2%<sup>1</sup>.

### 2.1 Introduction

The detection of single photons plays an important role in quantum optics [3] and quantum key distribution [50]. Superconducting single-photon detectors (SSPDs) for near-infrared wavelengths are promising because they combine high detection efficiency and high speed. In particular SSPDs made out of NbN and related materials have received a lot of attention because these detectors can be operated at relatively high temperatures of  $\sim 4$  K. Moreover, these detectors are technologically interesting due to a combination of high speed, low dark count rate, low jitter and high detection efficiency [17]. Typically, the detection efficiency and dark count rate are determined through

---

<sup>1</sup>Q. Wang, J. J. Renema, A. Gaggero, F. Mattioli, R. Leoni, M. P. van Exter, and M. J. A. de Dood, accepted by J. Appl. Phys. for publication.

measurement of the count rate as a function of the incident photon flux and detector bias current.

Further progress on characterizing SSPDs for applications in quantum optics can be made by using quantum detector tomography (QDT) [28, 34, 51–53] as a method to retrieve the complete quantum response of the detector. This assumption-free method is based on the calculation of the Positive Operator Valued Measure (POVM) [28, 34, 51–53], which mathematically determines the operator  $\{\Pi_{click}\}$  of the detector. The probability of a click event is expressed as:

$$R_{click} = \text{Tr}(\rho \Pi_{click}), \quad (2.1)$$

where  $\rho$  is the density matrix that describes the input state. Usually well-defined coherent states from a laser are used as probe states. Coherent states are a linear combination of photon number states (i.e., Fock states) with  $\rho = |N\rangle\langle N|$  and  $|N\rangle = \sum_{i=0}^{\infty} N^{\frac{i}{2}} \exp(-\frac{N}{2}) / \sqrt{i!} |i\rangle$  ( $N$  is the mean photon number of the coherent state and  $i$  indexes the photon number). In the basis of photon number states, the operator of the detector is written as  $\{\Pi_{click}\} = \sum_{i=0}^{\infty} \tilde{p}_i |i\rangle\langle i|$ , where  $\tilde{p}_i$  is the probability of a click event caused by an input photon number state  $|i\rangle$ . Because the detection is not phase-sensitive a description with only the diagonal elements of the POVM suffices. The description of SSPDs is further simplified by the fact that these detectors produce a binary response of “click” or “no-click” that does not contain information about the number of photons. We calculate first the no-click probability and then compute the click probability for a coherent state as [29, 36]:

$$\begin{aligned} R_{click}(N) &= 1 - R_{no-click}(N) \\ &= 1 - e^{-N} \sum_{i=0}^{\tilde{m}} (1 - \tilde{p}_i) \frac{(N)^i}{i!}. \end{aligned} \quad (2.2)$$

Equation (2.2) includes an assumption supported by experimental observations that at high input power the detector saturates with  $\tilde{p}_i = 1$  for  $i > \tilde{m}$ . For detectors with very low optical coupling efficiency  $\eta$ , Eq. (2.2) involves a large number of parameters  $\tilde{p}_i$ , i.e., of order  $\eta^{-1}$  for an ideal single-photon detector.

In our experiment we illuminate a meandering SSPD with an active area of  $5 \times 5 \mu\text{m}^2$  with a  $\sim 200 \mu\text{m}$  diameter optical beam, and we estimate an optical coupling efficiency  $10^{-3}$ . Consequently, we would have to determine  $10^3$  parameters  $\tilde{p}_i$ , making standard detector tomography an unrealistic task. This difficulty can be partly resolved by introducing a smoothing of adjacent  $\tilde{p}_i$ , through Tikhonov regularization [28] to effectively reduce the number of independent parameters. For very small values of optical coupling efficiency

the effect of this regularization becomes more prominent and complicates the interpretation of tomography. To alleviate these problems, we replace the mean photon number in the input beam  $N$  by the mean number of absorbed photons  $\eta N$ , and replace Eq. (2.2) by [29]

$$R(N) = 1 - e^{-\eta N} \sum_{i=0}^m (1 - p_i) \frac{(\eta N)^i}{i!}, \quad (2.3)$$

where  $\eta$  is interpreted as the effective absorption efficiency to describe the optical coupling process, and the parameters  $p_i$  now have the significance of representing the internal detection efficiency that an absorbed photon number state  $|i\rangle$  causes a click. The sum of Eq. (2.3) has much fewer terms and it is possible to obtain the values of  $p_i$  by performing a relatively simple experiment.

The introduction of Eq. (2.3) does not result in a loss of generality because all solutions to Eq. (2.2) are solutions to Eq. (2.3) for  $\eta = 1$ . Cases with  $\eta \neq 1$  result in an overdetermined system, where an additional assumption has to be invoked to identify the solution of physical significance. In this case, we use the sparsity in the  $p_i$  to select the solution which has the fewest  $p_i \neq 1$ . We note that  $\eta$  and  $p_1$  are separable in the experiment [35] due to the fact that  $\eta$  enters into the detection probability of higher-order photon numbers. This modified tomography procedure is particularly well suited for detectors where  $\eta \ll 1$  [29] and has been used to study the intrinsic quantum response of SSPDs to different photon number [29, 35–37] and to study the physics of the detection mechanism [30, 38].

In the experiment, the detector is illuminated with laser pulses that each contains a coherent state of light. The total detection probability is recorded as a function of average input power, which is proportional to the average photon number. Based on Eq. (2.3), an algorithm that takes into account the photon number distribution of the input states can be used to convert this information to an internal detection efficiency  $p_i$  in the photon number basis, which completely describes the detector.

The amount of information that can be extracted via tomography depends critically on the accuracy with which it is performed. For short measurement times the measured photon count rates show fluctuations that define a fundamental lower limit to the accuracy of the tomography. It is thus a natural question to ask how accurate QDT is in this limit and what other experimental factors limit the accuracy. A first estimate of the error in the nonlinear response of NbN superconducting detectors is reported in Ref. [30], and a calibration of the overall detection probability of an SSPD at high bias currents is reported in Ref. [54]. However, a discussion on the nature of the noise sources and how each of these sources affects the nonlinear detection probabilities determined by tomography has not been given.

In this chapter, we investigate the accuracy of quantum detector tomography on a meandering NbN SSPD. We consider five experimental factors: shot noise, fluctuations in laser power, non-linearities in the optical power meter, and fluctuations in bias current and temperature. We compare experimental results to synthesized data in order to systematically analyze how each noise factor influences QDT. By quantifying every type of noise in the measurement we calculate the combined uncertainty of the QDT results.

This chapter is structured as follows: Sections 2.2 and 2.3 describe the experiment and the method of quantum detector tomography, respectively. Section 2.4 contains the experimental results of QDT on an SSPD. In Section 2.5 we perform simulations to unravel the contribution of each noise source to QDT.

## 2.2 Experiment

The SSPD in this study is made out of a 4.5 nm thick NbN film deposited on a silicon substrate with a 254 nm thick layer of thermally grown SiO<sub>2</sub>. The NbN film is fabricated into a 100 nm wide, meandering wire, with 150 nm spacing between the wires (fill factor is 40%). The total active area of the device is  $5 \times 5 \mu\text{m}^2$ . The SiO<sub>2</sub> layer serves as a  $\lambda/4$  cavity optimized for 1550 nm wavelength. The critical current  $I_c$  of this device is measured to be  $23.5 \pm 0.5 \mu\text{A}$  at a temperature of 3.2 K corresponding to a critical current density  $j_c \approx 5.2 \times 10^6 \text{A}/\text{cm}^2$ .

The detector is mounted in a pulse-tube cryostat with free-space optical access (PRO-K-0274-00, Entropy GmbH), and is cooled down to a base temperature of 3.2 K. A bias current  $I_b$ , which is a significant fraction of the critical current  $I_c$  of the detector, is applied using a voltage source (Yokogawa GS200) with a 100  $\Omega$  resistor in series with the detector to convert the applied voltage to a bias current. Voltage pulses, which correspond to detection events, are collected via the high-frequency port of a bias-T (Minicircuits ZNBT-60-1W+) and are amplified via a cascade of high-frequency amplifiers ( $3 \times$  Minicircuits ZX60-3-18G+, 60 dB total amplification). The resulting pulses are sent to a pulse counter (Agilent 53131A).

To measure the detector response, the detector is illuminated in free space with picosecond laser pulses at a wavelength of  $\lambda = 1200 \text{nm}$  from a spectrally filtered supercontinuum laser with a repetition rate of 20 MHz (Fianium FP 1060). For free-space illumination, the optical coupling efficiency (i.e., effective absorption efficiency  $\eta$ ) is mainly determined by the alignment and the ratio of the area of the meandering wire to the light spot size (diameter of  $\sim 200 \mu\text{m}$ ). The large beam diameter eliminates mechanical vibrations and drift of the optical alignment, but compromises the optical coupling efficiency

$\eta$ . We find that these effects are more important than the dependence of  $\eta$  on wavelength due to the enhanced absorption by the cavity resonance. We select the wavelength of 1200 nm rather than the preferred 1550 nm to achieve larger  $\eta$  and focus on the internal detection efficiency  $p_i$  for physical interpretation.

To filter the incident light we use a combination of a long pass filter, that transmits wavelengths beyond 1000 nm, and a band pass filter for 1200 nm wavelength light with a full-width-at-half-maximum of 10 nm. The mean photon number per pulse can be varied by rotating a half-wave plate placed in between two crossed polarizers. In this way, we tune the laser power (25 points) by a factor of  $\sim 600$  between the maximum and minimum while keeping the polarization of the incident light on the detector unaltered [42]. The observed count rate is recorded as a function of the mean photon number per pulse and bias current from  $6.5 \mu\text{A}$  to  $16.8 \mu\text{A}$ . At low bias current compared to the critical current, one can obtain the nonlinear response of the detector with relative ease. In these experiments we observe no dark count events in one second (i.e., dark count rate  $< 1$  Hz) up to the highest applied bias current of  $16.8 \mu\text{A}$ ; therefore, we neglect dark count rate for all bias currents. In order to investigate the influence of noise on QDT and to discriminate between shot noise and technical noise, we measure the count rate in 1000 consecutive intervals of 0.1 second at each setting of the optical power and bias current. This allows us to vary the integration time per point by averaging the data after the measurement.

## 2.3 Quantum detector tomography

The purpose of tomography is to find the detection probability expressed in the photon number basis. We apply the detector tomography protocol that was originally demonstrated in Ref. [28] with the modifications proposed in Ref. [29] for low system detection efficiency (see Eq. (2.3)). In the experiment, the number of detection events is recorded as a function of the mean number of photons per pulse, which is directly given by the average intensity of the laser and can be measured to a high degree of accuracy with a conventional power meter. Next, the tomography algorithm is applied, which processes the measured count rates to find a precise detector response as detection efficiencies expressed in the photon number basis.

In addition, in order to verify the separation of the effective absorption efficiency  $\eta$  and the internal detection efficiency  $p_i$ , we use two different settings of the input laser power, referred to as high power and low power. The low power was obtained by attenuating the high power using a neutral density filter that lowers the average power on the detector by a factor 2.51. The idea is that, according to the interpretation of Eq. (2.3), if the QDT for the data

(measured  $R$ ) with low laser power is performed by using the reference laser power before the attenuator (i.e., values of high power), the attenuation factor in the beam path will be attributed to the effective absorption efficiency  $\eta$  and will not affect the internal detection efficiency  $p_i$ .

Figure 2.1(a) shows a set of representative data used in tomography for both high and low laser power. Count rates are shown as a function of mean photon number per pulse for the two different input settings (solid curves for high power and dashed curves for low power); they are represented as a detection probability  $R$  by normalizing the count rate to the laser repetition rate (20 MHz). The mean photon number per pulse for the two settings of the laser power is calculated as  $N = P_L/(\hbar\omega f)$ , where  $P_L$  is the high or the low laser power,  $\omega$  is the angular frequency of the light at wavelength of 1200 nm, and  $f$  is the laser repetition rate. The total data set comprises measurements at 57 different bias currents. For clarity, we only plot the data for 4 bias currents in Fig. 2.1(a).

The data in Fig. 2.1(a) shows that the detector response is determined by both the bias current and the mean photon number  $N$ . The straight line with slope of 1 in the log-log plot for high bias currents (14.40  $\mu\text{A}$  and 16.05  $\mu\text{A}$ ) indicates that the detector behaves as a linear detector that saturates at large values of the mean photon number. When biased with a lower current, the detector shows a lower detection probability that increases more than linearly with mean photon number. A direct way to make this visible is by calculating the slope of the detection probability on a log-log scale as shown in Fig. 2.1(b).

At the highest bias current (16.05  $\mu\text{A}$ ) this slope is less than or equal to 1 and tends to 0 due to saturation of the detector at large  $N$ . For a lower bias current (14.40  $\mu\text{A}$ ), the detector response increases more than linearly for  $N > 10^2$  and then saturates. The higher-order nonlinear response is more prominent at the lower bias currents (8.48  $\mu\text{A}$  and 11.26  $\mu\text{A}$ ), where the derivative exceeds 2. Investigating these derivatives is a coarse method to identify the photon number response, from which it is not possible to quantify the probability to detect 1, 2 or 3 photons.

To quantify these probabilities, we implement the tomography as discussed in the Introduction to yield the values of effective absorption efficiency  $\eta$  and internal detection efficiency  $p_i$  of the measured detector. We fit Eq. (2.3) to the power dependent data at each current, and repeat the non-linear least-squares fitting procedure for different values of maximum photon number  $m$ . To determine the quality of the fit we calculate the reduced chi-squared  $\chi^2 = \chi_{\text{rough}}^2/v$ , where  $v$  is the number of degrees of freedom.

An essential feature of our tomography is that we select the model that minimizes the original, non-reduced  $\chi_{\text{rough}}^2$  and number of fit parameters, according to the Akaike Information Criterion  $AIC = \chi_{\text{rough}}^2 + 2s$  ( $s$  is the number

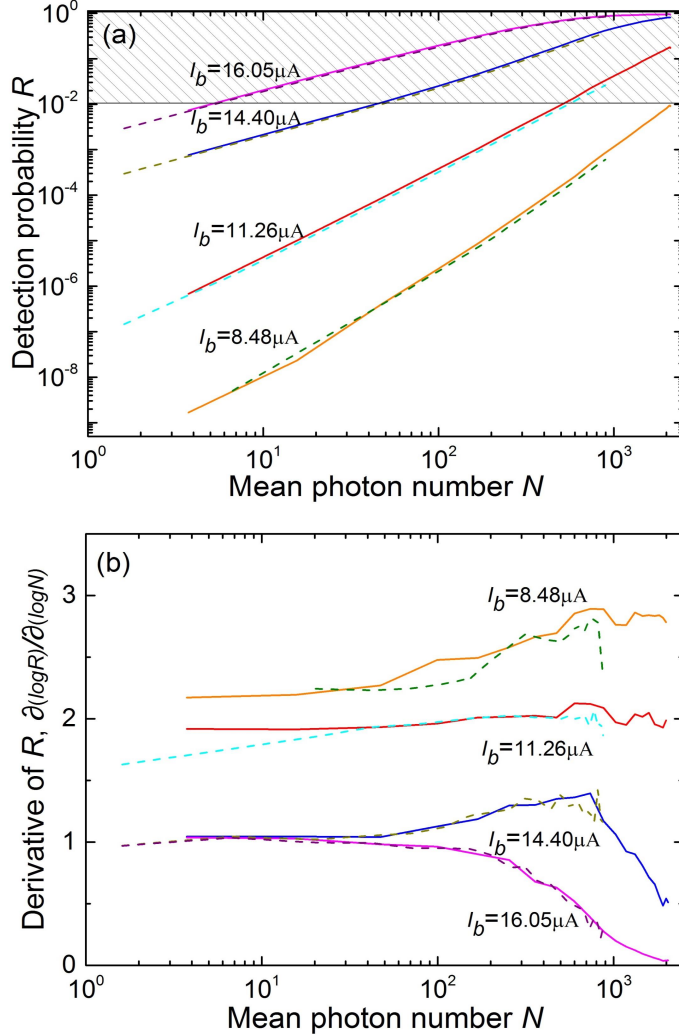


Figure 2.1: (a) Measured detection probability of the detector as a function of input photon number per pulse normalized to the laser repetition rate of 20 MHz. Data are shown for a high power setting (solid curves) and lower power (dashed curves) (b) Slope of the normalized count rate  $R$  on a log-log scale as a function of mean photon number  $N$  per pulse, giving a rough indication of the photon-number regime. At high bias currents ( $14.40 \mu\text{A}$  and  $16.05 \mu\text{A}$ ) the detector response is close to linear. For low bias currents ( $8.48 \mu\text{A}$  and  $11.26 \mu\text{A}$ ), the detector operates in a nonlinear regime.

of fitting parameters) [30,55]. This criterion minimizes the number of parameters needed to describe a detector and is particularly useful for detectors with low efficiency [29]. We find that for the SSPD studied here, the dark count rate associated with  $p_0(\sim 0)$  can be ignored and a description with only three parameters:  $\eta$ ,  $p_1$  and  $p_2$  suffices for all the bias currents.

It is important to stress again that the tomography put forward through Eq. (2.3) is completely general as it defines an (over)complete set of functions to describe the response of the detector. Alternative, more complex models can be defined that contain more detailed assumptions about the operation of the detectors. Such assumptions will alter the interpretation of the parameters in the model, but will not lead to a lower value of  $\chi^2$ . Therefore, we limit the discussion to the parameters that follow from the simplest possible complete model as defined through Eq. (2.3).

## 2.4 Overall noise and tomography results

In this section we analyze the noise in the measured data before starting a discussion on the influence of noise on the results of QDT. A straightforward way to show the noise is to quantify the statistical fluctuations of the data. We calculate the standard error of the mean (*SEM*) of the measured detection probability  $R$  for different integration times as a function of  $R$ , and normalize the *SEM* to the expected shot noise limit of the experimental data with an integration of 0.5 second. We normalize the *SEM* to this value, because a 0.5 second integration time together with the repetition rate  $f = 2 \times 10^7/\text{s}$  of our laser is comparable to the setting used in other tomography experiments on SSPDs [30,37]. The shot noise limit is given by  $\sqrt{R(1-R)/tf}$ , with the integration time  $t$ , as predicted by the binomial distribution for a sequence of  $tf$  independent experiments.

We take the experimental data of high laser power setting as an example. Figure 2.2 shows the *SEM* of the data at all values of bias current for different integration times. The four drawn curves serve to guide the eye and are obtained by averaging every 100 points in each data set. As the integration time increases the overall *SEM* of the data decreases, as expected with a factor of  $1/\sqrt{n}$ , where  $n$  is the ratio of the integration time to the reference of 0.5 second.

For larger integration times, typically beyond  $\sim 1$  second per point, it becomes most clearly apparent that the total noise in the measurements exceeds the shot noise level (horizontal lines) by a factor 4–5 when the detection probability  $R$  is above  $10^{-2}$ . This means that at longer integration times the experimental tomography is limited by both shot noise and technical noise. At very high count rates, close to saturation, the detector response may be

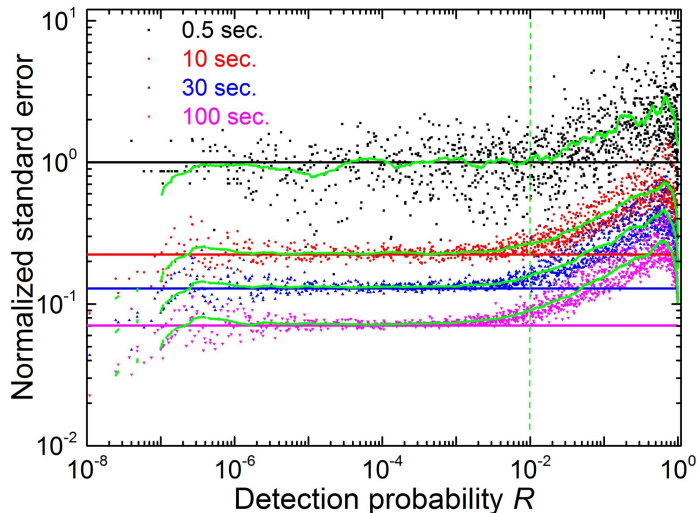


Figure 2.2: The ratio of the standard error of the mean of the data (high laser power setting) to the shot noise of the data with integration time of 0.5 second at all values of the bias current for different integration times.

influenced by heating effects [33, 56], which are not included in the detector response given by Eq. (2.3). Experimentally, we observe that the outcome of the tomography depends on the maximum photon count rate that is included in the fit procedure.

In order to exclude physical effects that go beyond the description from Eq. (2.3) we limit the data analysis to detection probabilities  $R$  below the value of  $10^{-2}$  (the left region of the vertical line in Fig. 2.2). This also excludes a large portion of the technical noise from the analysis. For practical tomography it is important to identify this threshold and find a tradeoff ( $10^{-2}$  in our case) between the error introduced by a too high threshold value and statistical errors introduced by a too low threshold value.

Figure 2.3 shows the quality of our fit  $\chi^2$  (based on the data of high laser power setting) on the left vertical axis as a function of the bias current for different maximum number of photons  $m$  in Eq. (2.3) up to 4. The figure indicates that a model with  $m = 2$  yields a good description of the data with a minimal set of fitting parameters ( $\eta$ ,  $p_1$  and  $p_2$ ), indicating that for  $i \geq 3$ , the internal efficiency  $p_i$  equals to 1, as desired.

In Fig. 2.3 the reduced  $\chi^2$  can be obtained only below the bias current of  $\sim 14 \mu\text{A}$ , this is due to the fact that the data of  $R$  above  $10^{-2}$ , corresponding to the shadowed data at bias currents  $> 14 \mu\text{A}$  in Fig. 2.1, are cut off and do not contribute to the QDT.

In the calculation of the reduced  $\chi^2$  we use the standard deviation  $\sigma_R$  of

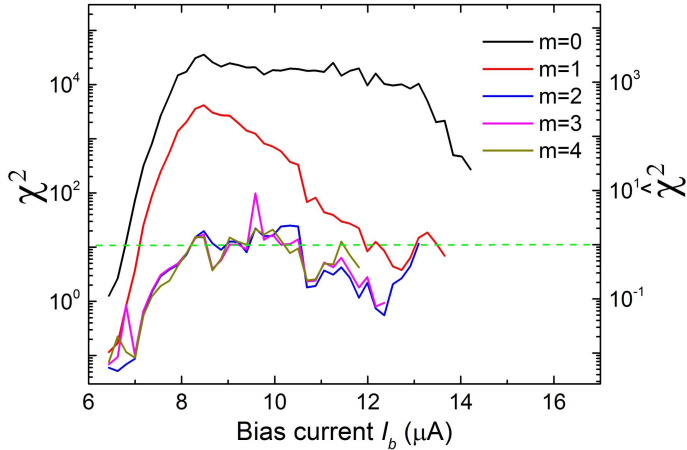


Figure 2.3: The reduced  $\chi^2$  and normalized  $\hat{\chi}^2$  from fitting the data to Eq. (2.3) at values of the detection probability  $R$  below  $10^{-2}$ . The reduced  $\chi^2$  is calculated based on the standard deviation of the raw data of  $R$ , while the normalized  $\hat{\chi}^2$  is based on the corrected standard deviation of  $R$  by including the long timescale fluctuations of the laser power.

the selected measured detection probability  $R$ . We find that the value of  $\chi^2$  is around  $\sim 10$  for currents from  $8 \mu\text{A}$  to  $11 \mu\text{A}$  while a good fit is supposed to have a  $\chi^2$  of 1.

The larger value of  $\chi^2$  can be interpreted as an underestimation of the standard deviation  $\sigma_R$  of the measured data. The standard deviation  $\sigma_R$  only shows the fluctuations in the data over a relatively short timescale of 100 seconds for each data point and ignores fluctuations or drifts in laser power on a longer timescale. In the next section we will show that a realistic estimate of this long term drift enlarges the  $\sigma_R$  by a factor of 3.3. Normalizing  $\chi^2$  by this value of  $\sigma_R$  leads to a  $\hat{\chi}^2 \sim 1$ , as shown in the right vertical axis in Fig. 2.3.

We emphasize that the QDT for both laser power settings was done using the reference power before the attenuator in order to verify that  $p_i$  and  $\eta$  can be determined as independent variables and that the value of  $\eta$  is lowered by the attenuation factor in the experiment. Figure 2.4(a) shows the internal detection efficiency  $p_1$  and  $p_2$  for a wavelength of 1200 nm as a function of bias current via tomography. We find that  $p_1$  and  $p_2$  for the two different powers are identical and are not influenced by the laser power setting, which confirms the separation between the internal detection process ( $p_i$ ) and the optical coupling process ( $\eta$ ). Meanwhile, the data of  $p_i$  shows the photon number regime that the detector operates in, e.g., below bias current of  $11 \mu\text{A}$  corresponding to 1-photon detection regime and above  $12 \mu\text{A}$  to 2-photon detection regime.

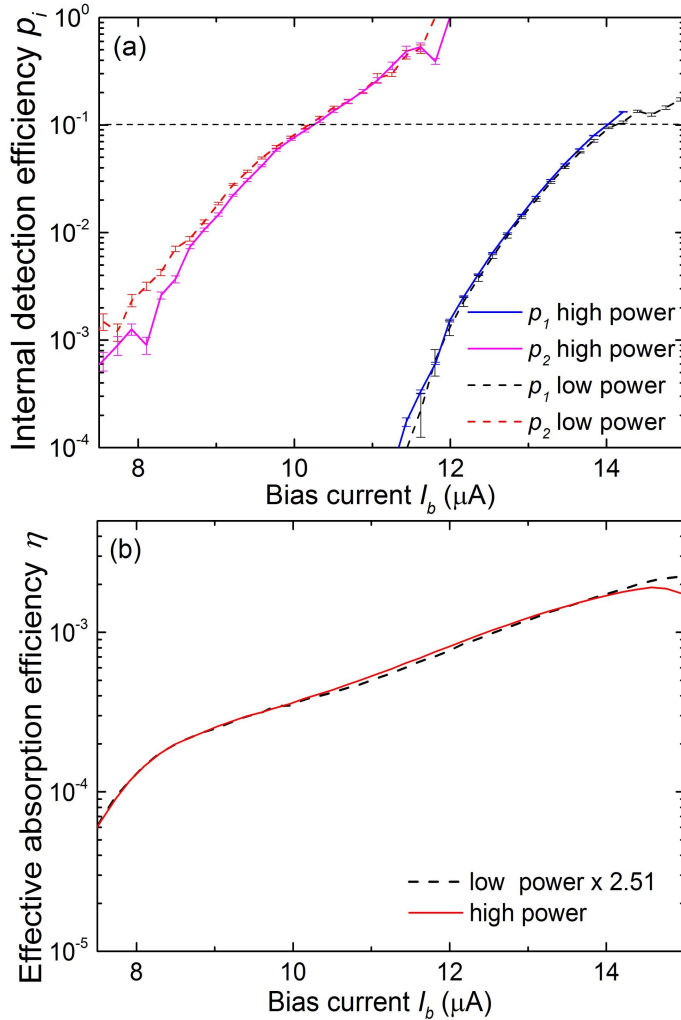


Figure 2.4: (a) Probabilities  $p_1$  and  $p_2$  of the NbN detector as a function of bias current determined by detector tomography. The horizontal line is used to calculate the relation between bias current and input photon energy in Section 2.5.6. (b) Effective absorption efficiency  $\eta$  for a photon participating in a detection event. Two sets of results are shown, corresponding to measurements at the two different input powers. The  $\eta$  for the low power is multiplied by 2.51, which is the attenuation factor in the beam path for the low power or the ratio of the high power to the low power input. The overlap between the curves ( $p_i$  and  $\eta$ ) demonstrates that the tomographic procedure retrieves the internal detection efficiencies that are intrinsic to the nature of the SSPD and separates them from the effective absorption efficiency.

The data in Fig. 2.4(b) shows the effective absorption efficiency  $\eta$  as a function of bias current, where the curve of  $\eta$  of the lower power setting is multiplied by the attenuation factor 2.51 for comparison. As we expected, linear loss or attenuation in the optical coupling is equivalent to rescaling the value of  $\eta$ , which confirms one of the main assumptions made in Ref. [29] to adapt detector tomography to detection systems with low efficiency.

In a straightforward interpretation of the detector tomography model a change in the value of  $\eta$  should not affect the retrieved values of  $p_1$  and  $p_2$ , because the values of  $p_i$  are interpreted as internal efficiencies that are related to the intrinsic detection mechanism of the NbN detector, while  $\eta$  is related to the coupling efficiency of a photon in the whole measurement system.

For an extended detector such as a meandering wire, the linear efficiency in the multiphoton regime is decreased because of the effect that two or more photons need to be absorbed close together to form a detection event [36, 57, 58]. Moreover  $\eta$  contains the optical absorption, inhomogeneities in the detector, the effect of bends and other factors that complicates further interpretation of this parameter. We restrict ourselves to the more straightforward interpretation to these intrinsic probabilities  $p_i$ .

## 2.5 Uncertainty budget and accuracy of tomography

### 2.5.1 Method of analyzing the uncertainty

Both shot noise and technical imperfections lead to fluctuations in the measured count rate that affect the value of  $p_i$  retrieved from tomography. We focus on the intrinsic detection probabilities  $p_i$ , quantify the fluctuations in the experiment, and discuss their origin and their consequences for the uncertainty of the  $p_i$  obtained from tomography. To simplify this task we will assume that all fluctuations are independent so that the uncertainty of  $p_i$  can be estimated by adding the uncertainty from each source.

We consider the effect of shot noise, fluctuations in laser power, nonlinearities in the optical power meter, instabilities of bias current and temperature. We use the tomography results at a bias current of 10.33  $\mu\text{A}$  and 14.00  $\mu\text{A}$  as an example, corresponding to a current setting where the detector operates in the two-photon regime and the one-photon regime, respectively.

We calculate the influence of the noise on the QDT results ( $p_i$ ) in two ways. For fluctuations of current and temperature we perform analytical error propagation based on the measured relation between  $p_i$  and  $I_b$ . For shot noise, laser power fluctuations and power meter instability, the relation between noise and  $p_i$  is more difficult to analyze due to the nonlinearity of Eq. (2.3). Therefore we

Table 2.1: The noise sources and the combined relative uncertainty.

Uncertainty source	Symbol	@ 10.33 $\mu\text{A}$ $p_1 = 0^*$ , $p_2 = 0.1$ ( $\eta = 4.09 \times 10^{-4}$ )	@ 14.00 $\mu\text{A}$ $p_1 = 0.1$ , $p_2 = 1^*$ ( $\eta = 1.71 \times 10^{-3}$ )
Shot noise ( $\propto 1/\sqrt{n}$ )	$u_S$	$3 \times 10^{-4}$	$0.4 \times 10^{-4}$
Laser power ( $\sigma_L = 2.8\%$ )	$u_L$	$9 \times 10^{-4}$	$16 \times 10^{-4}$
Power meter ( $\sigma_M = 0.9\%$ )	$u_M$	$0.5 \times 10^{-4}$	$0.3 \times 10^{-4}$
Bias current ( $\Delta I = 5.0 \text{ nA}$ )	$u_I$	$6 \times 10^{-4}$	$8 \times 10^{-4}$
Temperature ( $\Delta T = 4 \text{ mK}$ )	$u_T$	$6 \times 10^{-4}$	$9 \times 10^{-4}$
Combined uncertainty	$u = \sqrt{\sum_{k=1} u_k^2}$	$13 \times 10^{-4}$	$20 \times 10^{-4}$
Relative combined uncertainty	$U = u/p_i$	1.3%	2.0%

\*At current of 10.33  $\mu\text{A}$ , the detector is in 2-photon regime, where  $p_2 = 0.1$  and  $p_1$  is too low to be extracted from QDT; at current of 14.00  $\mu\text{A}$ , the detector is in 1-photon regime with  $p_1 = 0.1$ , and  $p_2$  fixed to 1.

perform numerical simulations<sup>2</sup>: we produce synthetic data of  $R_s$  with initial values of the tomography results (noted as  $\Pi_i$ ) at the two example currents. In this process we add noise to the synthetic data; then we perform tomography on these synthetic data and obtain the output (noted as  $P_i$ ); finally we obtain the uncertainty of the tomography results by calculating the difference between the initial ( $\Pi_i$ ) and the output values ( $P_i$ ). With these simulations we are able to evaluate how each of the noise sources (shot noise, laser power fluctuations and power meter instability) affects the tomography. The uncertainty of  $p_i$  caused by each noise source is summarized in Table 2.1. Details of the calculations are in section 2.5.2–2.5.7.

### 2.5.2 Shot noise

The fluctuations (or standard error of the mean) of a measured probability are fundamentally limited by statistical fluctuations of the discrete photon counting events. The standard error of the mean is predicted by binomial theory. To estimate how shot noise influences the final QDT results in our case, we perform tomography on synthetic data. As an example we use the experimental data at a bias current of 10.33  $\mu\text{A}$ , where  $p_1 = 0$ ,  $p_2 = 0.1$  and

<sup>2</sup>Matlab 2014b 64bits, The MathWorks, Inc.

$\eta = 4.09 \times 10^{-4}$ . In the simulation we take these initial values of  $p_i$  to be exact and denote these probabilities as  $\Pi_1$  and  $\Pi_2$ .

We first calculate the synthetic detection probability  $R_s$  as a function of the measured laser power by using Eq. (2.3), setting the  $\Pi_i$  and  $\eta$  values. We then add a noise term of  $r \times \sqrt{R_s(1-R_s)/tf}$  to  $R_s$  with  $tf = 2 \times 10^6$ ;  $r$  is a random number drawn from a Gaussian distribution with mean 0 and standard deviation 1. Then we repeat  $L = 1000$  times to produce  $L$  sets of detection probability.

On each set of synthetic data we perform tomography to retrieve values  $P_i$  for the internal detection efficiency  $p_i$ . We find that the value of  $P_1$  is indeed equal to 0, and we estimate the set of nonlinear parameters  $P_2$ , which may be different from the initial value  $\Pi_2$  that we set in the simulation. From these tomography simulations we extract the standard deviation  $\sigma_{pS}$  of the simulated  $P_2$ :

$$\sigma_{pS} = \sqrt{\frac{1}{L} \sum_{j=1}^L (P_{2,j} - \overline{P_2})^2}, \quad (2.4)$$

and we find that  $\sigma_{pS} = 7.9 \times 10^{-3}$ . The calculated mean value  $\overline{P_2}$  defined as  $\frac{1}{L} \sum_{j=1}^L P_{2,j}$ , is found to be equal to  $\Pi_2$ , indicating that the shot noise does not cause a bias, as expected. The shot noise affects the measurements in all  $L$  sets of measurements, and we need to consider the amount ( $L$  sets) of the synthetic data in uncertainty calculation: the uncertainty of  $P_2$  given by shot noise is calculated as  $u_S = \sigma_{pS} / \sqrt{L} = 3 \times 10^{-4}$ .

### 2.5.3 Laser power fluctuations

To estimate the magnitude and timescale of laser power fluctuations, we measure the laser power for 10 hours with a commercial Ge-based power meter (PH20-Ge, Gentec-EO).

Both short timescale fluctuations and long timescale drift in measured laser power are observed as shown in Fig. 2.5(a). The relative standard deviation of the measured laser power over the measurement of 10 hr is calculated to be  $\sigma_L = 2.8\%$  of the mean power. Figure 2.5(b) shows the autocorrelation function of the measured laser power of Fig. 2.5(a), and it demonstrates a long-timescale (of hours) fluctuation or drift of the laser power.

In the experiment of QDT, we vary laser power input using two polarizers, and fix a certain power (i.e., a fixed angle between two polarizers) into the cryostat and measure count rates as a function of detector bias current. We then repeat the measurement as a function of current for all input powers and convert the measured data to count rates as a function of input power at a fixed current. This data is then fed to the tomography algorithm. A consequence of

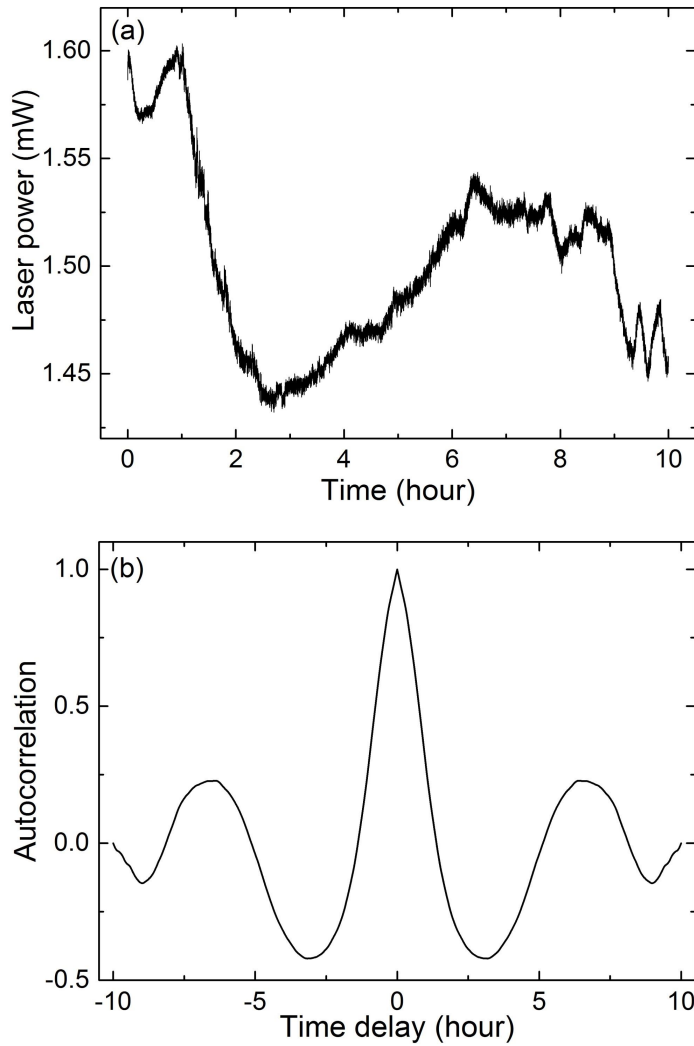


Figure 2.5: (a) Fluctuations in laser power output at 1200 nm wavelength as a function of time showing both fast fluctuations and long term drift with an amplitude of  $\sim 0.2$  mW over the whole timescale of 10 hours. (b) Corresponding autocorrelation function of laser power fluctuations.

this approach is that two adjacent points in the dataset are recorded approximately 1.6 hr after each other. At this timescale the autocorrelation function of the laser power fluctuations is close to zero, which means that laser power values are uncorrelated, and their fluctuations can be approximated as random. Each measured curve of count rate as a function of input power at constant current contains 25 points. During the measurement of each data point (100 seconds), the laser power is relatively constant because of the small standard deviation of 0.15% over this short time interval. Between the adjacent points with time interval of 1.6 hr, the long-timescale fluctuations of laser power are important (2.8%).

We assume that the power fluctuations are uncorrelated because the time interval between measurements is comparable to the timescale of the slow variations in laser power. To investigate to what extent the random laser fluctuations influence the tomography, we perform numerical simulations to take into account the nonlinear dependence of detection probability as a function of laser power as expressed by Eq. (2.3).

We use the data at the bias current of 10.33  $\mu\text{A}$  as an example. We first simplify the calculation by assuming that the fluctuations in the 25 laser power values are random. We add the random fluctuations to the calculation by multiplying each value with a factor of  $(1 + \sigma_L \times r)$ .

We then calculate one set of synthetic detection probability  $R_s$  by using Eq. (2.3), which involves the fluctuated laser power and the  $\Pi_i$  and  $\eta$  value. Finally, we do tomography to get the estimated  $\Pi_i$ . After repeating the procedure  $L$  times we have a set of simulated  $P_2$  with the mean value  $\bar{P}_2$  ( $P_1$  is equal to 0), and we calculate the bias of  $P_2$  as  $\Delta P_{2L} = \bar{P}_2 - \Pi_2 = 9 \times 10^{-4}$ , so we get the uncertainty of  $P_2$  given by laser power fluctuations  $u_L = \Delta P_{2L} = 9.4 \times 10^{-4}$ .

The long-timescale fluctuations ( $\sigma_L = 2.8\%$ ) of laser power are not included in the standard deviation  $\sigma_R$  of the measured data, so it leads to an underestimation of the noise of the data and increases the reduced  $\chi^2$ . We calculate the change in the measured detection probability  $R$  caused by fluctuations of the laser power (the mean photon number  $N$ ) as  $\Delta R = \frac{\partial R}{\partial N} \Delta N = \frac{\partial R}{\partial N} N \frac{\Delta N}{N}$  via Eq. (2.3), where we use the values of  $p_i$  and  $\eta$  at 10.33  $\mu\text{A}$ , and  $\frac{\Delta N}{N}$  is 2.8%. The results show that  $\Delta R$  is  $R$  dependent and is in a range of  $1 \times 10^{-4} - 4 \times 10^{-4}$ . We estimate the new overall fluctuations of the data in a simple way as  $\sigma'_R = \sqrt{\sigma_R^2 + \Delta R^2} = 3.3\sigma_R$  by using the averaged value  $\overline{\Delta R} = 2.5 \times 10^{-4}$ . With this correction for the overall fluctuations the QDT gives a lower  $\hat{\chi}^2$  of  $\sim 3$  at 10.33  $\mu\text{A}$ , which is suppressed from the value ( $\sim 40$ ) in the original QDT (see  $\chi^2$  in Fig. 2.3). We conclude that the long-timescale drift (e.g., in laser power) causes the larger values of  $\chi^2$ .

### 2.5.4 Accuracy of the power meter

The function of the power meter is to provide reference values of laser power that are inserted in the tomography. The power meter has an absolute accuracy that shifts all points equally and leads to a systematic error, which can be simply attributed to a change of  $\eta$ . In addition, the relative uncertainty of the power meter is limited by noise (e.g., dark count) of the power meter itself.

We record the laser power with a commercial Ge-based power meter (PH20-Ge, Gentec-EO) that has a specified relative uncertainty of  $\pm 0.3\%$  to  $\pm 0.9\%$  given by NIST [59]. In our simulation we take the upper limit (0.9%) as a conservative estimate of fluctuations in the readout of the power meter. To study the fast-fluctuation influence on the final  $p_i$ , we generate one set of detection probabilities with the original measured laser power values as the true values. Then in the fitting part we use a different calibration curve that contains the fluctuations in power measurement by multiplying each point of the original laser power with a factor of  $(1 + \sigma_M \times r)$ , where the  $\sigma_M$  equals 0.9%. We repeat this procedure  $L$  times and get a set of  $P_2$ . The difference of  $\Pi_2$  and  $\bar{P}_2$  is  $\Delta P_{2M} = 0.5 \times 10^{-4}$ , and the uncertainty of  $P_2$  given by power meter is  $u_M = \Delta P_{2M} = 0.5 \times 10^{-4}$ .

### 2.5.5 Current fluctuations

As can be seen in Fig. 2.4(a) the detection probabilities are strongly dependent on bias current. Based on the outcome of the tomography we find an empirical relation to describe the relevant part of the  $p_i$  curve. This empirical relation allows standard error propagation by calculating the sensitivity of the  $p_i$  to bias current fluctuations as the local derivative of the empirical curve. As an example we take  $p_2$  at a bias current of  $10.33 \mu\text{A}$  and fit the current dependence to the function:

$$p_2(I_b) = p_2(10.33\mu\text{A})e^{\alpha(I_b - 10.33\mu\text{A})}. \quad (2.5)$$

We obtain a value of  $p_2(10.33 \mu\text{A}) = 0.10$ , and the slope  $\alpha = 1.121 \pm 0.004 \mu\text{A}^{-1}$ . The influence of current fluctuations on the accuracy of  $p_2$  can be estimated from a Taylor expansion of Eq. (2.5) and yields

$$\Delta p_{2I} = \frac{\partial p_2(I_b)}{\partial I_b} \Delta I_b = \alpha p_2(10.33\mu\text{A}) \Delta I_b. \quad (2.6)$$

The uncertainty of  $p_2$  given by bias current fluctuations  $\Delta I_b = 5.0 \text{ nA}$  is  $u_I = \Delta p_{2I} = 6 \times 10^{-4}$ . The value of  $\Delta I_b$  is the average of the standard deviations of all the measured bias currents in the experiment.

### 2.5.6 Temperature fluctuations

The detection probabilities in our experiment are a function of temperature because the working principle of SSPDs is based on a superconducting material whose properties (e.g., critical current  $I_c$  and coherence length  $\xi$ ) are functions of temperature. We use a PID feedback control loop (Lake Shore model 350) to actively stabilize the temperature to  $T_o = 3.2$  K. The measured fluctuations of the temperature in the cryostat are in the range of  $\pm 4$  mK, which we take as the standard deviation of the temperature.

To calculate the influence of the temperature on  $p_2$  at  $10.33 \mu\text{A}$ , we link  $T$  and  $p_2$  via the bias current  $I_b$ . To estimate the fluctuations we use

$$\Delta p_{2T}(T) = \frac{\partial p_2(I_b)}{\partial I_b} \frac{\partial I_b}{\partial T} \Delta T, \quad (2.7)$$

in which the term  $\frac{\partial p_2(I_b)}{\partial I_b}$  has been given by Eq. (2.5), and  $\frac{\partial I_b}{\partial T}$  can be obtained from the observation that the detector is an energy detector [30]. Following Ref. [30], for a certain observed  $p_2$ , the bias current  $I_b$  of the SSPD has a linear relation with the total excitation photon energy  $E$ :

$$I_b(T) = I_o(T) - \gamma E. \quad (2.8)$$

The slope  $\gamma$  is found to be temperature independent and is determined by the properties and geometry of the NbN film [30]. By putting a horizontal line  $p_i = 0.10$  onto Fig. 2.4(a) we get two crossover points:  $I_{b1} = 14.00 \mu\text{A}$  for one 1200 nm photon with  $E_1 = 1.033$  eV, and  $I_{b2} = 10.33 \mu\text{A}$  for two photons with  $E_2 = 2.066$  eV. Using these two points  $(E_1, I_{b1})$  and  $(E_2, I_{b2})$  we estimate  $\gamma = 3.58 \mu\text{A}/\text{eV}$  and  $I_o = 17.72 \mu\text{A}$  at 3.2 K. The temperature-dependent current  $I_o(T)$  has an expression based on Ref. [30, 60]:

$$I_o(T) = I_o(T_o) \frac{\sqrt{1 - T/T_c}}{\sqrt{1 - T_o/T_c}}, \quad (2.9)$$

where  $T_o = 3.2$  K and  $T_c = 9.42$  K. Using above, we calculate the bias of  $p_i$  due to temperature fluctuations around  $T_o = 3.2$  K and  $10.33 \mu\text{A}$ :

$$\Delta p_{2T} = -\frac{1}{2} p_2(10.33 \mu\text{A}) * I_o(3.2\text{K}) \alpha \frac{1}{T_c - T_o} \Delta T. \quad (2.10)$$

The uncertainty of  $p_2$  given by temperature is  $u_T = |\Delta p_{2T}| = 6 \times 10^{-4}$ .

### 2.5.7 Combined standard uncertainty

We have calculated the influence of all uncertainty sources on  $p_2$  for bias current  $10.33 \mu\text{A}$ , and we can compare these calculations to the observed fluctuations in the raw data. We use Eq. (2.3) to create synthetic data that includes all the technical fluctuations, and the contribution due to shot noise.

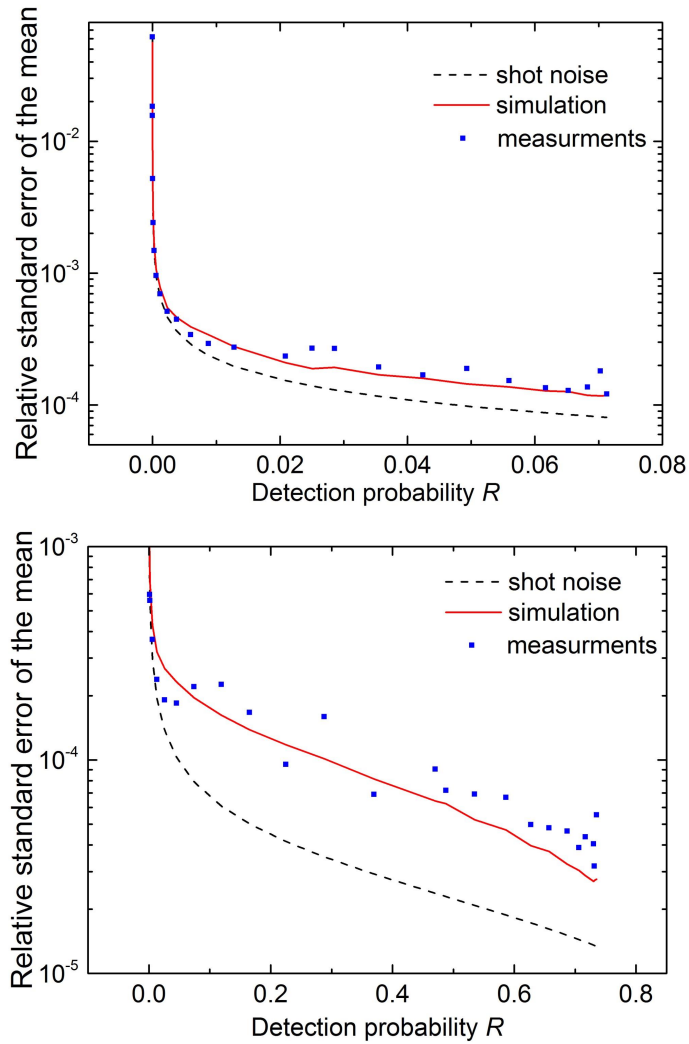


Figure 2.6: The relative standard error of the mean of detection probability ( $SEM/R$ ) at the bias current  $10.33 \mu\text{A}$  (a) and  $14.00 \mu\text{A}$  (b). The symbols represent experimental values. The black dashed curve is the predicted shot noise limit. The red curve takes into account additional fluctuations (laser power, current and temperature fluctuations) present in the experiment.

To incorporate fluctuations in laser power, we multiply the mean photon  $N$  by a factor of  $(1 + \sigma_L \times r)$ . Both temperature and bias current fluctuations affect the probabilities  $\Pi_2$ . To simulate these effects, we add  $r \times \sqrt{\Delta p_{2I}^2 + \Delta p_{2T}^2}$  to  $\Pi_2$ , in which  $p_{2I}$  and  $p_{2T}$  quantify the change in  $\Pi_2$ . The value of  $\Pi_1=0$  remains constant in this example.

Next, we (we already used Eq. (2.3) to create the synthetic data  $R_s$ ) add shot noise given by the binomial distribution as  $r \times \sqrt{R_s(1 - R_s)/tf}$  to  $R_s$ , with  $tf = 2 \times 10^6$ . We repeat the process 1000 times to obtain a set of synthetic data  $R_s$ , from which we calculate the averaged estimated  $\overline{R_s}$  ( $\overline{R_s} = \frac{1}{L} \sum_{j=1}^L R_{s,j}$ ) and the standard error of the mean  $SEM$ .

For bias current  $14.00 \mu\text{A}$  we repeat the same procedure. Figure 2.6 compares the normalized values of  $SEM/R$  for the measured data (blue points) to the simulation (red line) at the two typical currents of  $10.33 \mu\text{A}$  (a) and  $14.00 \mu\text{A}$  (b). The black dashed curve corresponds to the shot noise level. At each of the two currents, for low detection probabilities ( $R < 10^{-2}$ ) the shot noise dominates the measurement, while for larger detection probabilities ( $R > 10^{-2}$ ) the fluctuations due to technical noise sources (i.e., laser power, bias current and temperature) exceed the shot noise. The agreement of the measurement and simulations show that shot noise becomes more important at lower bias current since the overall count rate is lower, and that our experimental tomography operates in the nontrivial regime where technical noise becomes comparable to shot noise.

Table 1 shows all the noise sources and their influences on the internal detection efficiencies. The relative combined uncertainty of  $p_2$  at  $10.33 \mu\text{A}$  and  $p_1$  at  $14.00 \mu\text{A}$  are 1.3% and 2.0%, respectively, which reflects an high accuracy of the QDT procedure in our work. In our experiment laser power fluctuations contribute the most to the total uncertainty for both currents (or one-photon and two-photon regimes). An improvement of the accuracy of the QDT would result from using a more stable laser. However, if we eliminate laser power fluctuations from the error budget, the final relative combined uncertainty is only decreased to 0.9% ( $10.33 \mu\text{A}$ ) and 1.1% ( $14.00 \mu\text{A}$ ), because the other noise sources have a comparable effect on the outcome of QDT. The accuracy can only be significantly improved by minimizing the influences of all other technical noise, e.g., by also optimizing the design of electronic circuit and temperature feedback controlling of cryostat.

## 2.6 Conclusions

We have performed tomography at 1200 nm wavelength on an SSPD using quantum detector tomography and obtained the internal detection efficiency in different photon number regimes. We deliberately added optical loss to the

setup to rigorously demonstrate the separation of overall macroscopic absorption efficiency from the intrinsic, microscopic detection probabilities  $p_i$ .

We find that additional technical noise exists in the measurement, which makes the fluctuations of the noise level higher than shot noise level at detection probabilities  $R > 10^{-2}$ . By limiting the data to this threshold of  $10^{-2}$ , we improve the fit in tomography leading to a decreased value of  $\chi^2$ . The accuracy of the tomography is limited by long time drift in laser power, while short time fluctuations in bias current and temperature have a comparable effect.

We measured fluctuations including laser power, power meter accuracy, bias current, and temperature. The sensitivity of tomography to each of these factors is evaluated either via numerical simulation or via error propagation to quantify the total uncertainty of the  $p_i$ . We find that both  $p_1$  and  $p_2$  can be determined with a small relative uncertainty of 1.3% and 2.0%.



## Chapter 3

# Position-Dependent Detection Efficiency of a Single NbN Nanowire SSPD

We probe the local detection efficiency in a nanowire superconducting single-photon detector along the cross section of the wire with a spatial resolution of 10 nm. We find a strong variation in the local detection efficiency of the device. Our experimental results agree with theoretical calculations based on a photon-assisted vortex entry model<sup>1</sup>.

### 3.1 Introduction

Nanowire superconducting single-photon detectors (SSPDs) consist of a superconducting wire of nanoscale cross section [14], typically 5 nm by 100 nm. Photon detection occurs when a single quantum of light is absorbed and triggers a transition from the superconducting to the normal state. SSPDs have high efficiency, low jitter, low dark count rate and fast reset time [61], and are therefore a key technology for, among others, quantum key distribution [50], interplanetary communication [62] and cancer research [63].

Although considerable progress has been made recently, the underlying physical mechanism responsible for photon detection on the nanoscale is still under active investigation. A combination of theory [23, 60], experiments [30,

---

<sup>1</sup>This chapter is based on J. J. Renema, Q. Wang, R. Gaudio, I. Komen, K. op't Hoog, D. Sahin, A. Schilling, M. P. van Exter, A. Fiore, A. Engel, and M. J. A. de Dood, *Nano Lett.* **15**, 4541, (2015).

38,40], and simulations [24,25] on NbN SSPDs indicates that the absorption of a photon destroys Cooper pairs in the superconductor and creates a localized cloud of quasiparticles that modifies the current distribution in the wire. This, in turn, can make the wire susceptible to the entry of a magnetic vortex from the edge of the wire by lowering the energy barrier for vortex entry; this barrier depends on the superconducting electron density near the edge of the wire. A photon being absorbed near the edge generates a substantial decrease in this density near that edge and thus a quite large decrease in the energy barrier for vortex entry. Contrarily, when a photon is absorbed in the middle of the wire, the superconducting electron density decrease near the edge is small and the energy barrier for vortex entry is only little affected by the absorption of the photon. Energy dissipation by the vortex moving across the wire drives the system to the normal state and causes the detector to “click”. The “click” probability thus depends on the location of the photon-absorption within the wire (edge or center). An important implication of this detection model is that such a detector has non-uniform detection probability with photons absorbed close to the edge having a higher local detection efficiency compared to photons absorbed in the center of the wire [25].

This effect has practical implications for the operation of SSPDs, since it represents a potential limitation on the detection efficiency [42]. In addition, SSPDs have been proposed for nanoscale sensing, either in a near-field optical microscope configuration [32] or as a subwavelength multiphoton probe [64], where this effect would be of major importance for the properties of such a microscope. While this effect has been predicted theoretically, clear experimental evidence is missing.

In this chapter, we experimentally explore the nanoscale variations in the intrinsic response of the detector. We explore the spatial variations in the detection efficiency with a resolution of approximately 10 nm, i.e., better than  $\lambda/50$ , using far-field illumination only. We find that our results are qualitatively consistent with numerical simulations [24,25].

The key technique used in this work is a differential polarization measurement that probes the internal detection efficiency of the detector. The technique is based on the fact that polarized light is preferentially absorbed at different positions for the two orthogonal polarizations, due to differences in boundary conditions. Using this technique, we achieve selective illumination of either the edges or the middle of the wire. By doing so at different wavelengths, we are able to probe the intrinsic photodetection properties of our device on the nanoscale.

### 3.2 Separation of optical absorption and internal detection efficiency

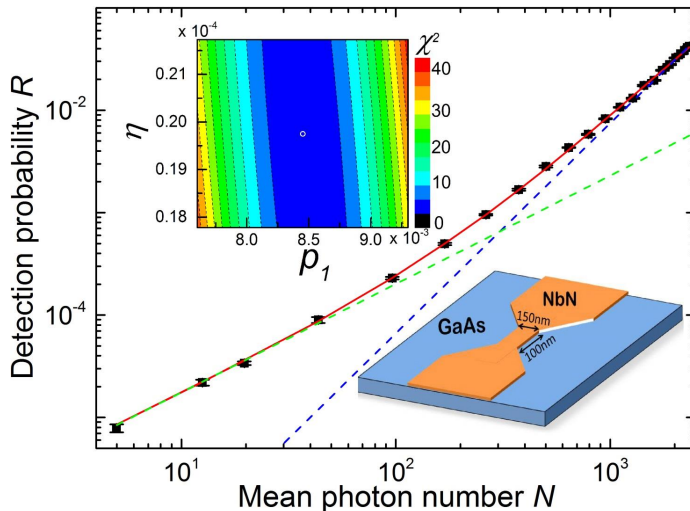


Figure 3.1: Detection probability as a function of input photon number at a wavelength of 1500 nm. The points represent experimental data with error bar. The red curve represents the fit by quantum detector tomography. The data are shown for a bias current equal to  $I_b = 22.7 \mu\text{A}$ ; we find that  $\eta = 1.98 \times 10^{-4}$  and  $p_1 = 8.46 \times 10^{-3}$ . The top inset provides a landscape picture of how the reduced  $\chi^2$  varies with  $\eta$  and  $p_1$ , and the white circle indicates the minimum of  $\chi^2$ . The bottom inset shows the structure of the SSPD, in which a single NbN nanowire is patterned in between two broader parts on a GaAs substrate, and an 80 nm thick HSQ layer (not shown) is covered on the NbN nanowire.

It is well known that changing the polarization of the incident light results in a change in overall optical absorption in an anisotropic structure such as a wire or a meander [42, 47, 65–67]. Therefore, our first task is to separate the probability that a photon is absorbed from the internal detection efficiency, where the latter is defined as the conditional probability that an absorbed photon causes a detection event. To make this separation, we use quantum detector tomography (QDT) [28–30, 34, 36–38, 53, 68–70].

QDT records the detector response to a set of known quantum states of light and distills from these measurements the detection probability for different photon numbers for the detector as a whole. As shown in Chapter 2 and Ref. [29], this procedure allows us to unambiguously separate the single-photon detection probability  $p_1$  from the probability  $\eta$  that a photon is absorbed. We find that  $\eta$  is almost independent of detector bias current for a nano SSPD and that its value is consistent with the geometric area of the detector [29]. Hence,

we identify  $p_1$  with the internal detection efficiency conditional on photon absorption, which we henceforth refer to as the internal detection efficiency or *IDE*.

Figure 3.1 shows, on a log-log scale, the measured detection probability  $R$  (points) as a function of mean photon number  $N$  for an illumination wavelength of 1500 nm. The data have been taken at a detector bias current of  $I_b = 22.7 \mu\text{A}$  ( $I_b/I_c = 0.81$ , where  $I_c$  is the device critical current). The bottom right inset shows the schematic structure of the SSPD in the experiment. A 150 nm wide, 100 nm long and 5 nm thick nanowire in between two tapered parts is fabricated on a semi-infinite GaAs substrate. The NbN is deposited on the GaAs substrate which is subsequently patterned by e-beam lithography and reactive ion etching [27], leaving an 80 nm thick HSQ (Hydrogen silsesquioxane) layer on top of the NbN nanowire for protection. The line through the data corresponds to the result of our QDT analysis. From the fit we find an internal detection efficiency  $p_1 = 8.46 \pm 0.17 \times 10^{-3}$ ,  $p_2 = 4.02 \pm 0.08 \times 10^{-1}$ , and an absorption efficiency  $\eta = 1.98 \pm 0.04 \times 10^{-4}$ . We note that the small value of  $\eta$  is related to the ratio between the active area of the nanodetector and the area of the optical beam. This ratio is small because the beam size was kept large to become insensitive to small variations in optical alignment. The two dashed lines in Fig. 3.1 indicate detection in the one-photon regime (green) and in the two-photon regime (blue), displaying a clear distinction between the two regimes.

Linear independence of fit parameters is illustrated in the top left inset, which shows a false color plot of the reduced goodness-of-fit  $\chi^2$  as a function of  $\eta$  and  $p_1$ . The white circle shows the minimum value of the reduced  $\chi^2$ , which represents the best fit. As can be seen in the inset,  $p_1$  and  $\eta$  can be determined with high accuracy (more details in Chapter 2).

### 3.3 Polarization-dependent internal detection efficiency

We have repeated the QDT procedure for different input polarizations and wavelengths of the incident light. Figure 3.2(a) shows the *IDE* and effective absorption efficiency  $\eta$  as a function of polarization at a wavelength of 1500 nm. The error bars in the figures are calculated from the standard deviation of a series of independent experiments. Note that the parameters obtained from this QDT analysis are quantities that represent the detector as a whole. A simple model of the detector would assume that only the effective absorption efficiency  $\eta$  depends on the polarization of the incident light.

So, it comes as a surprise that Fig. 3.2(a) shows that not only  $\eta$  but also the *IDE* is polarization dependent; actually they oscillate in phase as a function

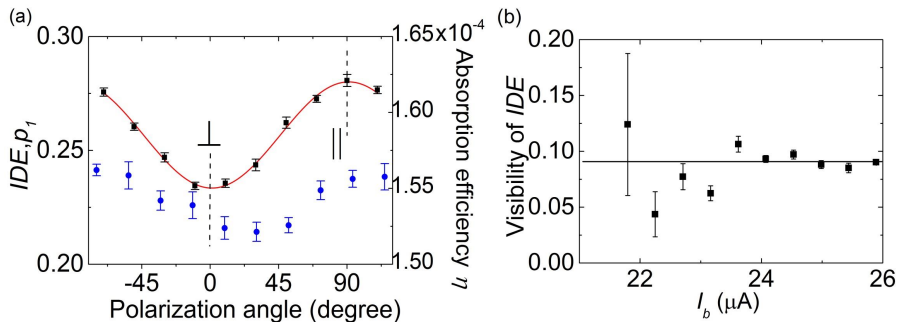


Figure 3.2: Polarization dependence of the internal detection efficiency at a wavelength of 1500 nm. (a) shows the internal detection efficiency  $IDE$  or  $p_1$  (black squares) and the effective absorption efficiency  $\eta$  (blue dots) as a function of the polarization of the incident light. The internal detection efficiency points are fitted by a sine function (red curve). The minimum and maximum of the fit are noted as perpendicular  $\perp$  and parallel  $\parallel$ . (b) shows polarization visibility of the  $IDE$  as a function of bias current. The horizontal curve represents the current averaged visibility.

of the polarization direction relative to the nanowire. We therefore introduce the visibility of the  $IDE$  as

$$V_{IDE} = (p_{1,max} - p_{1,min}) / (p_{1,max} + p_{1,min}). \quad (3.1)$$

To verify that our observation of a polarization-dependent  $IDE$  is robust we repeated the experiment for different bias currents. We find that the values of  $p_i$  depend strongly on bias current, as expected [38]. The visibility  $V_{IDE}$ , however, is independent of bias current and has an average value of 0.09 for the wavelength of 1500 nm, which is represented by the horizontal line in Fig. 3.2(b). Furthermore, we observe that the maximal and minimal  $IDE$  ( $p_{1,max}$  and  $p_{1,min}$ ) occur when the polarization is parallel and perpendicular to the nanowire, respectively. This indicates that under perpendicular illumination the absorbed photon is less likely to cause a detection event.

To find a physical explanation of the observed polarization dependence the simple model that we have used so far needs to be extended. While the QDT analysis yields an effective absorption efficiency  $\eta$ , it is well known that the optical absorption is position dependent, because of different boundary conditions for electric fields parallel and perpendicular to the nanowire. A possible interpretation of the polarization-dependent  $IDE$  is thus to assume that the observed internal detection efficiency itself depends on position. Therefore, we introduce a new quantity, namely the local detection efficiency  $LDE(x)$  to take these spatial variations into account. The observed polarization dependence is a combination of the position-dependent absorption distribution  $A(x)$  and a position-dependent local detection efficiency  $LDE(x)$ , where the latter can

be interpreted as the conditional probability that the detector produces a click given that a photon is absorbed at position  $x$ .

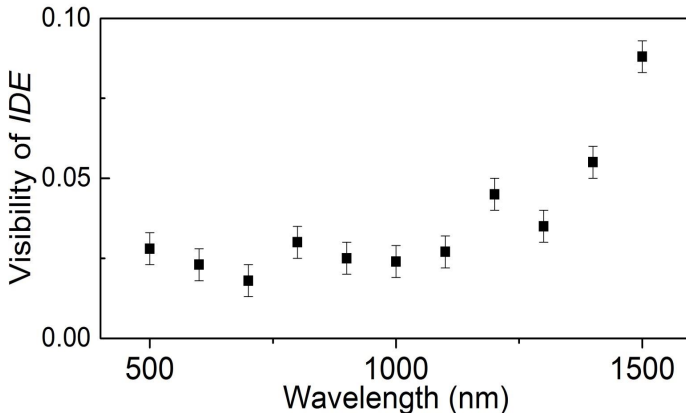


Figure 3.3: Plot of the visibility of the internal detection efficiency. For each wavelength the current-averaged value of the visibility is displayed.

Both the absorption efficiency and the local detection efficiency depend on wavelength. A description of the polarization and wavelength dependent  $IDE$  as measured by QDT is then given by:

$$IDE_k(\lambda) = \frac{\int A_k(\lambda, x)LDE(\lambda, x)dx}{\int A_k(\lambda, x)dx}, \quad (3.2)$$

where  $\lambda$  is the wavelength of illumination, and the subscript  $k = \{||, \perp\}$  refers to the polarization. The optical absorption distribution  $A_k(\lambda, x)$  can be obtained by numerically solving Maxwell's equations (see Section 3.4), and the  $LDE(\lambda, x)$  can be considered as fitting parameters, in which  $x$  is the variable and  $\lambda$  is a well described constraint (see Section 3.5).

We have measured the visibility  $V_{IDE}$  of the internal detection efficiency at a large wavelength range from 400 nm to 1500 nm. Figure 3.3 shows the measured visibility  $V_{IDE}$  as a function of wavelength. As a result,  $LDE(\lambda, x)$  at a particular wavelength can be determined by the fit. The results of  $LDE(x)$  and details of the fit are introduced in the following sections.

### 3.4 Optical absorption

Before discussing the local detection efficiency  $LDE(\lambda, x)$  we report on the calculated absorption distribution  $A(\lambda, x)$ . The aim of this section is to reduce the complexity of the problem by replacing the 3D absorption with an approximate 2D calculation of  $A(\lambda, x)$  that only depends on the transverse coordinate  $x$ .

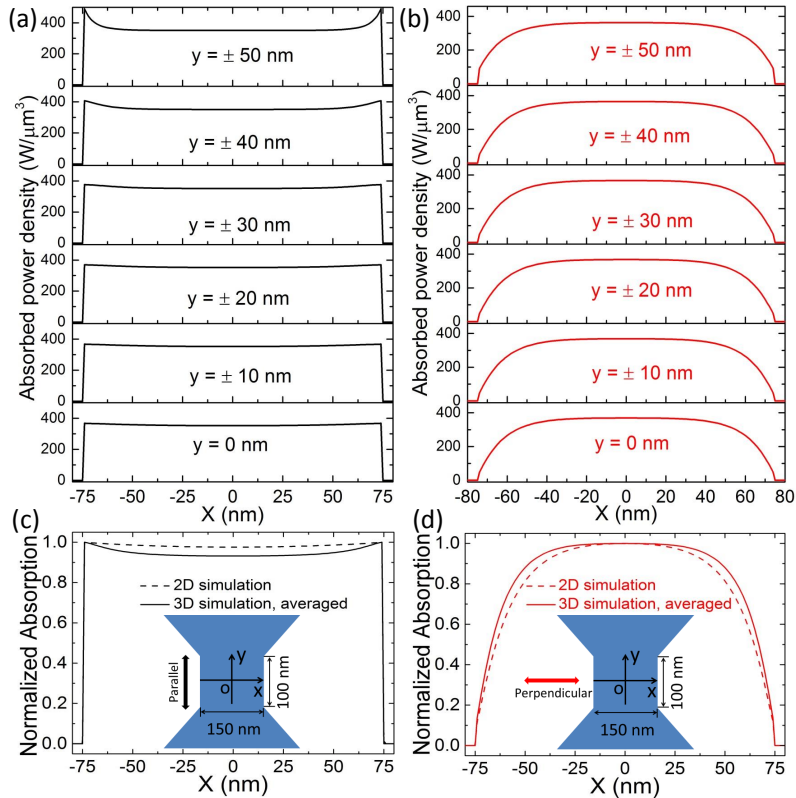


Figure 3.4: Absorption distribution by FDTD simulation at the wavelength of 1500 nm for parallel (left) and perpendicular (right) polarization. For each polarization, (a) and (b) obtained from 3D simulation show the absorption density across the wire ( $x$ -direction) at different  $y$  positions from the center ( $y = 0$  nm) to the ends ( $y = \pm 50$  nm) of the nanowire. (c) and (d) compare the 3D absorption density averaged on  $y$  position (solid line) and 2D absorption density (dashed line).

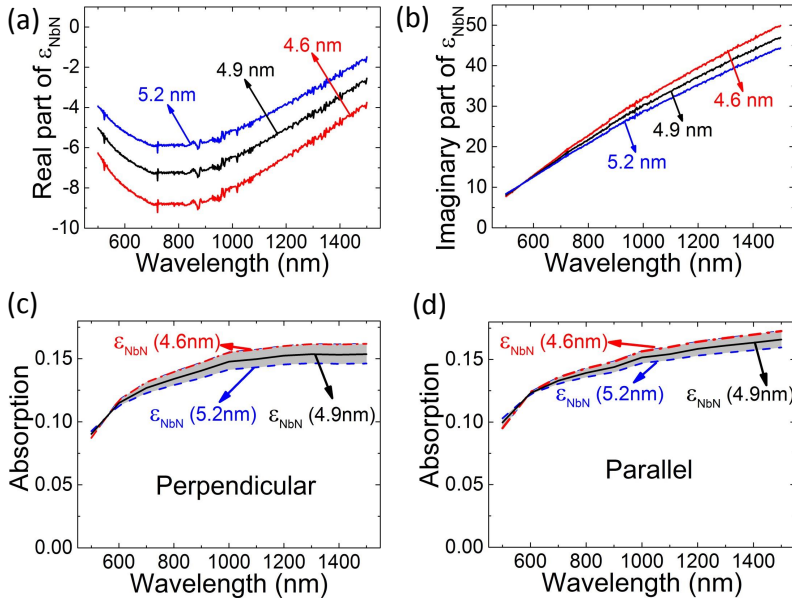


Figure 3.5: Dielectric constant of our NbN film as obtained by ellipsometry by assuming different values for the film thickness. (a) and (b) show the real and imaginary part of the dielectric constant. (c) and (d) show calculated absorption spectra for parallel and perpendicular polarization using the value of the dielectric constant shown in (a) and (b).

The absorption in the NbN nanowire is calculated using a commercial finite-difference-time-domain method (FDTD, FullWave package, RSoft [71]). We take a 3D simulation at a wavelength of 1500 nm for example. In the simulation, we describe the materials as shown in Fig. 3.1 (with an 80 nm layer of HSQ on top of NbN nanowire). Figures 3.4(a) and 3.4(b) show the 1D absorption distribution across the nanowire from center ( $y = 0$  nm) to the boundaries between the nanowire and the tapered parts ( $y = \pm 50$  nm) obtained from the 3D simulations. For both parallel and perpendicular illumination, the absorption profiles do not depend much on the coordinate  $y$ , which demonstrates that the tapered parts have minimal influence on the absorption of the nanowire. This allows us to perform a simpler and more efficient 2D simulation of the cross section of the nanowire to describe the absorption distribution in the nanowire.

Figures 3.4(c) and 3.4(d) show the comparison of simulations for a 2D infinite wire (dashed) and the 3D geometry (solid). The 3D absorption curve is obtained by averaging the absorption curves at different  $y$  positions in Figs. 3.4(a) and 3.4(b). The absorption curves from 2D and 3D simulations are normalized to their maximum because we are interested in the relative difference between the curves. We find that in case of perpendicular illumination the absorption mainly occurs in the middle of the nanowire while for the parallel case the absorption is roughly uniform over the entire nanowire. There is very little difference between 2D and 3D simulations for both parallel and perpendicular illumination in our geometry, justifying the use of much more efficient 2D simulations for other wavelengths.

The optical absorption is determined by the dielectric constant of NbN, which is obtained via ellipsometry [72]. In Ref. [72] a thickness of 4.9 nm was estimated. We assume a conservative error bar of 0.3 nm on the thickness, and recalculate epsilon via numerical inversion of the ellipsometry data for three different thicknesses resulting in the curves shown in Figs. 3.5(a) and 3.5(b).

Based on the three sets of the dielectric constant we calculate the absorption for perpendicular and parallel illumination, which are shown in Figs. 3.5(c) and 3.5(d). For most wavelengths (600 nm – 1500 nm), the film absorbs most if we assume the film to be thinnest (4.6 nm), which is due to the larger imaginary part of the dielectric constant. The variations in the dielectric constant are treated as systematic error in the following sections.

### 3.5 Position-dependent local detection efficiency

In order to distill from Eq. (3.2) the local detection efficiency  $LDE(\lambda, x)$  a relation between wavelength (photon energy) and local detection efficiency is needed. This allows inversion of Eq. (3.2) to find  $LDE(\lambda, x)$  given the measured

$LDE(\lambda)$  as a function of wavelength. Our experimental work in SSPDs [30, 38] shows that the photon-detection probability depends exponentially on bias current, and that a linear relation exists between photon energy and bias current for a certain internal detection efficiency [25, 38]. Based on these observations we postulate a similar bias current dependence of the microscopic  $LDE(\lambda, x)$ :

$$LDE(\lambda, x) = \min\{1, \exp[(I_b - I_{th}(\lambda, x))/I^*]\}, \quad (3.3)$$

with a threshold current defined as

$$I_{th}(\lambda, x) = I_c - \gamma'(x) \frac{hc}{\lambda}. \quad (3.4)$$

Here  $hc/\lambda$  is the photon energy and  $I^* = 0.65 \mu\text{A}$  is an experimentally determined current scale for our detector [38].  $\gamma'(x)$  is the local energy-current interchange ratio, which parameterizes the internal detection efficiency of the nanowire at different excitation wavelengths, and translates to a threshold current  $I_{th}(\lambda, x)$  that is sufficient to quantify this local internal efficiency [25]: when the bias current  $I_b$  exceeds  $I_{th}(\lambda, x)$  with a photon absorbed at position of  $x$ , the energy barrier for a vortex vanishes, leading to the entry of the vortex and to a detection event.

In practice, instead of using  $LDE(\lambda, x)$  for fitting the measured visibility  $V_{IDE}$  we employ  $\gamma'(x)$  as fitting parameter. The outcome should be comparable to the detailed calculation based on quasiparticle-diffusion and vortex-crossing, as introduced in Appendix I.

Figure 3.6 shows the measured visibility  $V_{IDE}$  as a function of wavelength (squares), a best fit (red), a fit with a constraint (green) and the results of a calculation using the function  $\gamma'(x)$  predicted by numerical modeling of the detection process. The details of the fit procedure are given in Appendix II. The original fit (red) is based on Eqns. (3.2) and (3.3) as discussed above with fitting parameters  $\gamma'(x)$  at discrete positions  $x$ . Mirror symmetry of  $\gamma'(x)$  and a parametrization with 9 points is sufficient to capture all details observed in the experiment. The results for  $I_{th}(x)$  at  $\lambda = 1500 \text{ nm}$  derived from the fitted values of  $\gamma'(x)$  are shown in Fig. 3.7(a), the curve (red) contains a distinct minimum at  $x = \pm 40 \text{ nm}$ .

To verify whether these minima are robust we constrain  $\gamma'(x)$  to monotonically vary from the center of the nanowire to the edge. In Fig. 3.7(a), the green curve shows the variation in  $I_{th}(x)$  under these constraints. However, Fig. 3.6 shows that the visibility (green) is only marginally affected by constraining  $\gamma'(x)$ . This analysis suggests that the spatial variations in the threshold current close to the edge can not be extracted in great detail.

A different point is how our results compare with theory. This comparison is shown both in Figs. 3.6 and 3.7(a), where the blue curves represent the

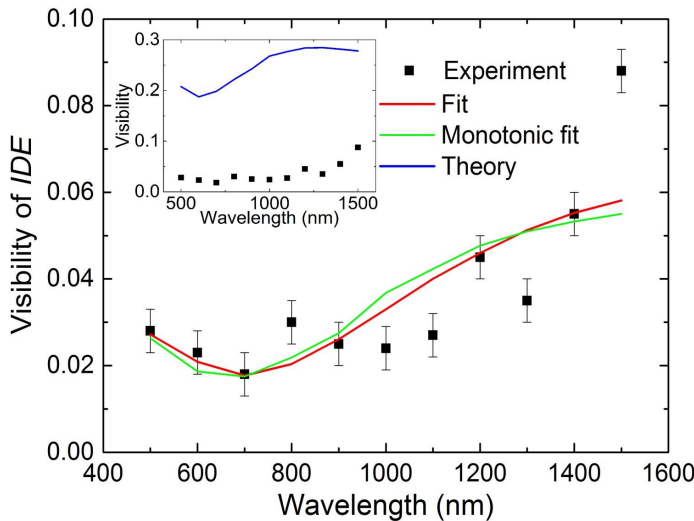


Figure 3.6: Visibility of internal detection efficiency and fit. For each wavelength the visibility is averaged from all the currents. The red curve is the fit by considering the distribution of absorption and internal detection efficiency, and the green curve is the fit by considering a constraint to make the variance of local detection efficiency monotonic from the center of the nanowire to the edge. The blue curve in the inset shows the visibility calculated based on the photon detection theory [25].

predictions by the numerical model of the detector. We find that the visibility is a factor of 10 larger (inset of Fig. 3.6), and that the threshold current from the numerical calculation has a notably stronger edge/center contrast (Fig. 3.7)(a).

The comparison of the results from experiment and numerical modeling brings up the following question: “Is there a link between the wavelength averaged value of the  $V_{IDE}$  and the width of the main feature of the threshold current  $I_{th}(x)$  as shown in Fig. 3.7(a)?”

To answer this question we determine  $I_{th}(x)$  for various values of  $V_{IDE}$  assumed to be wavelength independent, with  $0.03 < V_{IDE} < 0.3$ . The results are shown in Fig. 3.7(b), in support of our conjecture that a broader profile of  $I_{th}(x)$  leads to a sharper contrast between the edge and the center of the nanowire, and to a larger visibility consequently.

Finally, in Fig. 3.7(c) we show, using the results of Fig. 3.7(a) how the  $LDE(x)$  varies with the location of the photon absorption. The results are shown based on both the experimental data (solid, red) and the numerical calculations (dashed, blue), for different values of the bias current. Note that the relatively small spatial variations in the  $I_{th}(x)$  translate in much larger variations in  $LDE(x)$ , up to factors 10 – 20. Also note that the detector saturates at the edges before saturating at the center.

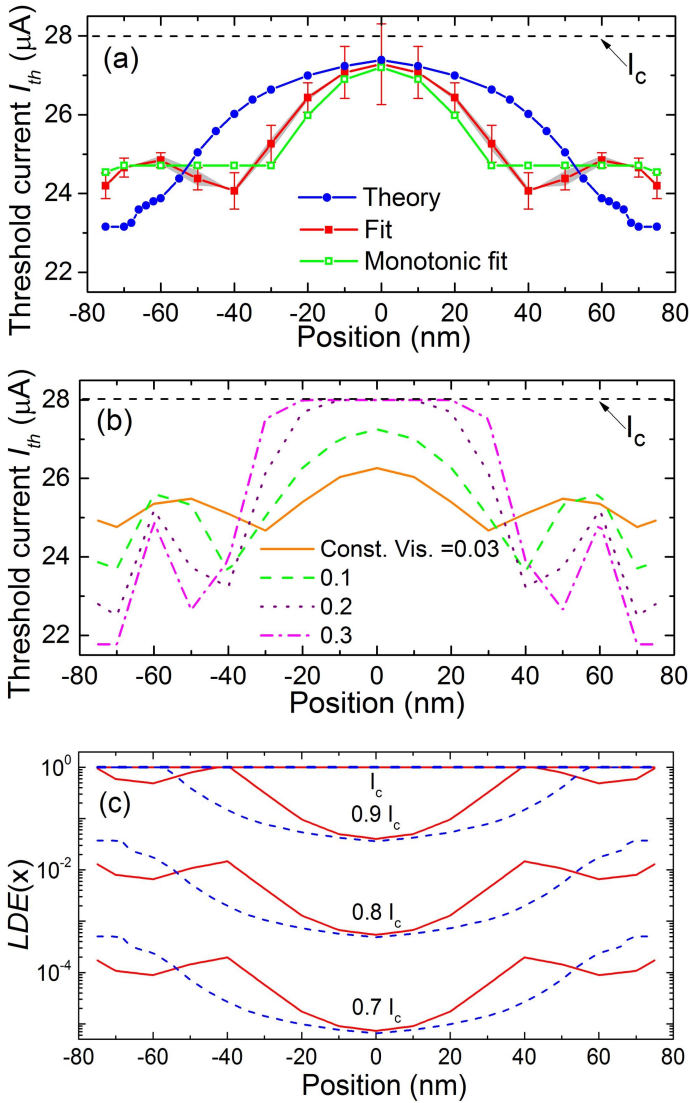


Figure 3.7: Threshold current and local detection efficiency at wavelength of 1500 nm. (a) shows the threshold current obtained from experiments (open and closed squares) and theory (dots). The grey area on the solid curve indicates the systematic error from calculation of optical absorption. The monotonic fit is obtained by using a constraint to make the fitting parameters monotonic from the center of the nanowire to the edge. (b) shows the threshold current by fitting a set of constant visibility from 0.03 to 0.3. (c) shows the local detection efficiency based on (a) : solid lines from experiment and dashed lines from theory.

## 3.6 Conclusions

We have separated the polarization-dependent internal detection efficiency from the optical absorption of an SSPD via quantum detector tomography. The internal detection efficiency is constructed by the optical absorption and position-dependent local detection efficiency, which depends on the position along the cross section at which the photon is absorbed. We have probed this effect with a resolution of approximately 10 nm, and found agreement with theoretical calculations done in the context of the quasiparticle-diffusion-based vortex-crossing model. Compared to the theory, we have confirmed that a narrower profile of threshold current is able to fit the experimental data. Within a range of  $\sim 30$  nm close to the edge of the nanowire the local detection efficiency is much higher than at the center, which is relevant to the scale of the quasiparticle diffusion after photon absorption. These experimental conclusions support the model of quasiparticle diffusion and vortex entry, and quantitatively describe the photon-detection process in the NbN nanowire SSPD on the nanoscale.

### 3.7 Appendix I: Photon detection mechanism

In the main text of Chapter 3, we use a quasiparticle-diffusion and vortex-crossing model to describe the photon detection process in a NbN superconducting single-photon detector. This appendix summarizes the model originally presented in Ref. [24] with a few additions to make the model more realistic. This model assumes that the photon excites one electron with energy  $hc/\lambda$ . The excited electron diffuses in the plane of the film with a diffusion constant  $D_e$ , and thermalizes via inelastic scattering with other electrons, Cooper-pairs and the lattice. Neglecting details of this thermalization process, an exponential increase of excess quasiparticles is assumed with a time constant  $\tau_{qp}$  and an overall efficiency  $\varsigma$  [22]. The excess quasiparticles themselves are also subject to diffusion with a temperature-dependent diffusion constant  $D_{qp} < D_e$  and eventually recombine to form Cooper-pairs on a time-scale  $\tau_r > \tau_{qp}$ . The entire process can be described by the following coupled differential equations [24]:

$$\frac{\partial C_e(r, t)}{\partial t} = D_e \nabla^2 C_e(r, t) \quad (\text{A.1})$$

$$\frac{\partial C_{qp}(r, t)}{\partial t} = D_{qp} \nabla^2 C_{qp}(r, t) - C_{qp}/\tau_r + \frac{\varsigma h\nu}{\Delta \tau_{qp}} \exp(-t/\tau_{qp}) C_e(r, t) \quad (\text{A.2})$$

with  $\Delta$  the superconducting gap,  $C_e(r, t)$  the probability density to find the excited electron at position  $r$  at time  $t$  after photon absorption and  $C_{qp}(r, t)$  the quasiparticle density.

An estimation of the Ginzburg-Landau relaxation time results in  $\tau_{GL} < 1$  ps. Therefore, we assume the current redistribution due to the spatial variation of the density of superconducting electrons  $n_{se} - C_{qp}(r, t)$  to be instantaneous on time scales  $> 1$  ps. To obtain a more realistic current-distribution than in Ref. [24], we now apply the relation that the velocity of superconducting electrons can be calculated from the gradient of the phase of the superconducting condensate [25]:

$$v_s = \frac{\hbar}{m} \nabla \varphi \quad (\text{A.3})$$

with a corresponding current density

$$j_s = -en_{se} \frac{\hbar}{m} \nabla \varphi \quad (\text{A.4})$$

and the continuity equation that needs to be solved:

$$\nabla \cdot (-en_{se} \nabla \varphi) = 0, \quad (\text{A.5})$$

where we use the previously calculated quasiparticle distribution to obtain  $n_{se}$ . Additionally, we take into account that the density of superconducting electrons depends on the velocity  $v_s$  [73].

$$n_{se} \propto 1 - (v_s/v_c)^2/3, \quad (\text{A.6})$$

with  $v_c$  the critical velocity at the critical-current density  $j_c$ . Thus Eq. (A.5) becomes nonlinear. Once we know the current distribution, the potential energy experienced by a vortex can be calculated as suggested in Ref. [41]. More details about the refined numerical model can be found in Ref. [25].

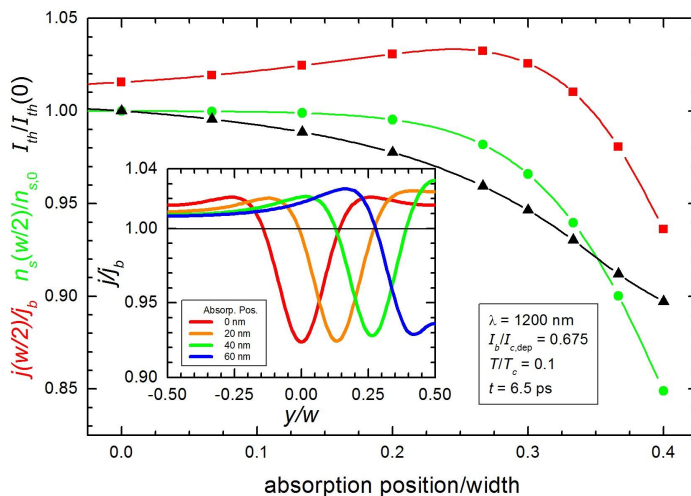


Figure A.1: Variation of reduced current density at the edge  $j(w/2)/j_b$ , normalized density of superconducting electrons  $n_s(w/2)/n_{s,0}$ , and rescaled threshold current for photon detection as a function of the distance of the photon absorption position from the center of the wire. The variation of the threshold current near the center of the wire is dominated by the variation of the current density at the edge. For absorption events closer to the edge the reduction of the density of superconducting electrons becomes the dominating effect. In the inset we show the variation of the current density across the wire for different absorption positions.

In the inset of Fig. A.1 we plot reduced current densities  $j/j_b$  across the strip for some absorption positions. At first, current densities increase with decreasing distance of the absorption position to the near edge. If the distance becomes less than 20 nm to the edge the current density near the edge is reduced, eventually below the equilibrium bias current density  $j_b$ .

In the main graph of Fig. A.1 the reduced current density at the edge  $j(w/2)/j_b$  is plotted as a function of absorption position, together with the density of superconducting electrons at the edge  $n_s(w/2)$  normalized to their equilibrium

density  $n_{s,0}$ , and the threshold current scaled by the threshold current for absorption in the center  $I_{th}/I_{th}(0)$ . For absorption events near the center, the variation of the threshold current is mostly determined by the variation of the current density at the edge, since the density of superconducting electrons at the edge remains approximately constant. At close distances to the edge  $n_s$  is significantly reduced at the edge. This is the reason for a reduced current density at the edge, but additionally leads to a reduction of the vortex self-energy which is proportional to  $n_s$ . This second effect is stronger than the effect of the reduced current density and as a result we obtain a monotonic reduction of the threshold current for vortex entry as a function of the distance from the strip center.

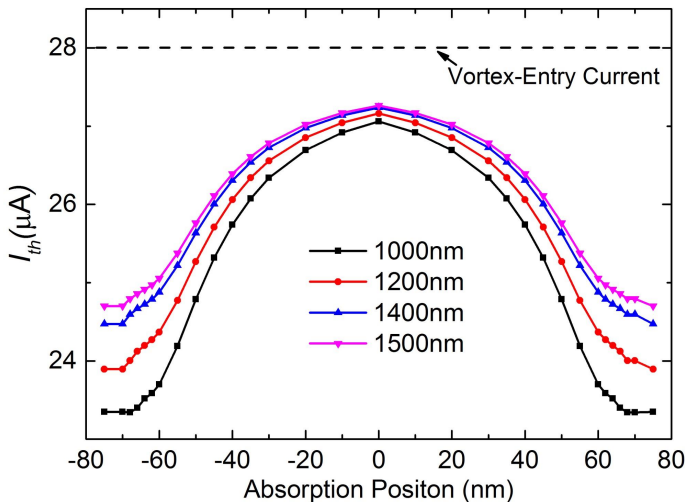


Figure A.2: Calculated threshold current as a function of the distance of the photon absorption position from the center of the wire for different photon wavelengths. The relative reduction of the threshold current for absorption near the edge compared to absorption in the center increases with increasing photon energy for the energy range considered in this study.

We define the threshold current as that value of the bias current for which the maximum potential energy for a vortex becomes zero. In this case we expect an internal detection efficiency equal to one. With this criterion, we obtain the energy dependence of the threshold current as a function of position, which is plotted in Fig. A.2. The vortex-entry current without photon absorption is also indicated by the horizontal line. This curve is symmetric with respect to the center line of the wire due to the symmetry between vortices and antivortices in zero applied magnetic field. There is a significant reduction of the threshold current for photons absorbed near the edge of around 10% as compared to the center of the wire. We would like to point out that for each position in the

wire we find a linear relation between threshold current and photon energy, consistent with previous experimental results [30, 38, 74].

As the photon energy increases and as absorption occurs closer to the edge, the relation between the density of superconducting electrons and the current distribution (Eqns. (A.5) and (A.6)) becomes more nonlinear. For absorptions very close to the edge, the nonlinear solver produces systematic errors. For all wavelengths, we do not calculate the detection current for absorption sites closer than one coherence length ( $\xi \approx 4\text{--}5$  nm for NbN) to the edge of the wire. For short wavelengths, the area in which this occurs increases, to approximately 12 nm from each edge at 800 nm. In our calculations, we assume that the detection current this close to the edge of the wire is weakly dependent on the absorption position and set it constant, with a value equal to the threshold current in the point closest to the edge that we can still reliably compute. In our experiment, we are operating below this threshold current. To convert the threshold current into a local detection efficiency, we assume a functional dependence of the form  $p \equiv IDE = \exp((I_b - I_{th})/I^*)$ ; where  $I^* = 0.65 \mu\text{A}$  is an experimentally determined scaling current. In this way, we obtain the variation of the internal detection efficiency for a given bias current as shown in the Fig. 3.7(c) in the main text.

### 3.8 Appendix II: Fit to visibility

The photon detection mechanism in Appendix I shows that the probability of vortex entry depends on the position of the photon absorption. Hence, we use the position-dependent local detection efficiency  $LDE(\lambda, x)$  to quantify the microscopic detection process. We assume that the internal detection efficiency  $IDE$  as a function of wavelength can be constructed as follows:

$$IDE_k(\lambda) = \frac{\int A_k(\lambda, x)LDE(\lambda, x)dx}{\int A_k(\lambda, x)dx}, \quad (\text{A.7})$$

where  $k$  stands for either parallel or perpendicular polarization,  $A_k(\lambda, x)$  is the absorption distribution obtained by FDTD simulation at an incident wavelength of  $\lambda$ , and the  $LDE(\lambda, x)$  is the efficiency to trigger the detector for the absorbed photon with energy  $hc/\lambda$  at position  $x$ . In the integral, the absorption profile  $A_k(x)$  is normalized in order to remove the dependence on average absorption probability  $\int A_k(\lambda, x)dx$ , because the average absorption (effective absorption efficiency)  $\eta$  is separated from the  $IDE$  via quantum detector tomography.

For a certain wavelength, we find that  $IDE$  depends exponentially on bias current  $I_b$ , which is supported by experiment in this work and a previous study [38]. Therefore we use a microscopic  $LDE(\lambda, x)$ :

$$LDE(\lambda, x) = \min\{1, \exp[(I_b - I_{th}(\lambda, x))/I^*]\}, \quad (\text{A.8})$$

where  $I^* = 0.65 \mu\text{A}$  is an experimentally determined current scale.

In order to combine the information from different wavelengths, we posit a relation between photon energy and the threshold current  $I_{th}(\lambda, x)$  [25, 30]:

$$I_{th}(\lambda, x) = I_c - \gamma'(x)\frac{hc}{\lambda}, \quad (\text{A.9})$$

where  $I_c$  is the critical current,  $hc/\lambda$  is the photon energy, and  $\gamma'(x)$  is the local energy-current interchange ratio, which parameterizes the detection probability of the wire at different excitation wavelengths. The assumption is based on the fact of the linear relation of bias current and incident energy of photon.

The assumptions leading to Eqns. (A.8) and (A.9) make it possible to perform a numerical inversion. From the measured wavelength dependence we obtain the parameters  $\gamma'(x)$  via fitting the experimental data. We use mirror symmetry about  $x = 0$  and 9 points for  $\gamma'(x)$ . We use the following procedure:

- 1) The strongly position-dependent  $A_k(\lambda, x)$  is calculated with a spatial resolution of 1 nm by FDTD simulation. Therefore, to calculate the integral of Eq. (A.7) we linearly interpolate  $\gamma'(x)$  on a 1 nm grid, from the points at which it is given. We assume mirror symmetry around point  $x = 0$ .

2) For each wavelength, we compute  $I_{th}(\lambda, x) = I_0 - \gamma'(x) \frac{hc}{\lambda}$ , and take  $I_0$  to be  $I_{c,exp} = 28 \mu\text{A}$ , in accordance with the theoretical predictions of the vortex-crossing model.

3) For each current and wavelength, we compute the local detection efficiency:  $LDE(\lambda, x) = \min\{1, \exp[(I_b - I_{th}(\lambda, x))/I^*]\}$ .

4) Compute  $IDE_k(\lambda)$  according to Eq. (A.7) and the visibility  $V = (IDE_{\parallel} - IDE_{\perp}) / (IDE_{\parallel} + IDE_{\perp})$ .

In order to fit the visibility to the experimental data, we use Tikhonov regularization [75]. That is, to the usual function that is minimized in an inversion problem

$$g(x) = \sum (V_i(\gamma'(x)) - V_{i,exp})^2 / \sigma_i^2, \quad (\text{A.10})$$

where  $V_{i,exp}$  is the observed visibility and  $\sigma$  is the error on each visibility. We add an extra term, replacing  $g(x)$  by

$$g(x) = \sum (V_i(\gamma'(x)) - V_{i,exp})^2 / \sigma_i^2 + s \sum (\gamma'(x_j) - \gamma'(x_{j+1}))^2, \quad (\text{A.11})$$

which has the effect of penalizing solutions where the difference between adjacent points in the curve is large. We apply only weak regularization such that the contribution to  $g(x)$  from the second term is approximately 20% of the first. Furthermore, we apply the constraint that the sum  $\gamma'(x)$  should be equal to the sum of the theoretical  $\gamma'(x)_{theo}$  curve. We find that we can fit our data if we set  $\sum \gamma'(x) \Delta x_i = 1.15 \sum \gamma'(x)_{theo} \Delta x_i$ . We varied the number of points and value of  $s$  and verified that the solution presented in the main text is robust against the small variation in the parameter  $s$ .



## Chapter 4

# Optimal Design of NbN Superconducting Single-Photon Detectors

The microscopic detection mechanism in superconducting single-photon detectors causes the internal detection efficiency to depend on the position where the single photon is absorbed. This effect, together with the polarization-dependent optical absorption causes the detector response to be polarization dependent. We calculate the response of meandering wire NbN detectors by considering the optical response obtained from finite-different-time-domain simulations and the local detection efficiency measured by J. J. Renema et al. [Nano Lett. vol. 15, p. 4541, 2015] as input. The calculations show good agreement with experimentally measured polarization dependence in the internal detection efficiency of meandering wire detectors that were hitherto not understood. By considering the spatially non-uniform absorption in the wire we estimate an optimum wire width of 90 nm for detection of single photons at 1550 nm for light polarized with the  $E$ -field perpendicular to the wire<sup>1</sup>.

### 4.1 Introduction

Superconducting single-photon detectors (SSPDs) [14] consist of a meandering nanowire made out of superconducting material through which a bias

---

<sup>1</sup>Q. Wang, et al. in preparation for publication.

current ( $I_b$ ) is passed. Typically, this current is comparable in magnitude to the device critical current ( $I_c$ ) below which the wire is superconducting. Absorption of a single photon of visible light is then sufficient to switch part of the wire from the superconducting to the normal state. This resistive state creates a voltage pulse that can be amplified and detected with pulse counting electronics. An appropriate design of the biasing electronics removes the current from the device in the normal state, allowing the detector to self-reset to the superconducting state on a nanosecond timescale [33].

The specific benefits of these detectors are their broad spectral range (from visible to infrared wavelengths) [18], combined with low dark-count rates [15], excellent timing resolution [16], and high detection efficiency [17]. This makes these detectors very suitable for use in quantum optics [76], quantum communication [77], and in the life sciences [63]. The optical response of these detectors under normal illumination is limited by the large impedance mismatch of the superconductor to vacuum or a dielectric [65]. For light incident from vacuum, this limits the maximum possible absorption efficiency to 50%. This limitation can be overcome by introducing a cavity structure that increases the absorption efficiency for wavelengths that are resonant to the cavity design [78], and device efficiencies up to 93% have been reported [17].

Recently, detector tomography on NbN *single nanowire* devices has been performed and has revealed a linear energy dependence of the detection probability [30]. This linear energy dependence can be explained by a microscopic detection model that uses quasiparticle diffusion and photon-assisted vortex entry [25, 30]. An important consequence of this microscopic detection model is that the photon detection efficiency depends on the position where the photon is absorbed because a photon absorbed in the middle of the wire affects the barrier for vortex entry to a much smaller extent than a photon absorbed at the edge of the wire. Using polarization resolved detector tomography [35] we were able to separate the effective absorption efficiency ( $\eta$ ) of a nano-fabricated constriction from the internal detection efficiency ( $IDE$ ). To capture the details of the microscopic detection mechanism a local detection efficiency ( $LDE(x)$ ) that depends on the position  $x$  of photon absorption across the wire is introduced.

This  $LDE(x)$  can be reconstructed from the measured  $IDE$  as a function of wavelength and polarization. To achieve this we use the numerically calculated position and polarization dependent absorption and an assumed linear exchange between current density and photon energy for each position across the wire [35]. This numerical inversion procedure leads to an estimate of the local detection efficiency that indeed predicts that photon absorption events occurring at the edge of a 150 nm wide wire are much more likely to produce a detection event than those in the middle. From these experiments we find that this “edge effect” extends roughly 30 nm into the wire, i.e., significantly

more than what was expected based on the theoretical predictions resulting from the microscopic model. An open question is whether, and to what extent the extracted spatially non-uniform  $LDE(x)$  impacts the detection efficiency of *meandering* wire detectors.

To answer this question we compare the predictions based on the measured  $LDE(x)$  to experimental data on the polarization-dependent absorption and detection efficiency of a set of meandering NbN SSPDs by Anant et al. [42]. These data show that the internal detection efficiency is less than 100% in state-of-the-art devices and depends on polarization. In this chapter we show how the  $LDE(x)$  as determined in Chapter 3 can be used to quantitatively explain the measurements of Anant et al. Armed with a better understanding of the microscopic detection model we discuss the implications for the design of SSPDs to maximize photon detection efficiency for both polarizations. This design is a compromise between absorbing the photons at the edge of the wire where the  $LDE(x)$  is maximum and optimizing the total absorption of the wire in a meander structure. We find that the optimal wire width for a NbN meandering SSPD operating at 1550 nm is  $\sim 90$  nm for polarization perpendicular to the wire, roughly three times the experimentally observed edge effect.

## 4.2 Photon detection process in NbN SSPDs

Absorption of a photon leads to the excitation of a single electron in the superconductor. For photon energies that are much higher than the superconducting gap this electron is strongly localized on a length scale well below the wavelength of the light. The energetic electron thermalizes via inelastic scattering with other electrons, Cooper pairs and the lattice, leading to a localized excitation of the superconductor [25].<sup>2</sup>

Within the photon-assisted vortex-entry model, the thermalization process of the electron leads to a cloud of quasiparticles that diffuses in the superconductor and leads to a local decrease of the superconducting electron density (without creating a normal state). Because the potential barrier for vortex entry depends on the superconducting electron density, the probability for entry of a vortex from the edge of the wire is increased. Energy dissipation by

---

<sup>2</sup>We use photon-assisted vortex entry as the microscopic mechanism to explain a detection event. This choice is motivated by experimental observations that the current needed to get a 1% detection efficiency depends linearly on the total energy of the excitation [30]. The vortex is an essential ingredient to explain the experimental observation that the current extrapolated to zero photon energy does not correspond to the device critical current [25,30]. Photon-assisted vortex entry predicts that detection of a zero energy photon occurs at  $\sim 0.8$  times the depairing current of the superconductor and also explains the observed temperature dependence [30].

the moving vortex breaks the superconducting state and triggers a photon detection event. An absorption event at the edge lowers the superconducting electron density at the edge of the wire and diverts supercurrent towards the center of the detector. Photon absorption in the center of the wire has little influence on the superconducting electron density at the edge of the wire, but diverts supercurrent towards the edge of the wire. For a NbN wire the lowering of the superconducting electron density at the edge is the dominant contribution to the decrease of potential barrier for vortex entry, therefore photon detection at the edge of the wire is more efficient than in the center. It thus becomes necessary to introduce a local detection efficiency  $LDE(x)$  as a function of position  $x$  across the wire.

It is well-known that the response of an SSPD depends on photon energy and device bias current. For a constant photon energy, the response increases exponentially as a function of bias current and saturates above a threshold current. Following Ref. [35] we posit a relation between the local detection efficiency  $LDE(x)$ , bias current  $I_b$  and threshold current  $I_{th}(x)$ , where the position dependence is expressed through the position dependence of the threshold current:

$$LDE(x, I_b) = \min\{1, \exp[(I_b - I_{th}(x))/I^*]\}, \quad (4.1)$$

where  $I^*$  is a current scale that can be extracted from experiments by fitting the internal detection efficiency  $IDE$  as a function of  $I_b$ . In this chapter we use a value of  $I^* = 0.65 \mu\text{A}$  based on the experimental data in Ref. [35].  $LDE(x)$  changes with different parameters of  $I_b$  is well described by Eq. (4.1). We limit the discussion to single-photon detection at a constant wavelength of 1550 nm, allowing us to ignore the fact that the threshold current depends on photon energy.

The empirical model discussed above is sufficient to describe measured results on a NbN single wire SSPD [35], as well as numerical calculations of the detection process based on the photon-assisted vortex-entry model. The  $LDE(x)$  derived from experiments indicates that the detection efficiency is roughly constant for distances up to  $\sim 30$  nm from the edge of the wire, while numerical results indicate a much more rapid decrease in the detection efficiency. Currently, the difference between these two curves is not understood. Throughout this chapter we use the experimentally determined values because we intend to discuss the implications of  $LDE(x)$  on the performance of meandering detectors and future detector design.

### 4.3 Optical absorption and detector response

To calculate the response of a meandering SSPD both the local detection efficiency  $LDE(x)$  and the spatial distribution of optical absorption  $A(x)$  need to be taken into account. The  $LDE(x)$  determines the probability to generate a click once a photon is absorbed at position  $x$  and contains the detailed physics of the microscopic detection model. The factor  $A(x)$  determines the macroscopic probability to absorb the photon at position  $x$  and can be calculated to good accuracy using standard numerical procedures to solve Maxwell's equations. We use finite-difference-time-domain (FDTD, Full-Wave package, RSoft [71]) simulations in two dimensions by approximating a meandering SSPD by an infinitely large array of wires via imposing periodic boundary conditions. We ignore bends in the meandering wire and limit ourselves to a plane wave incident at normal incidence. The first approximation is justified because in an actual SSPD the area covered by straight wire is much larger than the area of the bends. In addition, the central part of the meander is illuminated by making the light spot (diameter of  $\sim 10 \mu\text{m}$ ) slightly smaller than the meander size. The assumption that the optical absorption of a meandering detector is well described by plane-wave illumination at normal incidence relies on the fact that the illuminating beam has a small numerical aperture ( $\sim 0.1$ ) and that the absorption is to first order independent of angle of incidence near normal incidence [65].

Figure 4.1(a) shows the cross section (not to scale) of a repeat unit (width  $p$ ) of the periodic structures used in the FDTD calculation. A 4.35 nm thick NbN nanowire (width  $w$ ) with a 2 nm thick oxide layer of  $\text{NbN}_x\text{O}_y$  lies on top of a semi-infinite sapphire substrate. The fill factor  $f$  of the wires in a meandering wire is defined as  $w/p$ . The refractive indices of all the materials are taken from Ref. [42]:  $n_{\text{sapphire}} = 1.75$ ,  $n_{\text{NbN}} = 5.23 + 5.82i$ , and  $n_{\text{NbNO}} = 2.28$ . In the calculation, a plane wave, at wavelength of 1550 nm, illuminates the structure from the top ( $y$ -direction) and has the electric field either parallel ( $\parallel$ ) or perpendicular ( $\perp$ ) to the wire. The simulation area is bound by a perfectly matched layers (PML) on top and beneath the structure. The boundary conditions on the left and right boundary (see B.C. in Fig. 4.1(a)) can be set to PML to calculate the properties of an isolated wire or to periodic boundary condition to calculate the properties of a meandering structure.

The  $\sim 4$  nm thick NbN film is much thinner than the skin depth of  $\sim 90$  nm at the relevant wavelength of 1550 nm. Hence, the absorption distribution is uniform over the thickness of the film and is a function of position  $x$  across the nanowire only and can be expressed as follows [79]

$$A(x) = \frac{P_{\text{abs}}(x)}{P_{\text{total}}/w} = \frac{\int_0^t \frac{1}{2} \omega \varepsilon_o \text{Im}(\varepsilon_{\text{NbN}}) |E(x, y)|^2 dy}{P_{\text{total}}/w}, \quad (4.2)$$

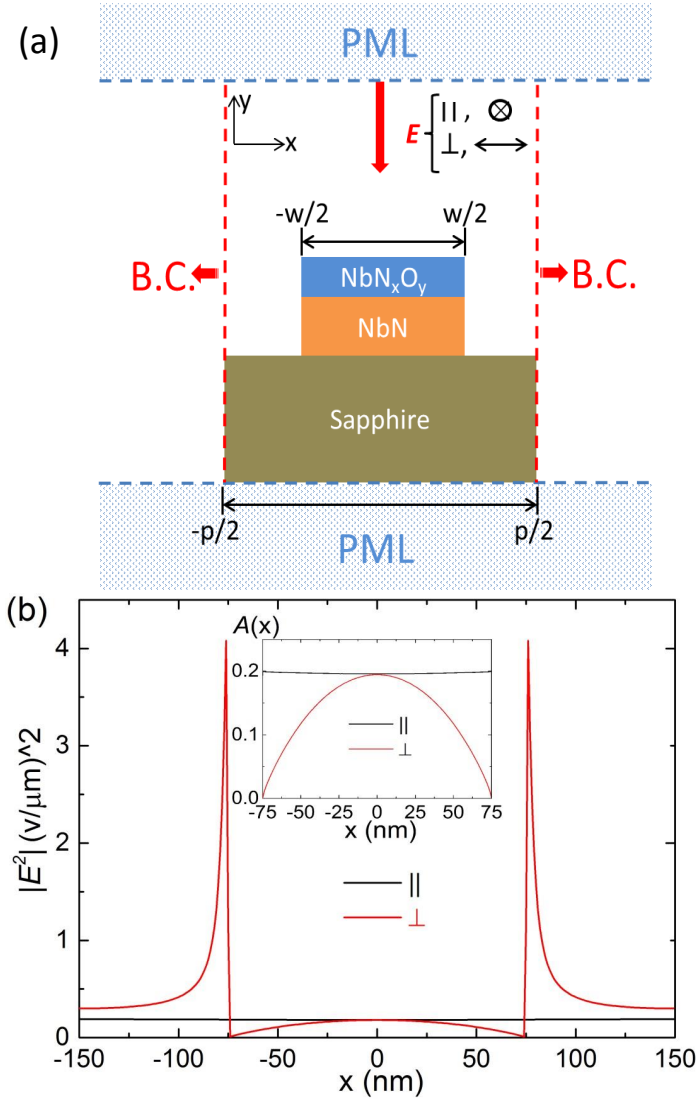


Figure 4.1: (a) Cross section of a simulation cell in the 2D FDTD calculation. The boundary conditions at  $x = \pm p/2$  are adapted to simulate either a periodic array of wires or an isolated wire. Inside the computational cell the 4.35 nm thick NbN wire ( $n_{\text{NbN}} = 5.23 + 5.82i$ ) with width  $w$  is sandwiched between a semi-infinite sapphire substrate ( $n_{\text{sapphire}} = 1.75$ ) and a 2 nm thick oxidation layer  $\text{NbN}_x\text{O}_y$  ( $n_{\text{NbNO}} = 2.28$ ). A linearly polarized plane wave with a wavelength of 1550 nm and  $E$ -field either parallel ( $\parallel$ ) or perpendicular ( $\perp$ ) to the wire is incident from the top of the structure. (b) Calculated intensity distribution  $|E^2|(x)$  for a periodic array of 150 nm wide wires with a pitch  $p = 300$  nm. The field distribution for parallel polarization is almost uniform, while the distribution for perpendicular polarization shows two strong discontinuities caused by singularities occurring at the edges of the NbN wire. The inset shows the absorption distribution inside the NbN wire in more detail.

where  $w$  is the width of the wire,  $P_{total}/w$  is the power density of illumination across the wire,  $P_{abs}(x)$  is the absorbed power density as a function of position  $x$  across the wire width,  $\omega$  is the angular frequency of the incident light,  $\varepsilon_o$  is the vacuum permittivity,  $t = 4.35$  nm is the thickness of the NbN film, and  $|E(x, y)|^2$  is the electric field intensity in the wire.

As an example, Fig. 4.1(b) shows the time averaged  $|E(x)|^2$  across a  $w = 150$  nm wide wire in a meander with a  $p = 300$  nm wide pitch. For illumination with parallel polarization,  $|E(x)|^2$  is almost constant over the entire unit cell. For perpendicular polarization, singularities in the field appear at the edge of the wire ( $x = \pm 75$  nm). The singularities originate from the electric field distribution around the sharp right-angle wedges of the wire. The inset shows the optical absorption distribution  $A(x)$  inside the wire in more detail. It is important to note that the highly non-uniform spatial distribution of the absorption in case of perpendicular polarization is related to the edges of the wire, and that the calculated profile  $A(x)$  for periodic structures is very similar to a calculation for a single wire [35] provided that the pitch of the meander is smaller than the wavelength.

We obtain the  $LDE(x)$  from Eq. (4.1) using the experimentally determined value of  $I_{th}(x)$  for photons with a wavelength of 1550 nm (0.8 eV energy) [35]. Figure 4.2(a) shows the results of the  $LDE(x)$  at bias currents  $I_b = 0.8I_c$ ,  $0.9I_c$  and  $I_c$ . As can be seen in the figure, the edges of the wire have much higher local detection efficiency than that of the center for sufficiently low bias currents. As the bias current increases, the detection efficiency at the edge starts to saturate. For currents close to the critical current  $LDE(x)$  becomes equal to unity over the entire width of the wire. It is important to note that the values of the critical currents and threshold currents used to define  $LDE(x)$  refer to those of a nanodetector (see Chapter 3). For longer wires, inhomogeneities and other imperfections in the wire directly limit the device critical current. The threshold current is affected in a different way because the sections of wire that are not biased close to their critical current will still detect photons. As a result the ratio between the device critical current and the threshold current for a meandering wire is expected to be closer to one than the same ratio for a nanodetector.

Similar to the short wire calculation, we assume that the overall detection probability or the response of a meandering SSPD can be expressed by:

$$R(I_b) = \frac{\int_{-w/2}^{w/2} A(x) \cdot LDE(x, I_b) dx}{w} \quad (4.3)$$

where  $w$  is the width of the wire.

Figure 4.2(b) shows the response distribution  $r(x) = A(x) \cdot LDE(x, I_b)$  for both polarizations. The solid and dashed curves correspond to parallel and

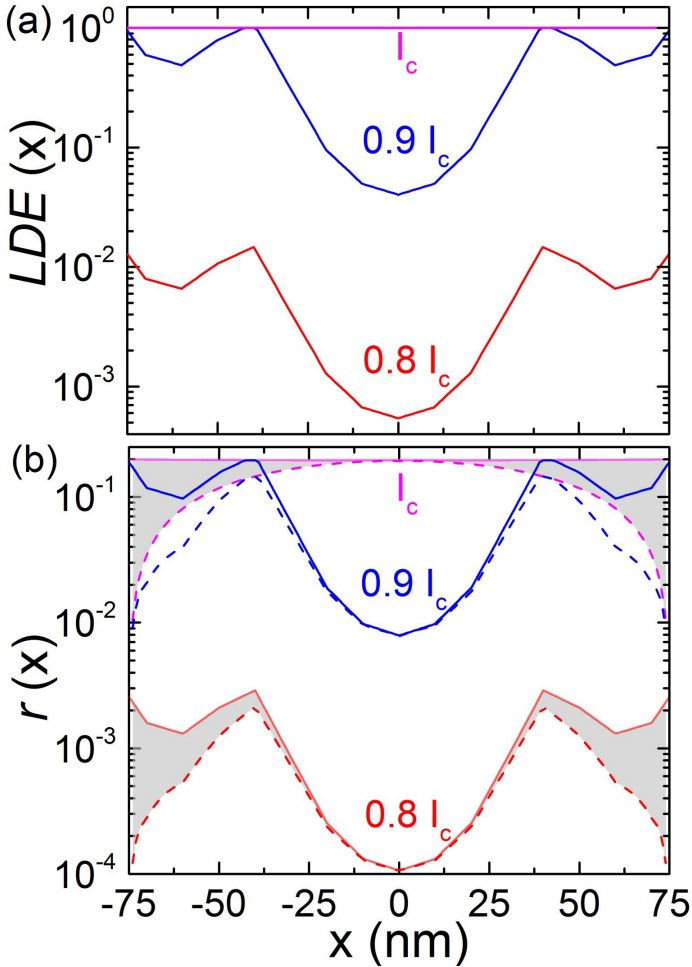


Figure 4.2: (a) Local detection efficiency across the 150 nm wide NbN wire at values of the bias current equal to  $0.8I_c$ ,  $0.9I_c$  and  $I_c$ . The curves are determined experimentally in Ref. [35]. (b) Detection response distribution across the 150 nm wide NbN wire at the same bias currents as shown in (a). The solid and dashed curves represent parallel ( $\parallel$ ) and perpendicular ( $\perp$ ) polarization, respectively. The grey area between the solid and dashed curves at bias currents of  $0.8I_c$  and  $I_c$  shows the difference of the local response between the two polarizations. For reasons of clarity the area between the two curves at  $0.9I_c$  is not filled. The curves at  $0.9I_c$  are used to produce the results in the remaining of this chapter.

perpendicular polarization, respectively. The calculated response distribution is plotted for various values of the bias currents ( $I_b = 0.8 I_c$ ,  $0.9 I_c$  and  $I_c$ ). For the highest bias current, i.e.,  $I_b = I_c$ , the  $LDE(x)$  equals to one over the wire, and the response distribution  $r(x)$  reflects the profile of the absorption distribution  $A(x)$ , which is shown in the inset of Fig. 4.1(b). The areas between the solid and dashed curve for each bias current (e.g., filled with grey for  $0.8I_c$  and  $I_c$ ) illustrate the difference in local response between the two polarizations. The detector response  $R(x, I_b)$  is then calculated by the integral of the local response  $r(x)$  as given by Eq. (4.3). In the following sections we use the  $LDE(x)$  at a bias current of  $0.9I_c$  to calculate the detector response for other geometries of meandering SSPDs, because this value of bias current gives the best agreement with the data presented in Ref. [42].

## 4.4 Results

### 4.4.1 Detector response for SSPDs with a constant wire width

Figure 4.3 shows the calculated detector response  $R$  as a function of the average optical absorption for a set of meander structures with a constant wire width  $w$  and different values of the pitch  $p = 150$  nm,  $200$  nm,  $300$  nm,  $400$  nm and  $500$  nm. The average optical absorption is straightforwardly calculated by averaging the absorption distribution:

$$\bar{A} = \frac{1}{w} \int_{-w/2}^{w/2} A(x) dx.$$

The solid, diagonal line with slope one indicates a detector with 100% internal detection efficiency for which each absorbed photon triggers the detector. Calculated data points for meander structures illuminated with parallel polarization (solid circles) and perpendicular (open circles) are shown and are fitted to a linear dependence. The fact that the detector response is proportional to the average absorption implies that meandering wires of constant width but different pitches have the same internal detection efficiency of the wire. For a constant wire width, the absorption distribution  $A(x)$  resembles that of an isolated wire and is very similar for structures with different pitches.

For both polarizations, the average absorption  $\bar{A}$  is mainly determined by the fill factor  $f$ , which is given by the ratio of wire width  $w$  over the pitch  $p$ , and increases as  $f$  increases (i.e., for decreasing  $p$ ), as expected [65]. Typically the  $IDE$  of the SSPDs (slope of the dashed line) with parallel polarization is higher than that of SSPDs with perpendicular polarization. This can be explained by the different  $A(x)$  for the two polarizations as shown in the inset of Fig. 4.3. As an example, for structure of  $w = 100$  nm and  $p = 300$  nm, the

$A(x)$  in parallel polarization is spatially uniform and higher than the calculated  $A(x)$  for perpendicular polarization.

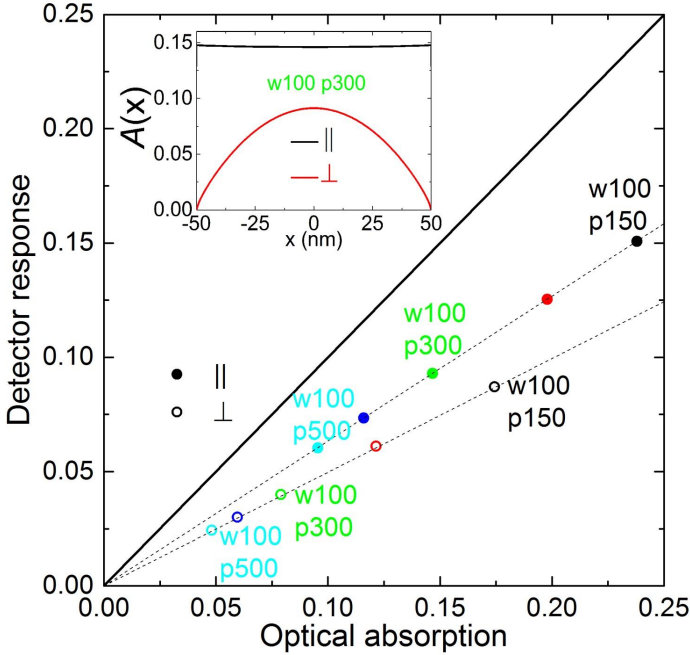


Figure 4.3: Calculated detector response as a function of optical absorption of meandering SSPDs with constant wire width ( $w = 100$  nm). The closed and open symbols represent parallel ( $\parallel$ ) and perpendicular ( $\perp$ ) polarization, respectively. The numbers next to the data points refer to the constant width  $w$  and varying pitch  $p$  expressed in nm. The inset shows a typical absorption distribution across the wire for structure with  $w = 100$  nm and  $p = 300$  nm. The diagonal line with slope of 1 represents  $IDE$  with a value of 1.

#### 4.4.2 Detector response for SSPDs with constant fill factors

Figure 4.4 shows the calculated response of meandering SSPDs with constant fill factors as a function of the average absorption for both polarizations. The solid and open symbols represent polarization states with the  $E$ -field parallel and perpendicular to the wire, respectively. For comparison, the triangles and squares represent structures with fill factor of  $f = 1/2$  and  $f = 2/3$ . The wire width  $w$  is set from 50 nm to 150 nm with a step of 10 nm, except for the structures with  $f = 1/2$  in perpendicular illumination, where extra settings of  $w$  of 5 nm, 10 nm, 20 nm, 30 nm, 40 nm, 50 nm are considered (open triangles) as well.

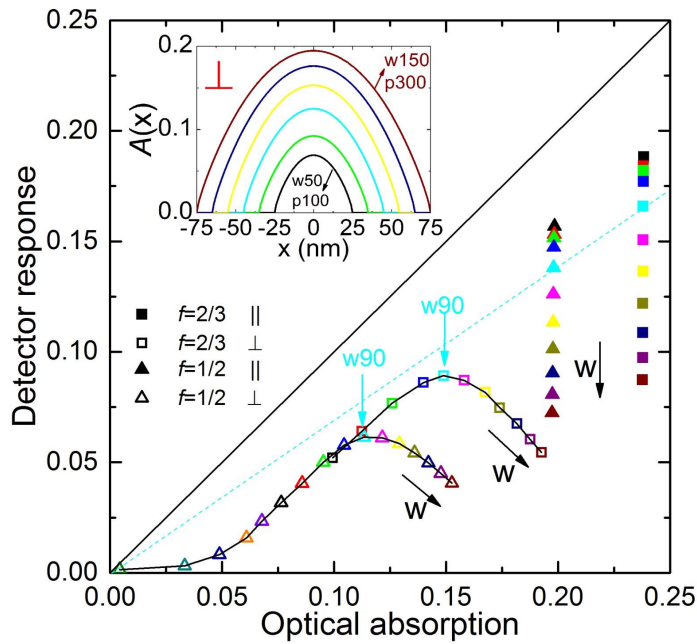


Figure 4.4: Calculated detector response as a function of optical absorption of SSPD meandering structures with varying wire width and constant fill factor of 1/2 (triangles) and 2/3 (squares). The closed and open symbols refer to parallel ( $\parallel$ ) and perpendicular ( $\perp$ ) polarized light, respectively. The arrow indicates increasing width of the wire. The inset shows the absorption distribution for perpendicular polarized light as a function of wire width (fill factor 1/2). The diagonal line with slope of 1 represents *IDE* with a value of 1.

For parallel polarization (solid symbols), the absorption distribution across the wire is almost uniform and the average absorption  $\bar{A}$  is mainly determined by the constant value of  $f$ ; the data points lie on a vertical line in the figure. The difference between the points is caused by a change in the internal detection efficiency as a function of wire width  $w$ . When comparing the two different fill factors, the structures with a constant wire width  $w$  (e.g.,  $w = 90$  nm in light blue) lie on a straight line through the origin (see the dashed line) as shown in Fig. 4.3, which represents a constant internal detection efficiency of the wire.

The data for perpendicularly polarized light for a constant fill fraction  $f$  and increasing  $w$  (direction of the arrow in Fig. 4.4) show a maximum in response  $R$  for a wire width around  $w = 90$  nm, for both values of the fill factor. The internal detection efficiency  $IDE$  increases sharply with wire width for very narrow wire and decreases with the width as  $w$  increases beyond  $w = 90$  nm. This behavior originates from the dependence of the  $LDE(x)$  as a function of wire width in combination with the non-uniform absorption distribution for perpendicularly polarized light. To obtain the  $LDE(x)$  for wires that are narrower than 150 nm we use the result of Fig. 4.2(a) for a 150 nm wide nanowire and omit the central part of the curve, leaving only the highly efficient edges of the wire. This procedure is motivated by numerical calculations of the  $LDE(x)$  [25] that show that removing the central part of the curve of a wide wire correctly predicts the behavior of narrower wires.

Experiments show a linear exchange between input photon energy  $E$  and bias current:  $I_b = I_o - \gamma E$ , where  $\gamma$  represents the interchange ratio between bias current and photon energy and  $I_o$  is a reference current beyond which the vortices enter the nanowire [30, 38]. In the photon detection model, a microscopic relation between  $I_{th}(x)$  and photon energy is assumed as  $I_{th}(x) = I_c - \gamma'(x) * E$ , where  $\gamma'(x)$  is the position-dependent interchange ratio between threshold current and photon energy. We note that the calculated average  $\overline{\gamma'(x)}$  from the model does not agree with the value of  $\gamma$  reported for three SSPDs with different widths [30]. The origin of this discrepancy is currently unclear, but may be caused by statistical fluctuations given the limited amount of experimental data. Making  $\gamma'(x)$  consistent with the measured  $\gamma$  leads to a change in the response shifting the curves in Fig. 4.4 up, leaving the optimum wire width unaffected to first order.

Because the edge has a higher detection efficiency than the center, the narrower wire has a higher average  $LDE(x)$  and a higher  $IDE$  and thus  $R$  for parallel polarization. With perpendicular illumination the absorption distribution as a function of wire width is an important factor. As the wire width rises, the average of  $LDE(x)$  decreases, but is compensated by an increase of the average absorption  $\bar{A}$ , as shown in the inset of Fig. 4.4. Because the  $LDE(x)$  is approximately constant for the first  $\sim 30$  nm from the edges and the average absorption increases with the wire width, the response of the de-

tector increases as a function of wire width until  $w \sim 60$  nm. For a wire width beyond  $\sim 60$  nm, there is a trade-off for the wire to be narrow enough to have a high  $LDE(x)$  and to be wide enough to have high optical absorption  $A(x)$ . This trade-off depends on the detailed shape of the absorption, the bias current relative to the threshold current and the wavelength of the light used. For the parameters considered in this chapter the trade-off results in an optimal value of  $w \approx 90$  nm, almost three times the width of the side-wing in the  $LDE(x)$  profile.

#### 4.4.3 Comparison between calculation and experiment

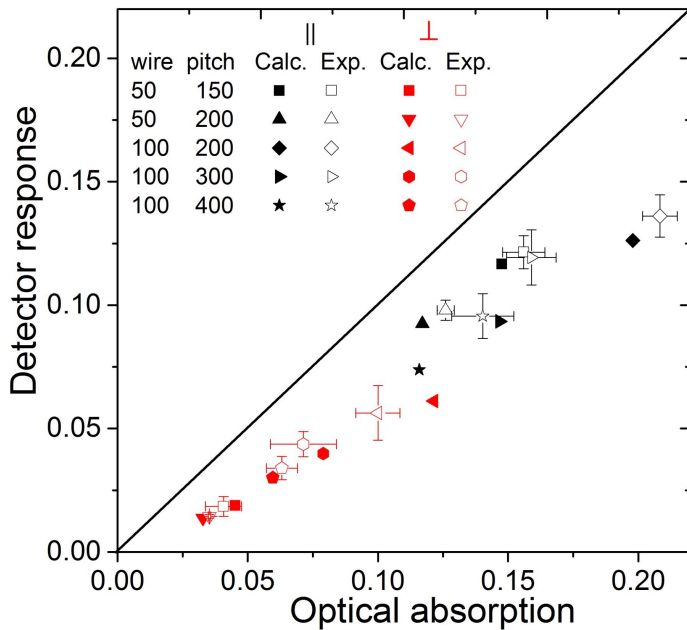


Figure 4.5: Measurements [42] and calculations of detector response as a function of optical absorption of meandering SSPDs. The open symbols represent experimental data as presented in Ref. [42]. The closed symbols refer to the calculated response based on the local detection efficiency  $LDE(x)$  for  $I_b = 0.9I_C$ . Black and red symbols represent parallel ( $\parallel$ ) and perpendicular ( $\perp$ ) polarization, respectively. Different symbol shapes refer to different structures (wire and pitch width) of the detector. The error bars on the experimental data represent the spread in properties between detectors of the same design. The diagonal line with slope of 1 represents  $IDE$  with a value of 1.

In order to verify our photon-detection model and optical absorption simulation, we calculate and compare the detector response for the structures used

in the experiment of Ref. [42]. Figure 4.5 shows the comparison of our calculation (solid symbols) with the experimental data (open symbols). Symbols in black and red represent parallel and perpendicular polarization, respectively. Good agreement between calculation and experiment is shown. The calculation confirms the hypothesis in Ref. [42] that the data with parallel polarization has a larger  $IDE$  (slope) than those for perpendicular polarization. We stress that the layout of the data points for calculation and experiment are strongly correlated, e.g., the rhombuses for calculations and measurements for a structure of  $w = 100$  nm and  $p = 200$  nm are located in the top right corner of data cluster for both polarizations. The use of the local detection efficiency  $LDE(x)$  that is supported by a microscopic detection model of photon-assisted vortex entry explains why the  $IDE$  depends on the detector geometry. The experimentally determined  $LDE(x)$  gives a quantitative description of the effect.

To obtain a non-unity  $IDE$ , we must assume that the highly efficient detectors reported in Ref. [42] were not biased to the depairing current of NbN. This assumption is quite reasonable because it is well known that the presence of inhomogeneities and current crowding in the bends of a wire can cause a reduction of the device critical current relative to the maximum possible depairing current. Such effects are expected to be much more prominent in long meandering wires as compared to a nanodetector. Current crowding in bends can reduce the critical current by as much as 40%, with typical values of 10–20% [26]. To get good agreement between experimental data and the calculation we have assumed  $I_b = 0.9 I_c$  for all devices to produce Fig. 4.5. This demonstrates that our calculations quantitatively describe the SSPDs which are used for applications, at the typical currents at which they are operated.

The agreement between calculation based on the detection model and the experimental data justifies the procedure to obtain the  $LDE(x)$  for wire widths smaller than 150 nm.

## 4.5 Conclusions

We have calculated the optical absorption and  $E$ -field distribution of meandering SSPDs via FDTD simulation. The absorption distribution is uniform across the nanowire when illuminated with  $E$ -field parallel to the wire. For perpendicularly polarized light the absorption close to the edges is minimal while the center of the wire displays maximum absorption. The response of an SSPD can be calculated by taking into account a local detection efficiency obtained from experiment and the absorption distribution. We have used this procedure to calculate the detector response for meandering SSPDs with different pitch and wire widths. For SSPDs with a constant wire width, the internal detection efficiency is predominately determined by the wire width, and higher fill

factor leads to higher detector response. For SSPDs with a constant fill factor, the detector response curve for perpendicular polarization shows an optimal design for  $w = 90$  nm that represents a trade-off between the wire being wide enough to efficiently absorb the incoming light while still being narrow enough to have a high local detection efficiency. To validate our calculations and the use of the experimentally determined local detection efficiency from Renema et al. (Ref. [35]) we compare the predictions with experimentally observed values from Anant et al. (Ref. [42]). The good quantitative agreement confirms that the local detection efficiency obtained for a nanodetector can be used to make quantitative predictions for state-of-the-art meandering wire detectors. More importantly, it shows how the idea of a photon-assisted vortex-entry model that results in a position-dependent local detection efficiency quantitatively explains a polarization-dependent internal detection efficiency.



## Chapter 5

# An Absorption-Based Superconducting Nanodetector as a Near-Field Optical Probe

We investigate the use of a superconducting nanodetector as a novel near-field probe. In contrast to conventional scanning near-field optical microscopes, the nanodetector absorbs and detects photons in the near field. We show that this absorption-based probe has a higher collection efficiency and investigate the details of the interaction between the nanodetector and the dipole emitter. To this end, we introduce a multipole model to describe the interaction. Calculations of the local density of states show that the nanodetector does not strongly modify the emission rate of a dipole, especially when compared to traditional metal probes<sup>1</sup>.

### 5.1 Introduction

Near-field optical microscopes have been used to probe the fluorescence of a single molecule and the evanescent near field of a large variety of nanophotonic structures [80,81]. Because near-field probes interact with evanescent waves the resolution of these microscopes is not limited by the diffraction limit that holds for propagating waves. Conventional near-field microscopes probe the optical

---

<sup>1</sup>Q. Wang, and M. J. A. de Dood, *Opt. Express* **21**, 3682, (2013).

near field with a metal tip [82], a metal particle [83] or a metal coated tip with a subwavelength hole [84]. These probes are positioned in the near field and scanned in the lateral directions. These tips either scatter the light directly into the optical far field, or through a subwavelength aperture connected to an optical fiber where it is detected by a photosensitive detector in the far field.

To attain subwavelength lateral resolution, the size of the aperture or tip should be smaller than the wavelength. This makes near-field probes based on scattering inherently inefficient because light scattering from subwavelength metal particles is an inefficient process. For particles that are much smaller than the wavelength, Rayleigh scattering occurs and the scattering decreases as  $a^6/\lambda^4$ , where  $a$  is the dimension of the particle and  $\lambda$  is the wavelength. This low collection efficiency makes near-field studies of quantum optics an extremely challenging task, because detection of weak light with a small collection efficiency (i.e., missing out many photons) introduces noise [46]. Similarly in experiments on single molecules the total number of photons emitted by a molecule is given by the ratio  $\tau_{\frac{1}{2}}/\tau_{rad}$ , where  $\tau_{\frac{1}{2}}$  is the half life of a molecule due to bleaching, and  $\tau_{rad}$  is the radiative lifetime [85].

Since the absorption of a small particle scales with its volume, i.e., as  $a^3$ , an intrinsically much more efficient near-field nanodetector can be constructed. Recently, superconducting nanodetectors have been demonstrated that absorb a single photon and create a measurable electronic pulse for each absorbed photon [14].

In this chapter we consider a detector made of a 4 nm thick NbN film grown on a GaAs substrate, i.e., identical to the square nanodetector reported in Ref. [64]. Photons can be detected only in the constricted area where the current through the detector is close to the critical current of the superconductor at cryogenic temperatures.

## 5.2 Scattering and absorption by a near-field probe

Conventional scanning near field optical microscopes (SNOMs) can be subdivided into two major types: aperture based SNOMs and scattering type SNOMs [86]. The aperture based SNOMs make use of a subwavelength hole in a metal film or metal-clad fiber tip [87–91]. The transmission through a subwavelength hole in a good conductor is extremely low and is proportional to  $a^6/\lambda^4$  ( $a/\lambda \ll 1$ ) [92], where  $a$  is the radius of the aperture, and  $\lambda$  is the wavelength of light. Similarly, the scattering type SNOMs make use of light scattering of the sharp end of a metal clad tip to scatter the optical near field directly onto a far-field detector. To estimate the performance of this type of SNOMs the probe is considered to be a sphere [93], and the tip's scattering cross section is then given by Mie theory. As shown in the schematic in

Fig. 5.1, a subwavelength sphere that models the scanning probe, is located above a substrate and is excited at normal incidence light. In this geometry, the tip induces a surface charge in the substrate that can be described by an image dipole at a distance  $r$  from the surface [94]. For the sphere one can apply the Rayleigh limit ( $a/\lambda \ll 1$ ) to calculate the scattering cross section  $\sigma = 8\pi|\alpha^{eff}|^2/(3\lambda^4)$  [95], where

$$\alpha_{\parallel}^{eff} = \alpha(1 - \beta)/(1 - \frac{\alpha\beta}{32\pi r^3}) \quad \text{or} \quad \alpha_{\perp}^{eff} = \alpha(1 + \beta)/(1 - \frac{\alpha\beta}{16\pi r^3}), \quad (5.1)$$

which represents the effective polarizability of the sphere close to the surface of the substrate. The applied electric field is either parallel or perpendicular to the surface. In Eq. (5.1) the polarizability of a sphere  $\alpha = 4\pi a^3(\epsilon_{sp} - 1)/(\epsilon_{sp} + 2)$ ,  $\beta = (\epsilon_{sb} - 1)/(\epsilon_{sb} + 1)$ , where  $\epsilon_{sp}$  and  $\epsilon_{sb}$  are the complex dielectric constants of the spherical particle and the substrate, and  $a$  is the radius of the particle [94,95].

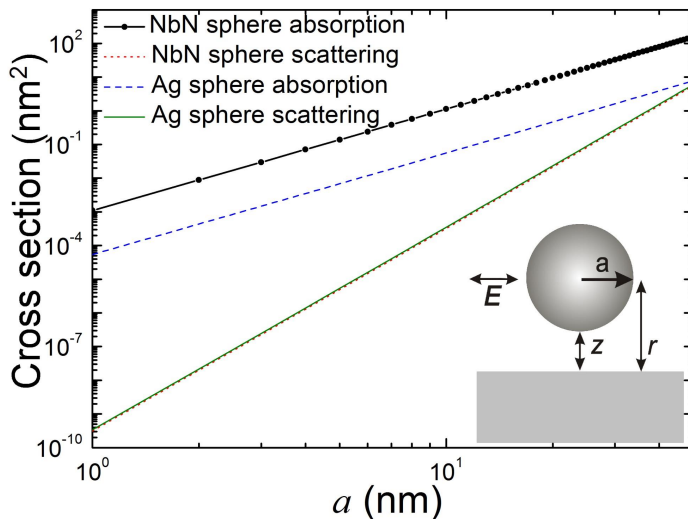


Figure 5.1: Absorption cross section for a NbN sphere close to a GaAs substrate, as compared to a Ag sphere. Calculations are done at  $\lambda = 1000$  nm, as a function of sphere radius. The inset shows a sphere with a radius of  $a$  at distance  $z_0 = 10$  nm from the semi-infinite substrate. The particle is excited by an external electric field  $E$  parallel to the interface. In the Rayleigh limit ( $a/\lambda \ll 1$ ), the absorption cross section is much larger than the scattering cross section (Scattering curves for Ag and NbN are overlapped). Because of the larger imaginary part of the dielectric constant of NbN, the absorption cross section of a NbN sphere is approximately 10 times larger than that of a Ag sphere.

Figure 5.1 compares the calculated scattering and absorption cross section for a Ag and a NbN sphere close to a GaAs substrate (refractive index 3.5).

Calculations are shown for light with polarization parallel to the substrate surface with a wavelength of 1000 nm, as a function of the radius  $a$  of the sphere. The air gap between the sphere and the substrate is kept constant at  $z_0 = 10$  nm as the radius of the sphere is varied. In these calculations we assume a dielectric constant of  $\epsilon_{sp} = -45.6 + 2.9i$  for the Ag sphere [96] and  $\epsilon_{sp} = -8.2 + 31.4i$  for NbN [47].

As can be seen in Fig. 5.1, the scattering cross sections of a NbN and a Ag sphere are comparable in the Rayleigh limit. This reflects the fact that both materials provide a large dielectric constant  $|\epsilon|$  and scattering depends on the absolute value of the polarizability. The absorption cross section of a sphere much smaller than the wavelength is proportional to the volume of the particle, and exceeds the scattering cross section by several orders of magnitude. The absorption cross section of a NbN sphere exceeds the absorption cross section of a comparable Ag sphere by more than an order of magnitude for all sizes. For a realistic, 20 nm diameter tip, the absorption of a NbN sphere is 4 orders of magnitude larger than the scattering of either a NbN or a Ag sphere. Additional calculations (not shown) for vertical polarization and for Au or Al metal are very similar to those presented in Fig. 5.1. A SNOM, based on a NbN nanodetector, that would be able to absorb and detect the radiation directly in the optical near field, would thus comprise a great advantage over current SNOM technology.

A real detector that can operate in the optical near field could be based on a thin strip of NbN material that is tapered down to a constriction which forms the active area [64]. Figure 5.2 compares the absorption cross section of a square detector of size  $a \times a$  with the absorption of a NbN sphere of radius  $a$ . A schematic drawing of the NbN nanodetector is shown in the inset of Fig. 5.2. The absorption of the NbN sphere is calculated using the Rayleigh approximation for small particles, while the results of a square on a substrate, excluding the wire, are based on finite-difference-time-domain (FDTD, Full-Wave package, RSoft [71]) simulations. The FDTD calculation includes a 3D model of the square NbN detector on a semi-infinite GaAs substrate. The detector is illuminated at normal incidence by a plane wave with the electric field parallel to the GaAs substrate surface. We monitor the power absorption in the detector and the total intensity of the illumination. From this we calculate the absorption cross section of the square detector. As can be seen from the figure, the absorption of the square NbN detector is larger than that of the sphere, even though the geometrical cross section of the sphere ( $\pi a^2$ ) is larger than that of the detector ( $a^2$ ).

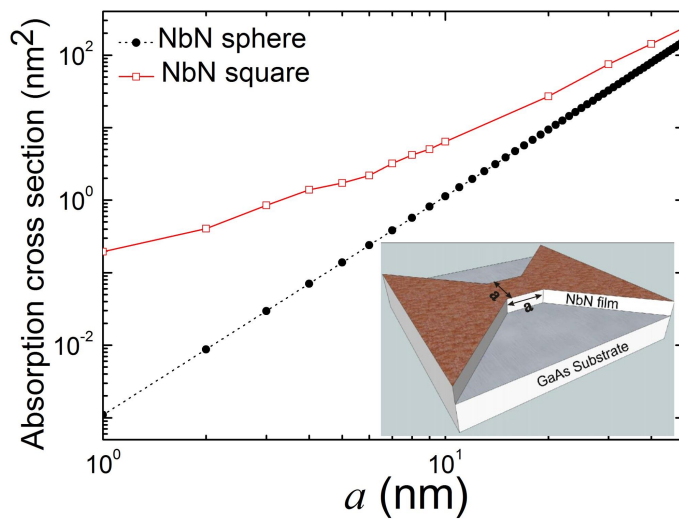


Figure 5.2: Comparison of the absorption cross section for a square and spherical NbN nanodetector as a function of size  $a$  at  $\lambda = 1000$  nm. Simulations are used to calculate the absorption of a square detector at  $\lambda = 1000$  nm. In the optical near field ( $a/\lambda \ll 1$ ), the absorption cross section of a NbN square is larger than that of a sphere. The inset shows a schematic picture of a realistic NbN nanodetector: a 4 nm thick NbN film is grown on a GaAs substrate. A bowtie shape with a nanoscale square constriction serving as the detector active area is patterned in the film.

### 5.3 Interaction between a NbN detector and a dipole emitter

To evaluate the performance of a SNOM using FDTD we perform simulation of a scanning probe with a light source in the near field. To this end we place a dipole emitter on a GaAs substrate to mimic the single-photon emission from an atom or a quantum dot. Figure 5.3 shows the geometry and the 3D coordinate system used in these simulations. On the surface of a semi-infinite GaAs substrate ( $z \leq 0$ ), a point dipole source is placed at the origin, with its dipole moment along the  $x$ -direction, i.e., in the plane of the surface. The square block of NbN represents the nanodetector ( $50 \text{ nm} \times 50 \text{ nm} \times 4 \text{ nm}$  constriction), and is situated above the dipole source. Both the detector and the emitter are centered on the  $z$ -axis.

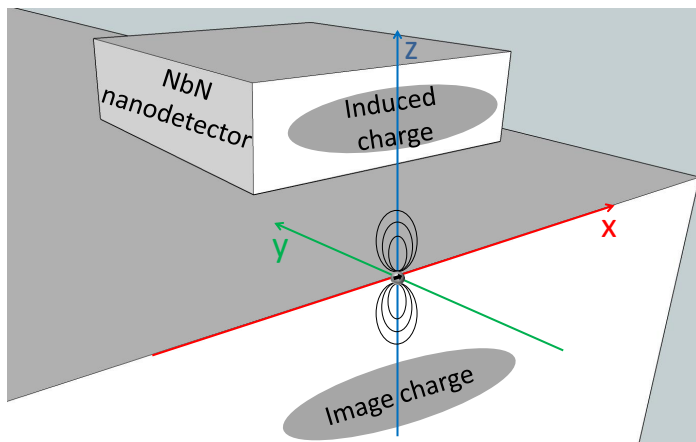


Figure 5.3: Physical model used in FDTD simulations of detector sensitivity and resolution. The NbN nanodetector is located above a dipole emitter (point source) with a dipole moment along  $x$ -direction. The emitter ( $\lambda = 1000 \text{ nm}$ ) is placed on the semi-infinite GaAs substrate. Charge areas are induced inside the nanodetector and in the substrate underneath the emitter.

Several dipole-based models have been put forward to describe the interaction between the tip of the probe in SNOM and the sample [94, 97, 98]. For a scattering SNOM as described in Ref. [94], an analytical dipole model can describe the interaction between the probe tip and a point sample. Within these models, the probe tip is treated as a polarizable sphere that interacts with a dipole source on a substrate.

In our case, when the distance between the nanodetector (probe) and the dipole (sample on substrate) becomes much smaller than the wavelength, a charge area is induced inside the nanodetector by the electric field of the dipole, and the electric potential generated by this charge area can be expressed by a

multipole expansion [79]:

$$\varphi(\vec{R}) = \frac{1}{4\pi\epsilon_o} \left[ \frac{Q}{R} - \vec{p} \cdot \nabla \frac{1}{R} + \frac{1}{6} \overset{\leftrightarrow}{D} : \nabla \nabla \frac{1}{R} + \dots \right], \quad (5.2)$$

where  $\varphi(\vec{R})$  is the potential at the position  $\vec{R}$  ( $R = \sqrt{x^2 + y^2 + (z - z_0)^2}$ ),  $z_0$  is the distance from the dipole source to the detector,  $\epsilon_o$  is dielectric constant in vacuum,  $Q$  is total induced charge, vector  $\vec{p}$  is the dipole moment, and the tensor  $\overset{\leftrightarrow}{D}$  relates to the quadrupole contribution to the field.

The first term in the brackets of Eq. (5.2) reflects the electric potential generated by the total amount of induced charge  $Q$  in the detector. In the detector the amounts of positive and negative induced charge should be equal and this term vanishes.

Within the dipole approximation we only keep the second term in Eq. (5.2), i.e., the dipole moment, and neglect all higher order terms in the multipole expansion. In this chapter, we however, do include the electric field of the induced dipole in the probe (nanodetector) that induces surface charges in the GaAs substrate. This contribution is equivalent to an image dipole in the substrate underneath the dipole source at a distance of  $2z_0$  from the probe [94].

The image dipole has a dipole moment  $p' = -\beta p$ , where  $\beta = (\epsilon_{sb} - 1)/(\epsilon_{sb} + 1)$  [94,99], and  $\epsilon_{sb} = 12.25$  is the dielectric constant of the GaAs substrate ( $\lambda = 1000$  nm). The total field includes the original dipole field and the contribution from the image dipole fields. The effective polarizability for the probe-sample system (parallel to the substrate) is then given by Eq. (5.1).

With this effective polarizability, the scattering and absorption cross section are calculated in a straightforward way.

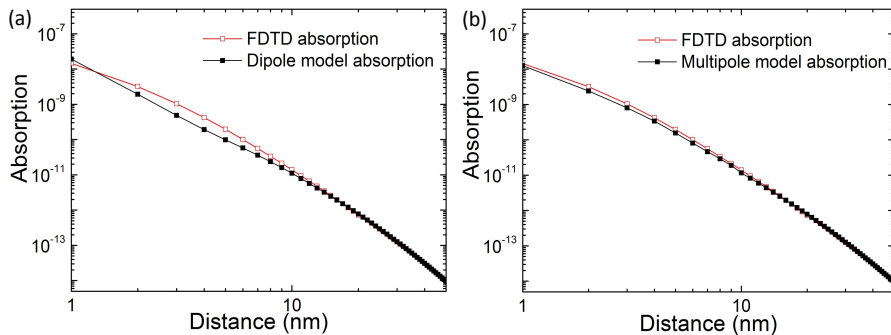


Figure 5.4: Calculated absorption of a point dipole as a function of distance between the nanodetector and the substrate. Calculations are done for a wavelength  $\lambda = 1000$  nm with the radiation power of the dipole source fixed at 1 W. The FDTD results are compared with two models: a dipole (a) and a multipole (b) model.

Figure 5.4 shows the absorption in the detector as a function of the distance

between the detector and the dipole. Calculations based on the dipole approximation and complete FDTD are compared. As can be seen in Fig. 5.4(a), a noticeable deviation exists between the absorption calculated by the dipole model and by FDTD for  $z < 10$  nm. We explain this deviation by the square shape of the detector instead of a simple sphere for the SNOM tip. In a square detector a more complex image charge distribution exists. This charge distribution cannot be described by an induced dipole only. In order to describe the image charge more accurately, we include a quadrupole moment in the expression given by Eq. (5.2). Figure 5.4(b) shows the absorption in the detector using a multipole expansion (i.e., dipole and quadrupole) and FDTD simulations. Compared to the dipole model above, the multipole model, that includes a quadrupole moment, fits the FDTD curve very well.

To analyze this contribution in a concise way we consider a dipole moment in the  $x$ -direction (see Fig. 5.3) that creates an induced dipole in the nanodetector, which is mirrored and points in the  $-x$ -direction. For the dipole and its induced dipole oriented along the  $x$  direction the  $E_y$  component of the field in the  $xz$ -plane is zero and the electric field is strongly concentrated at the center of the constriction. At this position the field contains only nonzero  $E_x$  and  $E_z$  components. Hence, we limit our model to the component  $D_{13}$  of the tensor  $\overleftrightarrow{D}$ . The induced quadrupole moment in the detector can then be defined as:

$$D_{13} = \int_V 3xz\rho(x, y, z)dxdydz = \zeta\sqrt{E_x^2 + E_y^2}, \quad (5.3)$$

where we have introduced a tuning parameter  $\zeta$  that we determine from the comparison of the model with FDTD simulations.

Again, an image charge is induced below the emitter as shown in Fig. 5.3, with  $p' = -\beta p$  and  $D' = \beta D$  [99], where  $\beta = (\varepsilon_{sb} - 1)/(\varepsilon_{sb} + 1)$ .

The total electric field  $\vec{E}(E_x, E_y, E_z)$  inside the nanodetector contains a contribution from the dipole emitter and the image charge and can be expressed as:

$$\vec{E} = \vec{E}_{emitter} + \vec{E}_{image}, \quad (5.4)$$

which can be solved analytically. To obtain the absorption in the detector we numerically integrate  $|\vec{E}|^2$  over the volume of the nanodetector and multiply the result by the imaginary part of the dielectric constant [79]. We neglect phase variations of the electric field in our model, because the near field of a radiant dipole can be treated as a static electric dipole field as long as  $kr \ll 1$  ( $k$  is the wave vector and  $r$  is the distance from the dipole) [79].

At distances larger than 20 nm the interaction between the detector and the dipole emitter is very weak. In this case both the multipole model and FDTD calculations yield almost identical curves with the same tendency that

reflects the rapid decay of the electric field of the dipole source with distance. From the comparison of the multipole model and FDTD calculations we find a value  $\zeta = 14.5$  for the tuning parameter in Eq. (5.3). We note that a very small deviation remains in Fig. 5.4(b). We attribute this deviation to the fact that our multipole model does not include the finite size of the detector. In the multipole model we ignore the boundaries of the detector based on the assumption that the quadrupole field decays very strongly towards the edge of the detector.

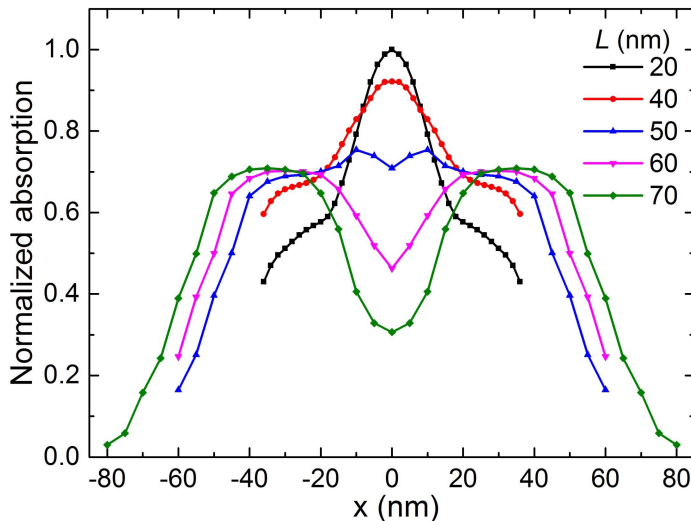


Figure 5.5: The absorption of a  $50 \times 50 \text{ nm}^2$  detector when scanning over two dipole sources separated by a distance  $L$ . The different curves correspond to different values of  $L$ . The two dipoles can be resolved for a separation  $L = 60 \text{ nm}$ . The absorption curves are normalized to the maximum for a separation  $L = 20 \text{ nm}$ .

For practical applications of the novel, absorption-based, SNOM tip it is important to consider the spatial resolution. To this end, we perform additional FDTD calculations. To estimate the resolution we investigate the response of the detector to two dipole sources separated by a distance  $L$ . Figure 5.5 shows the absorption of the detector when scanning the two sources on the substrate surface. The absorption values are normalized to the maximum of the absorption for a separation  $L = 20 \text{ nm}$ . The various curves in the figure correspond to different values of the separation  $L$ . As can be seen in the figure, two sources at a distance  $L = 60 \text{ nm}$  can be resolved, comparable to the transverse size of the detector. The calculations are performed with the detector at a height  $z_0 = 10 \text{ nm}$  from substrate. We chose this height to find a compromise between the near-field probe affecting the dipole emitter and a degradation of the resolution that occurs for larger distances of the detector

from the substrate. The most favorable situation is reached for a detector that is as far away as possible, without significantly degrading the resolution. In principle, the spatial resolution can be improved via nanofabrication of smaller detectors by reducing the constriction area of the wire further. However, it is currently unclear how this affects the operation of the detector and what the practical limitations on the active area of the detector are when the resistive region (“hot spot”) in the detector is taken into account [64]. The 50 nm constriction considered in this work has been studied experimentally [64] and a spatial resolution of  $\sim 500$  nm has been demonstrated.

## 5.4 The detector’s influence on the dipole source/emitter

In the previous sections, we have discussed the absorption of radiation from an emitter by a nanoscale detector. In this section we will investigate and discuss the influence of the detector on the emitter. It is well-known that near-field probes affect the emitter and can change the decay rate and quantum efficiency of the emitter [100–102]. The change in decay rate is proportional to the local density of states (LDOS) of the system consisting of the near-field probe and the substrate on which the emitter is placed.

In order to estimate the change in emission rate we calculate the LDOS for a simple system consisting of a thin (4 nm thick) NbN film on a semi-infinite GaAs substrate. We are primarily interested in the near-field interaction where the distance between the emitter and the detector is comparable or smaller than the lateral size of the detector. In this near-field regime the change in the decay rate of an emitter close to the detector is expected to be very similar to the change in decay rate induced by an infinite large slab. For the slab configuration, the LDOS can be calculated with relative ease using an analytical expression of the Green’s function.

The LDOS  $\rho(\vec{R}, \omega)$  can be calculated by taking the imaginary part of the trace of the Green’s dyadic  $\overset{\leftrightarrow}{G}(\vec{R}, \vec{R}', \omega)$  of the system [103]. This quantity is evaluated at the position  $\vec{R} = \vec{R}'$ , where  $\vec{R}'$  is the location of the emitter with transition frequency  $\omega$ :

$$\rho_{LDOS}(\vec{R}, \omega) = \frac{\omega}{\pi c^2} \text{Im}\{\text{Tr}[\overset{\leftrightarrow}{G}(\vec{R}, \vec{R}, \omega)]\}. \quad (5.5)$$

We use the Green’s dyadic  $\overset{\leftrightarrow}{G}(\vec{R}, \vec{R}, \omega)$  given by the approach of Ref. [100] that separates the dyadic into a nonscattering part  $\overset{\leftrightarrow}{G}_o(\vec{R}, \vec{R}, \omega)$  and a scattering part  $\overset{\leftrightarrow}{G}_S(\vec{R}, \vec{R}, \omega)$ . The detailed expressions for these quantities can be found in Ref. [102]. For a planar interface with an emitter at a distance

$z$  from the interface the Green's dyadic at the position of the emitter can be significantly simplified. In cylindrical coordinates we obtain:

$$\begin{aligned} \vec{G}(z, z, \omega) = \frac{i}{4\pi} \int_0^\infty d\lambda [(c'_1 e^{i2h_1 z} + 1) \frac{\lambda}{2h_1} \hat{e}_r \hat{e}_r + (\lambda - f'_1 e^{i2h_1 z}) \frac{h_1}{2k_1^2} \hat{e}_\phi \hat{e}_\phi \\ + (f'_1 e^{i2h_1 z} + 1) \frac{\lambda^3}{k_1^2 h_1} \hat{e}_z \hat{e}_z], \end{aligned} \quad (5.6)$$

where  $c'_1 = (h_1 R_1 - h_2)/(h_1 R_1 + h_2)$ ,  $f'_1 = (S_1 h_1 \varepsilon_2 - h_2 \varepsilon_1)/(S_1 h_1 \varepsilon_2 + h_2 \varepsilon_1)$ , with  $R_1$  and  $S_1$  defined as  $R_1 = (h_2 - i h_3 \tan \theta)/(h_3 - i h_2 \tan \theta)$ , and  $S_1 = (h_2 \varepsilon_3 - i h_3 \varepsilon_2 \tan \theta)/(h_3 \varepsilon_2 - i h_2 \varepsilon_3 \tan \theta)$ . In these expressions,  $k_j$  denotes the wave vector in  $j$ -th layer,  $h_j$  is the vertical component of the wave vector and the phase change in the second (middle) layer is  $\theta$ . These quantities are given by  $k_j^2 = \varepsilon_j (\omega/c)^2$ ,  $h_j^2 = k_j^2 - \lambda^2$  and  $\theta = h_2 d_2$  respectively, in which  $c$  is the speed of light in vacuum, and  $\varepsilon_j$  is the dielectric constant of  $j$ -th layer, and  $d_2$  is the thickness of the second layer [102].

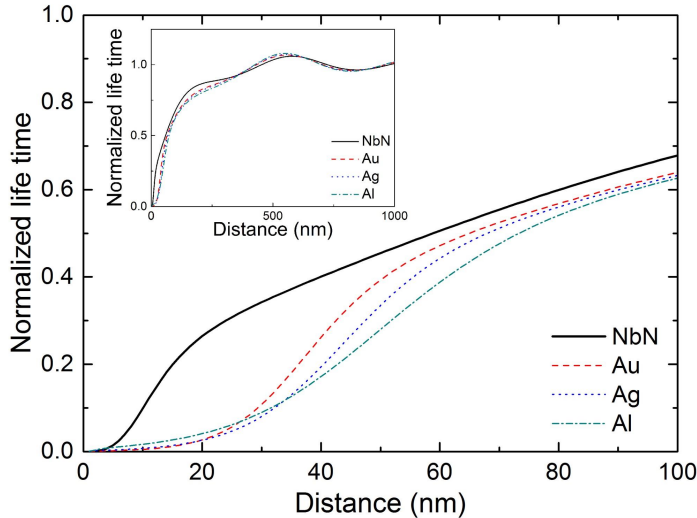


Figure 5.6: Normalized life time of an emitter close to a 4 nm thick metal film as a function of distance from the substrate. Calculation are shown for a NbN, Au, Ag and Al film at  $\lambda = 1000$  nm. In the near field (distance  $< 50$  nm), the emitter close to NbN behaves differently from those close to the other three metal films. The inset shows the variations in emitter lifetime for larger distances.

Figure 5.6 compares the normalized life time of an emitter calculated as a function of distance for an emitter close to a 4 nm thick NbN, Au, Ag or Al film. Calculations are shown for a wavelength of 1000 nm. The normalized lifetime is obtained by dividing spontaneous decay rate in free space by the

spontaneous decay rate of the dipole emitter as obtained from the Green's function:

$$\Gamma(z) \propto \omega^2 \text{Im}\{\text{Tr}[G(z, z, \omega)]\}. \quad (5.7)$$

The proportionality constant is divided out by normalization to the life time of the dipole in free space.

The curves in Fig. 5.6 show that the lifetime of the emitter close to the NbN film is much higher for distances below 50 nm compared to the lifetime close to a thin metal film of Au, Ag or Al. This makes a NbN detector a very interesting near-field probe because it has a relatively high detection efficiency while leaving the emission rate of the dipole unaffected. We attribute the relatively weak coupling of the NbN detector to the strong damping in the material that excludes strong energy transfer to the film via surface plasmons. We emphasize that all thin films have comparable reflectivity while only Au, Ag and Al support low-loss surface plasmon modes. This inset shows the calculated normalized life time for distances up to 1000 nm. For larger distances all curves show characteristic oscillations with a periodicity of  $\lambda/4$  for an emitter close to a mirror [100]. The modulation of the oscillation around a normalized lifetime of 1.0 is a consequence of self interference between the emitted radiation and radiation reflected by the mirror. These similar oscillations for the different materials are a signature of the fact that reflectivity of the different thin films is comparable.

To further investigate the role of surface plasmons in the near-field interaction for a dipole close to a thin film we calculated the LDOS as a function of angular frequency for different materials. Figure 5.7 shows the calculated LDOS for a 4 nm thick NbN film compared to a 4 nm thick Ag film as a function of frequency. Calculations are shown for a dipole at a constant distance of 5 nm and 10 nm from the metal surface. As can be seen, the calculations for the Ag film show a sharply double peaked structure at angular frequencies close to  $3 \times 10^{15}$  and  $7 \times 10^{15}$  rad/s, while the calculations for NbN show a relatively small maximum around a frequency of  $7 \times 10^{15}$  rad/s.

To calculate these data we use two different modified Drude models [96,104] to describe the dielectric constant of NbN and Ag as a function of frequency:

$$\varepsilon_{NbN}(\omega) = \varepsilon_{NbN-high} - \frac{\varepsilon_{NbN-high} \omega_{NbN-p}^2}{\omega^2 + i\gamma_{NbN}\omega}, \quad (5.8)$$

$$\varepsilon_{Ag}(\omega) = \varepsilon_{Ag-high} - \frac{(\varepsilon_{Ag-static} - \varepsilon_{Ag-high}) \omega_{Ag-p}^2}{\omega^2 + i\gamma_{Ag}\omega}, \quad (5.9)$$

where  $\omega_{NbN-p} = 5.28 \times 10^{15}$  rad/s and  $\omega_{Ag-p} = 1.72 \times 10^{16}$  rad/s are plasma frequencies;  $\gamma_{NbN} = 3.77 \times 10^{15}$  rad/s and  $\gamma_{Ag} = 2.3 \times 10^{13}$  rad/s are the damping constants of the plasma excitation;  $\varepsilon_{NbN-high} = 12.5$  and  $\varepsilon_{Ag-high} = 5.45$

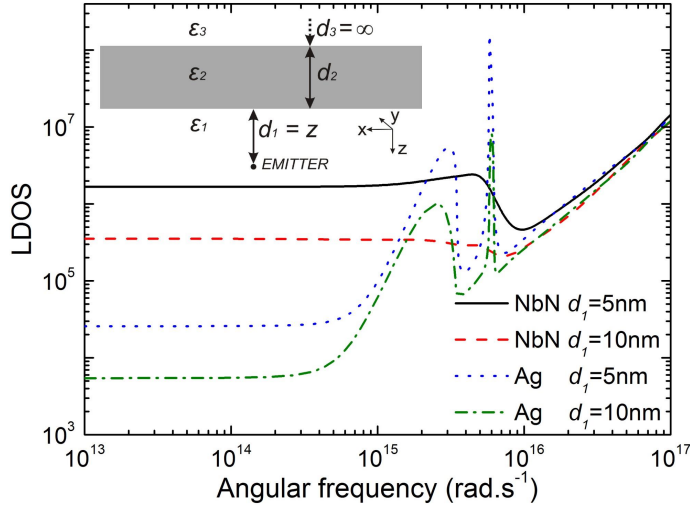


Figure 5.7: Local density of states (LDOS) at the position of the emitter as a function of frequency for different metal substrates. Results are shown for a 4 nm thick NbN film and a 4 nm thick Ag film on a semi-infinite GaAs substrate as shown in the inset. The distance between the emitter and the film is set to 5 nm or 10 nm, which are in the near field of the emitter leading to a strong coupling to surface plasmon modes for the case of a Ag film.

are the relative permittivity in the high frequency limit and  $\varepsilon_{Ag-static} = 6.18$  is the relative permittivity in the static limit for Ag.

The data in Fig. 5.7 show that for low angular frequencies below  $10^{15}$  rad/s (wavelength larger than 1800 nm), all curves of the LDOS are very smooth and nearly constant. For frequencies above  $10^{16}$  rad/s (wavelength shorter than 180 nm), all curves approach a LDOS that is proportional to  $\omega^2$ . In the relevant spectral range between angular frequencies of  $10^{15}$  and  $10^{16}$  rad/s (wavelength range from 180–1800 nm) the calculation for a NbN and a Ag film are markedly different.

The Ag system has two peaks due to the localized surface plasmons. Those sharp fluctuations in LDOS come from the strong energy coupling between the emitter and the Ag film, and this will enhance the energy transfer from the emitter to the Ag that reduces the lifetime of the emitter. These large fluctuations show that the surface plasmon has a profound effect on the emitter and the field that is emitted. In contrast, the LDOS for NbN film shows a much smoother frequency dependence and therefore perturbs the original field much weaker.

## 5.5 Conclusions

We have introduced a novel, absorption-based, near-field probe based on a NbN nanodetector that absorbs and detects single photons directly in the near field. This nanodetector has a higher detection efficiency compared to conventional scanning near-field optical microscopes because it is based on the physical process of absorption instead of scattering. We calculate an enhancement of 1 to 2 orders by comparing the absorption of a NbN detector with the scattering cross section of a Ag particle using Mie theory in the Rayleigh limit. We introduce a multipole model to describe the near-field interaction between a square NbN detector and a dipole emitter on a GaAs substrate and find that this analytical model fits well with FDTD simulations. From the calculations and FDTD simulations we find that a spatial resolution of  $\sim 60$  nm can be achieved for a detector ( $50 \text{ nm} \times 50 \text{ nm}$ ) at 10 nm distance from the substrate. This resolution is limited by the detector size and may be improved for smaller detectors. Further research on nanodetectors smaller than  $50 \text{ nm} \times 50 \text{ nm}$  is needed to find out whether the active area of the detector can be reduced further. A nanodetector close to an emitter also influences the decay rate of that emitter. For good metals with low-loss, large enhancements in the local field can be achieved if the emitter couples to a plasmon mode. For a near-field probe this strong perturbation of the emitter is undesired. We use a Green's function formalism to calculate and compare the change in decay rate for a NbN-nanodetector versus other, commonly used, metals in SNOM tips (Ag, Au and Al). We find that the life time of an emitter that emits at  $\lambda = 1000$  nm is only mildly decreased when the emitter is close to a NbN film, while a strong reduction in lifetime occurs for an emitter close to other metals. To explain this difference, we calculate the LDOS at the position of the emitter close to NbN and Ag film as a function of angular frequency of the emitter and show that the surface plasmon on the Ag film causes a strong energy transfer, reducing the life time of the emitter. In contrast, the NbN film has a much weaker coupling to the emitter and does not have a well-developed plasmon mode.

This novel nanodetector could be integrated with a cantilever or a tuning fork as a detection probe. To this end, the superconducting nanodetector should operate in a cryostat ( $\sim 4$  K) to create a near-field scanning optical microscope with high spatial resolution and single-photon and multiphoton sensitivity [64]. This opens new possibilities to explore single emitters, quantum light and optical antenna structures at the nanoscale.

## Chapter 6

# Near-Field Single-Photon Detection in a Scattering SNOM

A conical tip made out of good conductive metal can be used to efficiently localize the optical field at the apex of the tip. For a tip of finite length both a field singularity (lightning rod effect) and a surface plasmon resonance contribute to the electric field enhancement. A strongly absorbing superconducting nanodetector placed in the optical near field of the tip shows enhanced optical absorption. The design of an optimal tip-detector system is nontrivial because the strong damping by the detector shifts the resonance wavelength of the tip and significantly lowers the quality factor of the resonance. We compare calculations of the field enhancement of a bare tip to the absorption enhancement in the detector in the presence of the tip as a function of tip length, apex radius and semi-angle of the cone. The resonance of a 225 nm long gold tip in the presence of a nanodetector occurs at  $\sim 1000$  nm and is red-shifted by 150 nm compared to the resonance of a bare tip<sup>1</sup>.

---

<sup>1</sup>Q. Wang, and M. J. A. de Dood, proceeding 9504-2, SPIE Optics + Optoelectronics, Prague, Czech Republic, (2015).

## 6.1 Introduction

Direct detection of single photons in the optical near field would be beneficial to the investigation of light-matter interaction on the nanoscale. However, this involves two contradicting requirements: the detectors should have near-unity efficiency and they should be smaller than the wavelength of light. Nanometer-sized NbN superconducting single-photon detectors (SSPDs) [61] have been applied in quantum optics and communication due to its sensitivity to a wide wavelength range, low noise and a high detection efficiency [17]. Such detectors are prime candidates to be used as a sensor in near-field photon detection [32]. To study the absorption of the detector in the near field, we perform finite-difference-time-domain (FDTD, FullWave package, RSoft [71]) simulations to calculate the enhanced field and photon absorption of the detector in the vicinity of a tip of a scattering scanning near-field optical microscope (scattering SNOM).

We consider a long, 150 nm wide, 5 nm thick NbN wire fabricated on a GaAs substrate. The wire is constricted to a small, 150 nm  $\times$  100 nm weak point in the wire [38, 64]. When a current is applied to these nanodetectors the superconductivity is weakest at the constriction and absorption of single photons leads to detection events. By reducing the bias current more photons need to be absorbed at the same time to trigger the detector and the detector thus operates in a higher photon number regime [29, 36]. To increase the near-field absorption of a subwavelength detector an antenna structure that enhances the local field is desirable. We explore the scattering of a gold tip with a finite length. Such tips are used in SNOM experiments and large local field enhancements have been reported [105]. However, it is unknown how strongly this tip interacts with the detector and if the presence of strong absorption in the near field affects, or even destroys the resonant nature of such a tip.

To explore this regime we simulate a sharp metal tip placed above the NbN detector that scatters the incident light to the detector in the optical near field. The sharp tip acts as an antenna or a point-like source, which localizes the light field around its apex. From simulations we find that the absorption of the detector is strongly concentrated and enhanced due to the presence of the tip. This enhancement depends on the wavelength of the incident light, and on the position and geometry of the tip. Here we report the absorption of the detector in a scattering SNOM as a function of the tip geometry and compare this to previous studies of the enhanced local field of the bare tip.

Figure 6.1 shows the detailed geometry of the gold tip and the detector used in the simulation. As shown in Fig. 6.1(a) the tip is modeled as a combination of a cone (semi-angle  $\alpha$  and length  $L$ ) and a hemisphere (radius  $r$ ) at the end. The origin of the coordinates is set at the apex of the tip. In the simulation, tabulated values of the dielectric constant of gold as a function of wavelength

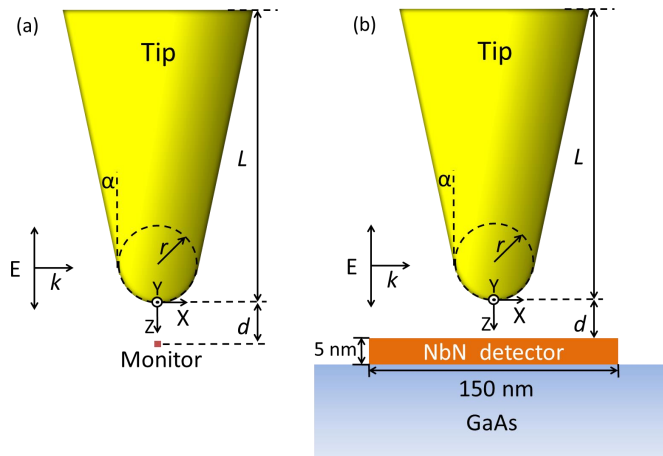


Figure 6.1: Cross section of the 3D model of the bare tip (a) and the tip-nanowire (detector) system (b). (a) The tip has a geometry of a cone with length  $L$  and semi-angle  $\alpha$  and ends in a semi-sphere of radius  $r$ . For the bare tip the electric field is monitored at a position of 5 nm away from the tip apex ( $z = 5$  nm). (b) The detector is 150 nm wide and 5 nm thick on a semi-infinite GaAs substrate. The gap  $d$  between the tip and the detector is fixed to 5 nm. The polarization of the incident light is parallel to the long axis of the tip.

[71,106] are used to calculate the optical response of the bare tip. The incident light propagates in a direction perpendicular to the long axis of the tip and is polarized with the electric field parallel to the long axis of the tip, which leads to strong electric field enhancement at the tip apex [99,107,108].

Figure 6.1(b) shows the tip-detector system. In order to make the 3D simulations efficient we consider only the constricted point of the NbN nanowire, i.e., the active area of the detector. The nanowire is thus reduced to a 150 nm  $\times$  100 nm slab of NbN with a thickness of 5 nm. The underlying GaAs substrate is treated as semi-infinite. To calculate the optical properties of this tip-detector system we use tabulated values of the dielectric constant of the GaAs substrate [71]. The angular frequency dependence of the dielectric constant of NbN is extracted from a Drude model [104]. We use

$$\varepsilon(\omega) = \varepsilon_{high} - \frac{\varepsilon_{high}\omega_p^2}{\omega^2 + i\gamma\omega},$$

where  $\omega_p = 5.28 \times 10^{15}$  rad/s is the plasma frequency,  $\gamma = 3.77 \times 10^{15}$  rad/s is the damping constant of the plasma excitation, and  $\varepsilon_{high} = 12.5$  is the relative permittivity in the high frequency limit.

The influence of the tip geometry is investigated at a reference wavelength of 1000 nm. At this wavelength the complex valued dielectric constant of gold,

NbN and the GaAs substrate are  $\varepsilon_{Au} = -38.13 + 3.47i$ ,  $\varepsilon_{NbN} = -15.57 + 58.62i$  and  $\varepsilon_{GaAs} = 12.25$ , respectively. As a rule of thumb, the sharp tip serves as an antenna, which localizes the electric field into a limited area within a range of  $2r$  from the end of the tip [109]. Therefore, the gap  $d$  between the tip and the nanowire is fixed to 5 nm, to place the detector in the area of resonantly enhanced electric field of the tip.

## 6.2 Wavelength dependence and resonantly enhanced absorption

In a scattering SNOM a good conductive, sharp tip with a radius much smaller than the excitation wavelength functions as an optical antenna, which localizes the electric field and enhances the intensity of the field. Enhancement of  $|E|^2$  up to a factor of  $\sim 10^3$  was reported [48]. Two mechanisms that localize the electric field can be identified: the local resonance of surface electron oscillation (surface plasmon effect) [48] and the local field increase due to sharp edges and curvatures (lightning rod effect) [49]. Both mechanisms depended on the geometry of the tip in a nontrivial way. In order to understand the more complicated tip-detector system, we start by calculating the enhancement of the electric field around a bare gold tip.

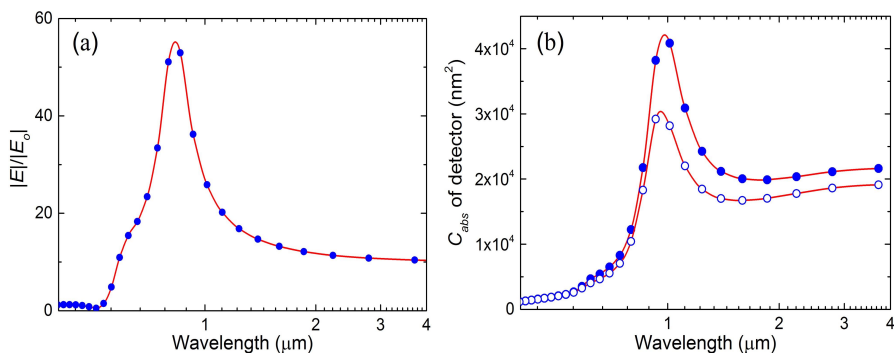


Figure 6.2: Electric field enhancement spectrum for the bare tip (a) and absorption spectrum of the nanowire (b). The dots represent the FDTD simulation results and the red curves serve to guide the eye. For figure (b) the two sets of data represent two settings of gap  $d$ : 5 nm (closed symbols) and 10 nm (open symbols).

Figure 6.2(a) shows the electric field enhancement at  $z = 5$  nm below the tip as a function of wavelength of the incident light for a tip with length  $L = 200$  nm, apex radius  $r = 10$  nm and cone semi-angle  $\alpha = 15^\circ$ . We define the field enhancement factor  $F$  as  $|E|/|E_0|$ , where  $E$  is the modulus of the total electric field in the presence of the tip and  $|E_0|$  is the amplitude of the incident electric field. The spectrum is obtained by using a pulsed excitation

in the FDTD simulation. We use a pulse with a Gaussian envelope function with a width of 2.67 fs, which multiplies a sinusoidal carrier wave with a center wavelength of 800 nm. The enhancement factor shows a main resonant peak at wavelength of  $\sim 850$  nm and a small feature at  $\sim 650$  nm. The peak originates from the surface plasmonic resonance, for which the electrons are driven by the electric field parallel to the  $z$  axis. We attribute the feature at 650 nm to a higher (second) order of this resonance mode, which has a shorter resonant wavelength [44].

Figure 6.2(b) shows the absorption of the nanowire in the presence of the tip as a function of wavelength. The geometry of the tip is identical to the one used in the calculation of Fig. 6.2(a). A resonance in the absorption of the nanowire is observed that resembles the field enhancement of the bare tip. We attribute this enhanced absorption to the plasmonic resonance of the tip that is damped by the detector. This damping becomes apparent when comparing the data in Figs. 6.2(a) and 6.2(b). The resonant wavelength of the bare tip is close to 850 nm, while the resonance in the presence of the detector is red-shifted to  $\sim 1000$  nm. This redshift is partly due to the presence of the high-index substrate and partly due to the detector that acts as a resistive load and damps the antenna (tip) resonance [110, 111]. The loading effect of the detector is calculated for a distance  $d = 5$  nm (closed symbols in Fig. 6.2(b)) and  $d = 10$  nm (open symbols in Fig. 6.2(b)).

To further analyze the two sets of data in Fig. 6.2(b), we determine the peak wavelength  $\lambda_0$ . The lack of a description of the background absorption makes it difficult to extract parameters other than the peak wavelength of the resonance in an unambiguous way. For the two gap settings we find  $\lambda_0 = 975 \pm 5$  nm for  $d = 5$  nm and  $\lambda_0 = 950 \pm 5$  nm for  $d = 10$  nm, where the estimated error bars represents an estimate of the error due to the varying background. Following the discussion above, the larger gap of 10 nm should result in an antenna (tip) with a smaller load, and gives a smaller redshift compared the the system of  $d = 5$  nm. This is consistent with the calculation presented in Fig. 6.2(b).

### 6.3 Electric field enhancement by the bare tip

In order to study the influence of the geometry of the tip on the enhancement factor, we simulated the tip with excitation of a Gaussian beam at a single wavelength of 1000 nm. The effect of these geometrical parameters on the tip resonance and field-enhancement is well-known. We reproduce these results here for completeness and to obtain a reference for the more complicated geometry of the tip-detector system.

Figure 6.3 shows the enhancement factor as a function of tip length  $L$ , apex

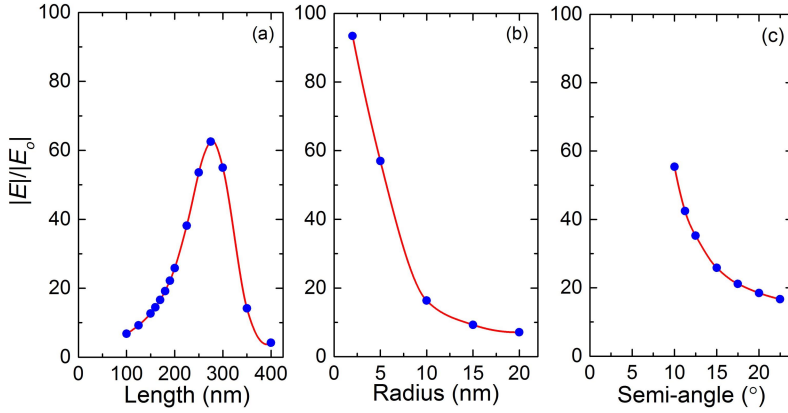


Figure 6.3: Electric field enhancement at a wavelength of 1000 nm in the near field as a function of tip geometry. (a) The enhancement factor is calculated at  $z = 5$  nm with a resonance peak at  $L \approx 275$  nm for fixed values of the tip radius  $r = 10$  nm and semi-angle  $\alpha = 15^\circ$ . (b) The data points of the enhancement factor as a function of radius are obtained at the position of  $z = r$  for fixed values of the tip length  $L = 200$  nm and semi-angle  $\alpha = 15^\circ$ . (c) The enhancement factor as a function of semi-angle is calculated at the position of  $z = 5$  nm for fixed values of the tip radius  $r = 10$  nm and length  $L = 200$  nm.

radius  $r$  and semi-angle  $\alpha$ . The resonance of the surface plasmon is determined primarily by the tip length  $L$ , and with incident light at 1000 nm the resonance occurs at  $L \approx 275$  nm.

Since the electric field is mainly concentrated in a range of  $2r$  around the tip, we monitor the electric field at the position of  $z = r$ . The influence of the apex radius  $r$  is shown in Fig. 6.3(b) and a monotonic decrease of the enhancement factor with the radius of the tip is observed. The radius  $r$  of the rounded tip has minimal influence on the plasmonic resonance, but strongly influences the lightning rod effect that is related to a field singularity at the apex of an infinitely sharp tip. For a finite apex radius, the charge density at the apex is reduced for larger values of  $r$  due to the increased area of the tip apex. Therefore the electric potential is lowered and the electric field at the tip becomes weaker.

The influence of the semi-angle  $\alpha$  is reported in Fig. 6.3(c) and shows that the enhancement of the electric field decreases with semi-angle. This effect is well understood and can be explained by a simple model of a sharp cone, around which the electric field is  $E(z) \propto z^{\nu-1}$ , where  $\nu$  is between 0 and 1 and is determined by the semi-angle [112]. The exponent  $\nu$  increases for large semi-angles, which results in slower field decay and smaller enhancement factor.

## 6.4 Absorption of the nanowire with the tip

The tip geometry-dependent absorption cross section of the nanowire is calculated in a similar way as the enhancement factor at a wavelength of 1000 nm. Figure 6.4 shows the absorption as a function of length  $L$ , radius  $r$  and semi-angle  $\alpha$ . The absorption with the tip is higher than that without tip (dashed line) due to the enhanced local electric field. The influence of the geometry of the tip is reported in the three subfigures and is qualitatively similar to the behavior for a bare tip. We interpret this result in the sense that the same mechanisms of electric field enhancement of the bare tip are responsible for the absorption enhancement despite the strong damping induced by the detector.

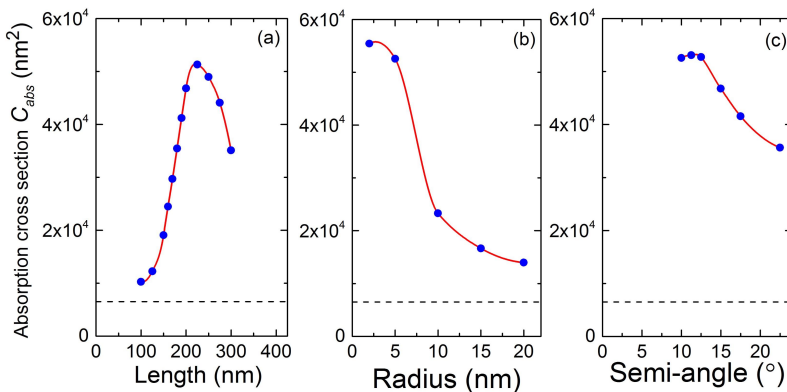


Figure 6.4: Absorption cross section of the nanowire as a function of the geometry of the tip at a wavelength of 1000 nm. The dashed line is the absorption cross section without the tip as a reference. (a) The absorption cross section is calculated at  $z = 5$  nm with a resonance peak ( $L = \sim 225$  nm) with  $\alpha = 15^\circ$  and  $r = 10$  nm. (b) The data points are obtained at position  $z = r$  to make sure most of the nanowire is in the area of the enhanced electric field. Other settings of geometry are set to  $\alpha = 15^\circ$  and  $L = 200$  nm. (c) The absorption cross section is calculated at the position of  $z = 5$  nm as a function of semi-angle with  $r = 10$  nm and  $L = 200$  nm.

Figure 6.4(a) shows that the resonance occurs for a length  $L = 225$  nm for the loaded tip compared to  $L = 275$  nm for the bare tip. We explain this shift in tip length by a phase-shift in the amplitude reflection coefficient of the tip due to the resistive load of the detector. As a result the resonance has a lower quality factor and occurs in a shorter length antenna. For Figs. 6.4(b) and 6.4(c) we stress that the absorption (cross section) of the nanowire is proportional to the integral of  $|E|^2$  over the whole nanowire, and this integral over a relative larger region (nanowire) varies more slowly than the electric field in a single point on the  $z$  axis. Hence, Figs. 6.4(b) and 6.4(c) show a smooth change (especially at small radii and semi-angles) instead of the strong dependence in Figs. 6.3(b) and 6.3(c).

## 6.5 Conclusions

We have calculated the electric field enhancement around a sharp, conical, gold tip illuminated by a plane wave from the side. The strong field enhancement of a bare tip originates from surface plasmon resonance and lightning rod effect. The resonant wavelength of the field enhancement is mainly determined by the length of the tip, and depends strongly on the apex radius and cone semi-angle. The enhancement becomes smaller when the radius or semi-angle of the tip increases because the lightning rod effect related to a field singularity at the tip apex is strongly reduced. When a NbN nanodetector is placed in the near-field region of strongly enhanced field we observe that the absorption of light by the nanodetector is resonantly enhanced. At the same time strong shifts in the resonance wavelength (up to 10%) are observed due to the strong resistive load on the tip. Despite the strong damping the absorption of the nanodetector as a function of tip geometry is very similar to the trends observed in the field enhancement of a bare tip. The bare tip can thus be used as a starting point for the design of enhanced near-field detection of single photons. Improvements to the simple description of the bare tip are expected if the model takes into account that the nanodetector acts as a resistive load on the antenna (tip) and that it damps the radiation of the tip.

## Chapter 7

# Local Detection Efficiency of a NbN SSPD Explored by a Scattering SNOM

We propose an experiment to directly probe the local response of a superconducting single-photon detector using a sharp metal tip in a scattering scanning near-field optical microscope. The optical absorption is obtained by simulating the tip-detector system, where the tip-detector is illuminated from the side, with the tip functioning as an optical antenna. The local detection efficiency is calculated by considering the recently introduced position-dependent threshold current in the detector. The calculated response for a 150 nm wide detector shows a peak close to the edge that can be spatially resolved with an estimated resolution of  $\sim 20$  nm, using a tip with parameters that are experimentally accessible <sup>1</sup>.

### 7.1 Introduction

Scanning near-field optical microscopes (SNOMs) beat the diffraction-limit of conventional optical microscopes and are able to probe nanoscale structures such as single molecules [113], plasmonic antennas [114] or graphene [115], by scattering part of the optical near field via a sharp tip (scattering-SNOM or s-SNOM) or a metal coated fiber (aperture-SNOM or a-SNOM) to a photon

---

<sup>1</sup>Q. Wang, J. J. Renema, A. Engel, M. P. van Exter, and M. J. A. de Dood, *Opt. Express* **23**, 24873, (2015).

sensitive detector placed in the optical far field. However, the signal collection in SNOMs is extremely inefficient, because the Rayleigh scattering process between the sample and the subwavelength apex of the tip or the fiber has a scattering cross section proportional to  $a^6/\lambda^4$ , where  $a$  is the size of the apex. Typical values of  $a$  are  $\sim 1/10$  to  $1/50$  of the incident wavelength  $\lambda$ . The low efficiency limits the application of SNOM in quantum optics, which requires very high signal collection efficiency. Chapter 5 shows a highly efficient near-field probe made out of a nanoscale NbN superconducting single-photon detector (SSPD), which gives two orders of magnitude higher absorption compared to a conventional SNOM.

According to the calculation of optical absorption in Chapter 5, the spatial resolution of the nano SSPD under the illumination of a point light source (a radiative electric dipole) is estimated to be approximately equal to the dimension of the nano SSPD. Studies on the spatial dependence of the response of SSPD on a micrometer or sub-micrometer scale have been reported [116,117]. Recent experiments [35] and modeling [25] of SSPDs show that the response of the SSPDs consist of not only the optical absorption but also the internal detection efficiency that is related to the intrinsic detection process. Hence, the spatial resolution of the SSPD is not trivial, and contains information about the intrinsic photon-detection process and is worthy of being investigated for applications in optical near-field microscopy. Moreover, these detectors are technologically interesting because the very thin and narrow wire can be used to detect single photons over a broad wavelength range with minimal timing jitter, small detector dead-time and high system detection efficiency [17].

In this chapter we use a short metallic tip in an s-SNOM to investigate the local response of a strongly absorbing SSPD, which is based on the fact that the sharp tip can localize the illuminated light field and act as a point-like light source to probe the SSPD in the optical near field. When the superconducting nanowire is biased close to its critical current, absorption of a single photon can induce a transition from the superconducting to the normal state. This transition leads to a voltage difference that can be amplified to create a measurable signal.

Three steps are needed to understand the photon detection process in SSPDs: the photon absorption [42, 65], the generation of the voltage pulse and the self-resetting mechanism [33]. The initial and final steps are well-understood. Recently, significant progress has also been made in the understanding of the intermediate step [25, 30, 60], where the absorbed photon leads to a transition of a cross section of the wire to the normal state that leads to the voltage pulse. Experimental results for visible to near-infrared wavelengths absorbed by a short NbN nanowire confirm predictions from a photon-assisted vortex-entry model [25]. In this model, photon absorption leads to a decrease of the locally available Cooper pairs that carry the current in the supercon-

ductor. The initial excitation diffuses in the superconductor without breaking superconductivity and lowers the edge barrier for vortex entry. If this barrier is lowered enough, a magnetic vortex transits the wire cross section and dissipates additional energy that triggers the detector. A direct consequence of the photon-assisted vortex-entry model is that the absorption of a photon near the edge of the wire is more efficient than absorption in the center, because this directly affects the redistribution of supercurrent at the edge.

A local detection efficiency  $LDE(x)$  can describe the position-dependent detector response [35]. The typical length scale over which this  $LDE(x)$  can vary is set by diffusion of electrons from the position of initial excitation, which is about 10 – 30 nm. Further experiments are needed that either measure this size or that explore the dynamics of electrons and quasiparticles in a NbN nanowire. A conventional a-SNOM based on a scanning aperture is typically limited by the skin-depth of the metal used to create the aperture. Even for good conductive metals, such as gold, this limits the resolution to  $\geq 20 - 50$  nm. Therefore, we explore the possibility to use an s-SNOM to probe a NbN nanowire with a spatial resolution comparable to 10 nm, using the calculated position-dependent response [25] of the detector as a reference.

It remains an open question, if the s-SNOM technique can be applied successfully to strongly absorbing structures such as the NbN nanowire considered here. The resolution and sensitivity of s-SNOM is determined by the shape and resonant nature of the tip that strongly enhances the field at the tip vertex. In the presence of a good metal or low loss dielectric substrate the tip-sample interaction can be understood via an image dipole of the tip in the substrate [94]. Because the losses are minimal, the resonant enhancement of the field that is critical to the operation of the s-SNOM is not negatively influenced by the substrate. This situation drastically changes when the resonant nature of the tip is damped by a strongly absorbing sample in the near field. To explore the effect of the detector on the tip resonance and to evaluate the performance of the proposed scanning probe we perform numerical finite-difference-time-domain (FDTD, FullWave package, RSoft [71]) calculations that we combine with a model of the photon detection process in order to simulate the complete response of the superconducting detector.

## 7.2 Simulation configuration

We calculate the optical response of a superconducting single-photon detector in an s-SNOM via the FDTD method. Figure 7.1 shows the geometry of the NbN single nanowire (100 nm long, 150 nm wide and 5nm thick) in between two tapered parts on a semi-infinite GaAs substrate. The NbN single nanowire has dimensions identical to a device that has been studied experi-

mentally [35, 38]. This simple design avoids the problem of current-crowding that occurs in the bends of meandering structures that are usually used in SSPDs [26, 41].

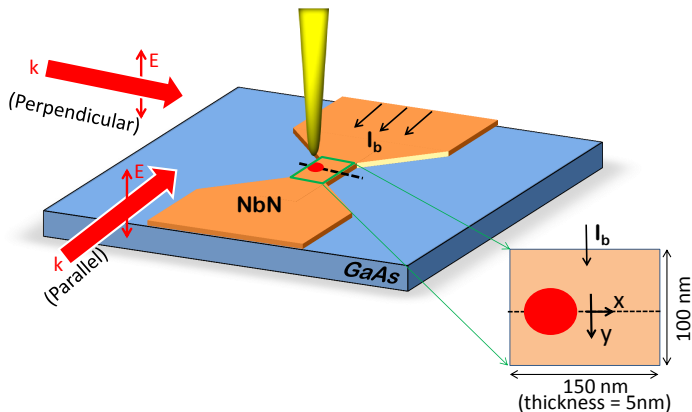


Figure 7.1: Schematic diagram of the tip-detector system in a scattering SNOM considered in the simulation. A 5 nm thick NbN film on a GaAs substrate is patterned into a short wire in between two tapered parts. Only the central part of the wire with a width of 150 nm and a length of 100 nm is considered in the simulation. A rounded and conical gold tip is positioned above the detector with a fixed height of 5 nm and scanned in either  $x$ - or  $y$ -direction. The tip-detector system is illuminated by a plane wave with a wave-vector  $k$  either parallel or perpendicular to the single wire. The incident field is polarized with the electric field along (parallel to) the long axis of the tip. The simulation area is 200 nm by 200 nm by 250 nm in the  $x$ ,  $y$  and  $z$ -directions with a Perfectly Matched Layer at the boundaries.

In the experiment that we simulate, the detector placed in a cryostat is cooled below its critical temperature ( $\sim 10$  K), and is biased with a current  $I_b$ , close to the critical current  $I_c$ . Absorption of the energy of a single photon can drive the nanowire from the superconducting state to the normal state with some internal probability. Once the wire is in a resistive state a voltage difference over the wire is generated that can be amplified and read out with pulse counting electronics.

The dielectric constants of GaAs and gold are taken from RSoft Library [71] and Ref. [106], respectively. The dielectric constant  $\epsilon_{NbN}$  of NbN is described by a Drude model [104], which makes NbN a metal-like material but with strong absorption or Ohmic loss due to the large imaginary part of  $\epsilon_{NbN}$  [47].

Figure 7.2 shows the configuration of the s-SNOM with a gold tip in the shape of a rounded cone above the detector. The gap between the tip and the nanowire is set to 5 nm, because this distance ensures that the detector is within the near field of the tip, while avoiding problems of electron tunneling [118–

120]. For example, at sub-nanometric scale ( $\sim 5\text{\AA}$ ) the electronic densities of the individual sub-nanostructures tend to overlap and the field enhancements of the resonant modes cannot be described by a classical description, and quantum effects need to be accounted for [120].

The incident light illuminates the detector and tip from the side and has a wave-vector  $k$  that is either parallel or perpendicular to the wire. The polarization of the incident light is kept constant with its electric field parallel to the long axis of the tip, which leads to a strong electric field enhancement at the tip. For this polarization the induced surface charge density is symmetric about the long axis of the tip and has the highest amplitude at the end of the tip, leading to a large enhancement of the local electric field. For an electric field perpendicular to the tip the surface charge is distributed diametrically at opposed points on the tip, and very little charge is accumulated at the apex of the tip, and the enhancement of the electric field is negligible [48].

To reduce the computational time for 3D FDTD calculation<sup>1</sup>, we concentrate on the central nanowire of the detector, namely the active area shown as the magnified section in Fig. 7.1. The considered nanowire has a size of 150 nm (width,  $x$ -direction) by 100 nm (length,  $y$ -direction) by 5 nm (thickness,  $z$ -direction), and the entire simulation area is 200 nm ( $x$ -direction) by 200 nm ( $y$ -direction) by 250 nm ( $z$ -direction). At the boundaries a Perfectly Matched Layer (PML) with thickness of 50 nm and reflection of  $10^{-12}$  is added. The spacing of grid points is set to 0.25 nm on the boundary of the NbN film and to 0.5 nm inside the film.

Limiting the simulation to the central part is justified because the localized electric field area given by the tip is confined to an area  $\sim 50$  nm compared to the 100 nm long wire of the detector in the simulation. The “contacts” or the tapered parts have little influence on the electric field distribution in the central nanowire [35], because the NbN material does not support surface plasmons modes due to the strong damping. This eliminates the capacitive coupling between the tapers that is responsible for the resonance in antennas made from more plasmonic metals such as Au or Ag. The simulation volume used in this work is sufficient to answer the main physical questions we are interested in. We have tested the stability of the FDTD with a simple model of a stratified, 5 nm thick, NbN film and find that the simulated optical properties deviate less than 1.5% from the analytical solution.

The simplified settings make simulation of a single configuration possible within a reasonable amount of time ( $\sim 7$  hours). The optical absorption of the nanowire is recorded and analyzed.

---

<sup>1</sup>A typical simulation involves  $3 \times 10^6$  grid points and  $1.8 \times 10^4$  time steps and takes approximately 400 minutes to complete on a PC (Intel Xeon E5420, 2.54 GHz, 16.0 GB RAM)

### 7.3 Enhanced electric field and absorption

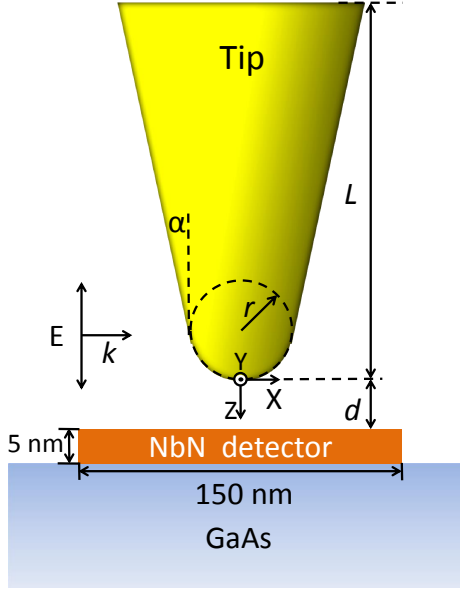


Figure 7.2: Cross section of the 3D model with the tip above the center of the detector. The geometry of the tip is set in the way of  $\alpha = 15^\circ$ ,  $r = 10$  nm, and  $L = 200$  nm. The central nanowire of the NbN detector is 150 nm wide and 5 nm thick on a semi-infinite GaAs substrate. The gap  $d$  between the tip and the detector is fixed to 5 nm. The polarization of the incident light is parallel to the long axis of the tip. The origin of the coordinates is placed at the bottom of the tip and its  $z$ -axis points to the nanowire.

Figure 7.2 shows the detailed geometry of the gold tip. The origin of the coordinates is set at the bottom of the tip with the positive  $z$ -axis pointing to the detector. The tip is modeled as a combination of a cone (semi-angle  $\alpha = 15^\circ$  and length  $L = 200$  nm) and a hemisphere (radius  $r = 10$  nm) at the end. The parameters of the tip are chosen as a realistic design amendable to fabrication. More detailed information about how each of the geometric parameters ( $\alpha$ ,  $L$ ,  $r$ ) influences the absorption in the detector is included in Chapter 6.

As a rule of thumb, the sharp tip serves as an antenna which localizes the electric field into a limited area within a range of  $2r$  from the end of the tip [109]. Hence, the gap  $d$  between the tip and the nanowire is fixed to 5 nm, to place the detector in the area of enhanced electric field.

Figure 7.3 shows the absorption cross section of the NbN detector with tip as a function of wavelength to illustrate the resonant enhancement of the absorption by the tip. To calculate the wavelength dependence, we use a well

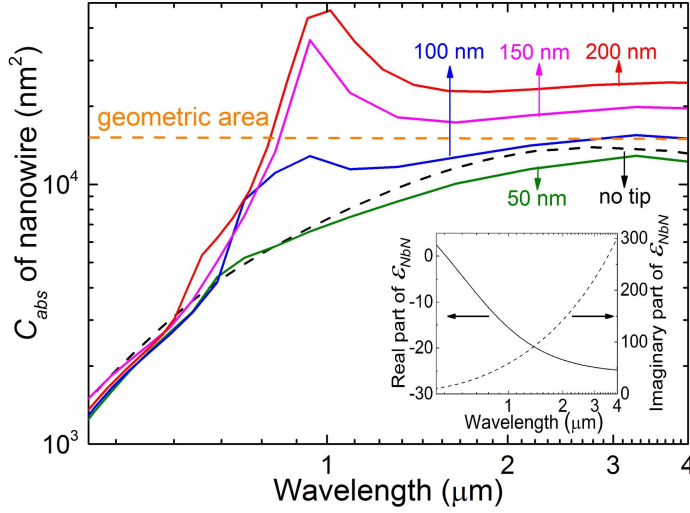


Figure 7.3: Calculated absorption cross section  $C_{abs}$  of the nanowire as a function of wavelength in the presence of a tip of varying length. The black dashed line is the absorption of the nanowire without tip and the colored curves are with tips of different lengths from 50 nm to 200 nm. As a reference, the horizontal dashed line shows the geometry area of the  $100 \times 150 \text{ nm}^2$  nanowire. The real and imaginary parts of the relative permittivity of NbN are shown in the inset.

defined pulse with a Gaussian envelope function with a width of 2.67 fs, which multiplies a sinusoidal carrier wave with a center wavelength of 800 nm [71].

The horizontal dashed line in Fig. 7.3 indicates the  $100 \times 150 \text{ nm}^2$  geometric area of the nanowire, as a reference. The inset of Fig. 7.3 demonstrates the relative permittivity of NbN based on the Drude model [104]. The imaginary part, which dominantly determines the absorption in the nanowire, increases monotonically with wavelength. This agrees well with the trend of the absorption increase of the nanowire without tip (black dashed line in Fig. 7.3). The solid curves are calculations of the absorption cross section of the nanowire in the presence of a tip with varying lengths from 50 nm to 200 nm (the curvature radius and the semi-angle of the tip are kept constant). The length of the tip determines the resonance condition for surface plasmons along the tip and causes the resonance to shift to the blue as the tip becomes shorter [44]. From these calculations we observe that for a tip length of 200 nm the absorption is about one order of magnitude higher than that without tip at the resonant wavelength of  $\sim 1000 \text{ nm}$ . This peak originates from the fundamental mode of the surface plasmon resonance in the tip. A feature can be distinguished in the shoulder of the main resonance around a wavelength of 650 nm that we attribute to the second order mode of the surface plasmon standing wave along the tip [44, 48].

In order to better understand the enhancement of the detector absorption, we calculate the electric field of the tip-detector system for a constant wavelength of 1000 nm, close to the resonance in absorption. We introduce an enhancement factor  $F = |E/E_o|$ , where  $E$  is the total electric field in the presence of the tip and  $E_o$  is the incident electric field. We simulate the enhancement factor  $F_f$  for the “free tip” by considering a bare tip in vacuum without nanowire and substrate, as well as the factor  $F_l$  for the “loaded tip” for the configuration depicted in Fig. 7.2. Figure 7.4 shows the enhancement as a function of position along the  $z$ -axis where  $z = 0$  corresponds to the end of the tip. The black and red colors stand for  $F_f$  in vacuum and  $F_l$  in the presence of the nanowire and substrate, respectively.

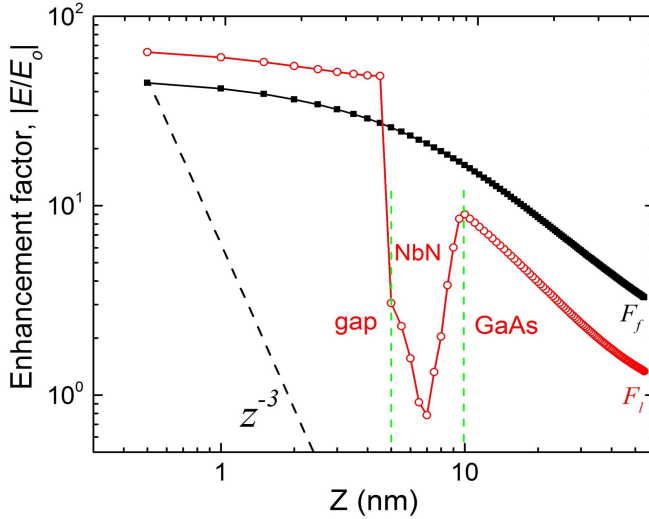


Figure 7.4: Simulations of the electric field enhancement of a gold tip close to the nanowire along the long axis of the tip ( $z$ -axis). The black squares ( $F_f$ ) are the field enhancement of a bare tip without nanowire and substrate, and it is fitted to the sharp cone model (black curve). The red dots ( $F_l$ ) are the calculated field enhancement in the presence of the nanowire and the substrate. For comparison the dashed line shows the behavior of  $z^{-3}$  for the field enhancement in the near field of a radiative dipole. Two green vertical dashed lines separate the red dots into three regions: the “gap” region (5 nm) between the tip and nanowire, the “NbN” film region, and the “GaAs” substrate region.

As can be seen, the enhancement  $F_f$  is largest close to the tip and decreases away from the end of the tip. To understand the  $F_f$ , we fit the black dots to a model of a sharp, perfect-conductive cone with an expression of  $F_f(z) = F_o(1 + z/z_o)^{\nu-1}$  [112, 121], where  $F_o = F(z = 0) = 48.5 \pm 0.2$ ,  $z_o = 8.7 \pm 0.2$  nm and  $\nu = -0.42 \pm 0.01$ . The value of the parameter  $\nu$  is determined by the semi-angle  $\alpha$  of the tip [112].

For an infinite, perfect-conductive and sharp cone, its localized electric field is expressed by  $E(z) \propto z^{\nu-1}$  with  $0 < \nu < 1$  [112], and contains only contributions from the lightning rod effect [49], because the surface plasmon resonance mode does not exist along a tip with an infinite length. For pure electric dipole radiation caused by a surface plasmon resonance, the decay of  $F_f$  should show a  $z^{-3}$  ( $\nu = -2$ ) behavior (dashed line in Fig. 7.4) [79].

In our calculation for a finite and rounded cone the fitting parameter  $\nu = -0.42 \pm 0.1$  is between the two extreme cases. This indicates a combination of the two mechanisms: the local resonance of surface electron oscillation (surface plasmon) and the local field increase due to curvature (lightning rod effect).

With the nanowire and substrate the  $F_l$  becomes complicated. As shown in Fig. 7.4, the  $F_l$  (red dots) has three parts, divided by two vertical dashed lines. The first part corresponds to the vacuum “gap” region between the tip and the nanowire. The  $F_l$  of this region is higher (50 – 65) than that of the vacuum case (27 – 45) (black squares). The difference is due to reflection of the field by the nanowire that constructively interferes with light scattered by the tip [122].

The middle part, where the 5 nm thick NbN film lies, has a very low  $F_l$  caused by the very lossy nature of NbN. The relative permittivity of NbN is set to  $\varepsilon_{NbN} = -15.57 + 58.62i$  according to the Drude model, where the large imaginary part makes it very lossy. Because of this it is hard for electrons in the NbN film to be driven by the external field, leading to a weak electric field and a low  $F_l$  consequently. For the  $F_l$  in the GaAs substrate the electric field penetrating into the substrate is relative low due to the large dielectric constant of the GaAs  $\varepsilon_{GaAs} = 12.25$ .

In our calculation we choose a simple setting of a 200 nm long tip without any support for simplicity. In practice the tip can be fabricated on a silicon pillar [44]. We perform additional simulations for the tip with a silicon support (not shown here), that show that the resonance of the tip is broadened and redshifted, because the support on one end of the tip functions as a load. This lowers the surface plasmon resonance quality factor and induces a redshift [123]. The absorption area remains within 50 nm. This can be explained because at the other end of the tip, the localization of the electric field originates from both the surface plasmon resonance and the lightning rod effect. The latter effect is determined by the unchanged semi-angle and the radius of the tip. Therefore we expect that a tip with support will lead to very similar conclusions.

## 7.4 Position-dependent absorption and local detection efficiency

There are two factors that together determine the efficiency of a detection event in the detector: the spatial distribution of optical absorption and the local detection efficiency  $LDE(x)$ . The optical absorption over the detector corresponds to the fraction of light (or probability of a photon) absorbed in the active area (nanowire) of the detector, and the local detection efficiency quantifies the probability for the absorbed light (or photons) to trigger the detector.

To model these two effects, we assume that the overall detection efficiency or the normalized photon count rate  $R$  can be expressed as follows:

$$R(x_{tip}, I_b) = \int \int A(x_{tip}, x, y) * LDE(x, I_b) dx dy \quad (7.1)$$

where  $A(x_{tip}, x, y)$  (in unit of  $\mu\text{m}^{-2}$ ) is the optical absorption distribution in the  $x$ - $y$  plane of the nanowire with the tip at a position  $x_{tip}$  and  $LDE(x, I_b)$  is the local detection efficiency across the nanowire, which is assumed to depend on position and bias current at a constant photon energy (wavelength). In our calculation we keep  $y_{tip} = 0$  and the gap  $d = 5$  nm constant, to focus our attention to an experiment where the tip is scanned in a direction across the nanowire. We will discuss the details of these two factors separately.

The absorption distribution  $A(x, y)$  with the tip at  $x_{tip}$  is expressed as follows [79]:

$$A(x_{tip}, x, y) = \frac{P_{abs}(x_{tip}, x, y)}{P_{total}} = \frac{\int_0^t \frac{1}{2} \omega \varepsilon_o \text{Im}(\varepsilon_{NbN}) |E(x_{tip}, x, y, z)|^2 dz}{P_{total}}, \quad (7.2)$$

where  $P_{total}$  is the total illumination power,  $P_{abs}(x, y)$  (in unit of  $\text{W}\mu\text{m}^{-2}$ ) is the absorbed power density in  $x$ - $y$  plane,  $\omega$  is the angular frequency of the incident light,  $\varepsilon_o$  is vacuum permittivity,  $t = 5$  nm is the thickness of the NbN film, and  $|E(x_{tip}, x, y, z)|^2 = |E_x|^2 + |E_y|^2 + |E_z|^2$ .

In Eq. (7.1) the absorption distribution is independent of  $z$  and simplified by the integral of Eq. (7.2). This approximation is reasonable since the 5 nm thick NbN film is much thinner than the skin depth of  $\sim 70$  nm at the relevant wavelength of 1000 nm. The absorption is uniform over the thickness of the film. Figure 7.5 shows the absorbed power  $P_{abs}(x_{tip}, x, y)$  (a) and electric field components  $E_x$  (b) and  $E_y$  (c) in the nanowire with the total illumination power  $P_{total} = 1$  W. In this simulation the tip is above the center of the wire ( $x_{tip} = y_{tip} = 0$ ) and the wave vector of the incident light (monochromatic Gaussian beam) is pointing in the negative  $y$ -direction. As can be seen in the

figure, the absorption is concentrated within a 50 nm area of the central part of the nanowire, as a result of the strongly localized electric field of the tip. The localized absorption area is asymmetric, because the illumination direction is along the  $y$ -axis, and part of the light is reflected back by the metal tip.

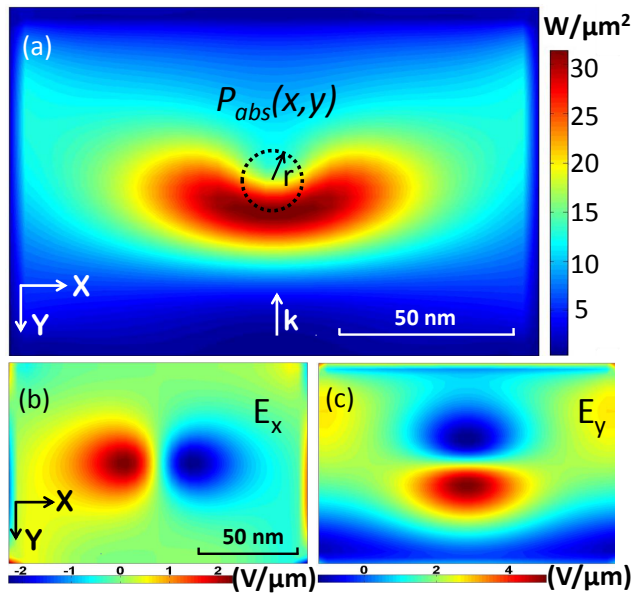


Figure 7.5: The position-dependent time-averaged absorbed power  $P_{abs}(x, y)$  for a tip centered at  $x_{tip} = y_{tip} = 0$  with the total illumination power of 1 W(a). The tip is located above the center of the nanowire and illuminated by light incident from the positive  $y$ -direction. The central part is circled in dashed curve with the radius of the tip curvature  $r = 10$  nm. Electric field components  $E_x$  (b) and  $E_y$  (c) in the  $150$  nm  $\times$   $100$  nm nanowire demonstrating the radiative electric dipole nature of the tip. Components  $E_x$  and  $E_y$  are displayed at the moment of maximum amplitude contrast in the lobes that oscillate out of phase.

In order to understand the shape of the absorption distribution, we plot the position-dependent components  $E_x$  and  $E_y$  of the electric field in Figs. 7.5(b) and 7.5(c), respectively.  $E_x$  displays a pair of lobes that oscillate out of phase. The field pattern  $E_y$  shows a more complicated oscillation with multiple lobes, and the amplitude of the bottom lobe (red) is higher than that of top one (blue), as a consequence of the asymmetry of the absorption area.  $|E_z|$  (not shown) is isotropic with its maximum value in the center. All these components are typical features of a radiative electric dipole, originating from the surface plasmon oscillation excited by the external field.

The results for illumination along the  $x$ -axis are similar, with the absorption

pattern in Fig. 7.5(a) rotated by  $90^\circ$  clockwise. This proves that the electric field is strongly concentrated at the tip (within  $\sim 50$  nm) and is not influenced by the edges of the nanowire or the tapered parts at the two ends when the tip is located above the center of the nanowire.

In order to calculate the local detection efficiency  $LDE(x, I_b)$  we consider the photon-assisted vortex-entry model in Ref. [25] and the experimental results in Ref. [35]. According to this model the absorbed photon excites one electron in the NbN film. The electron thermalizes via inelastic scattering with other electrons, Cooper-pairs and the lattice, generating a localized cloud of quasi-particles. This cloud of quasi-particles diffuses and leads to the local decrease of the superconducting electron density. Consequently, the vortex pinned at the edge of the nanowire has an increased possibility to enter the nanowire due to the decrease of the barrier potential. The energy dissipation of this moving vortex triggers a detection event.

A distinctive feature of such a model is that photon absorption at the edge is more likely to lead to a photon detection. An absorption event at the edge of the wire reduces the current density at the edge due to the reduction in the number of superconducting electrons, which slightly increases the barrier potential. However, this is more than compensated by the reduction of the vortex self-energy, which is proportional to the density of the superconducting electrons. The overall effect is that the total barrier for vortex entry is lowered. Therefore, vortices enter more easily when the superconductivity is weakened at their entry point, and that makes the detector more efficient at the edges. A position-dependent threshold current  $I_{th}(x)$  is sufficient to quantify this local internal efficiency [35]: When bias current  $I_b$  goes beyond  $I_{th}(x)$  with a photon absorbed at position of  $x$ , the energy barrier for a vortex vanishes, leading to the entry of the vortex and to a detection event. Following Ref. [35], we posit a relation between local detection efficiency, bias current and threshold current:

$$LDE(x, I_b) = \min\{1, \exp[(I_b - I_{th}(x))/I^*]\} \quad (7.3)$$

where  $I_b$  is the bias current, and  $I^*$  is a current scale and it can be extracted from experiments by fitting the internal detection efficiency as a function of  $I_b$ . The value of  $I^* = 0.65 \mu\text{A}$  used in this article is based on the experimental data in Ref. [35].

Figure 7.6 shows the  $LDE(x, I_b)$  for several values of  $I_b$  up to the critical current  $I_c$ , for which we adopt the experimental value of  $28 \mu\text{A}$  [35]. For lower bias currents ( $0.7I_c$  and  $0.8I_c$ ) the curves have identical shape but with a different prefactor as expressed by Eq. (7.3). For low bias currents, the value of the probability at the edges is approximately three orders of magnitude higher than that in the center, which implies that the edges are much more sensitive than the center. Higher current (e.g.,  $0.9I_c$ ) leads to saturation of the detection

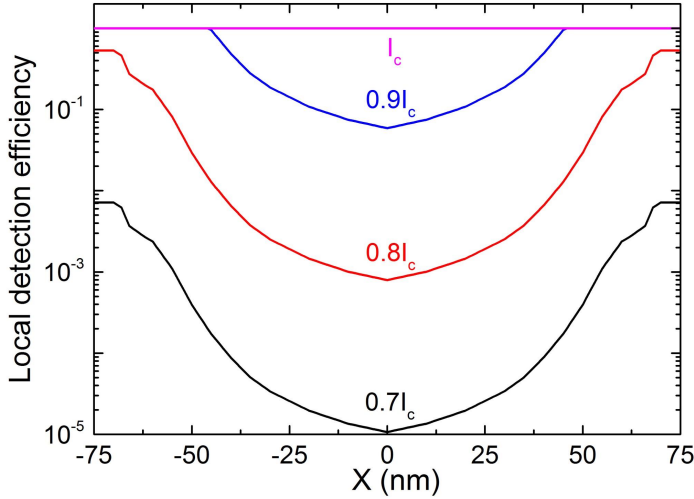


Figure 7.6: Local detection efficiency across the nanowire. The detection efficiency is calculated at bias currents of  $0.7I_c$ ,  $0.8I_c$ ,  $0.9I_c$  and  $I_c$  according to Eq. (7.3).

efficiency near the edges and therefore less contrast. At bias currents close to the critical current ( $I_c$ ) the detector shows a position-independent detection efficiency.

## 7.5 Detector response in a scanning probe experiment

An experiment that measures the light count rate as a function of both bias current and tip position can distinguish between the effect of local absorption and the position-dependent internal detection efficiency. In this section we calculate the detector response of an s-SNOM experiment building on the results from the previous sections. We consider a tip that moves across the wire ( $x$ -direction) with the height of the tip fixed. At each position of the tip we simulate the optical absorption distribution  $A(x_{tip}, x, y)$  of the nanowire, and then we calculate the integral in Eq. (7.1) using the position-dependent local detection efficiency  $LDE(x, I_b)$  at different bias currents from  $0.7I_c$  to  $I_c$ .

Figure 7.7 shows the result of the detector response  $R(x_{tip}, I_b)$  as a function of tip position and bias current for light entering from (a) the  $y$ -direction (parallel illumination) and (b) the negative  $x$ -direction (perpendicular illumination). The region without shade represents the location of the nanowire. As a reference, the dashed lines indicate the detector response without tip. In order to facilitate comparison between curves at different bias currents we normalize the calculated  $R(x_{tip}, I_b)$  as a function of tip position  $x_{tip}$  to its max-

imum value. The whole procedure is repeated for light that is entering parallel and perpendicular to the nanowire.

At lower currents of  $0.7I_c$  and  $0.8I_c$ , the shape of the  $R(x_{tip}, I_b)$  curves is identical, and the only difference between the two curves is a prefactor of  $\sim 10^3$ , which is determined by  $LDE(I_b, x)$ , as shown in Fig. 7.6. The similarity in shape is a direct result of the assumed scaling behavior expressed by Eq. (7.3), and can be verified in a scanning probe experiment at low bias currents. When we consider the higher currents of  $0.9I_c$  and  $I_c$ , the  $LDE(I_b, x)$  first saturates at the edges of the nanowire, leading to differences in the shape of  $R(x_{tip}, I_b)$ .

We note that part of the signal is due to background illumination. In an experiment this background can be distinguished from the signal by varying the tip-detector interaction by modulating techniques [124, 125] that vary the tip-detector distance. The signal of tip-sample (nanowire) interaction depends strongly on the distance to the sample surface while the background of course does not. A modulation of the tip-sample distance with a frequency of  $\Omega$  will also generate higher order harmonics in the near-field signal. This allows us to demodulate the signal at higher frequencies (e.g., at  $2\Omega$  or  $3\Omega$ ).

The detector response (solid curves in Fig. 7.7(a)) for parallel illumination shows a symmetric behavior relative to the  $y$ -axis, because the illumination parallel to the nanowire ( $y$ -axis) makes the incident field symmetric about the  $y$ -axis. For smaller bias currents ( $0.7I_c$  and  $0.8I_c$ ) the response shows an “edge effect”: The response of the detector has maximum values when the tip moves above the edges of the detector. This edge effect contains a contribution of both the internal detection efficiency and optical absorption that are enhanced at the edge. The internal efficiency is enhanced due to the decrease of the vortex-entry barrier caused by photon absorbed on the edge. The absorption is increased due to the sharpness of the nanowire edge when the tip is above the edge [79]. We find that the absorption (or electric field) is strongly localized within a region  $\sim 25$  nm from the edge for a tip above the edge. The combined effect of the high  $LDE(x)$  at the edge and the enhanced absorption near the edge shifts the maximum response towards the edge compared to the maximum absorption.

We observe in Fig. 7.7(a) that the response at the lower currents ( $0.7I_c$  and  $0.8I_c$ ) does not reach its maximum value when the tip is right above the edge at  $x_{tip} = \pm 75$  nm but when the tip is about 10 nm away from the edge at  $x_{tip} \approx \pm 65$  nm. The position of these maxima is determined by the optical absorption integrated over the detectors, which is maximum when the tip is at  $x_{tip} = \pm 65$  nm. The absorption of the nanowire is determined by two factors. The first factor is the local intensity of the electric field at the tip, which has a maximum value when the point-like source is exactly above the edge ( $x_{tip} = \pm 75$  nm). The second factor is the area of the detector that is exposed to the light from the source, and this area is maximized when the source is right

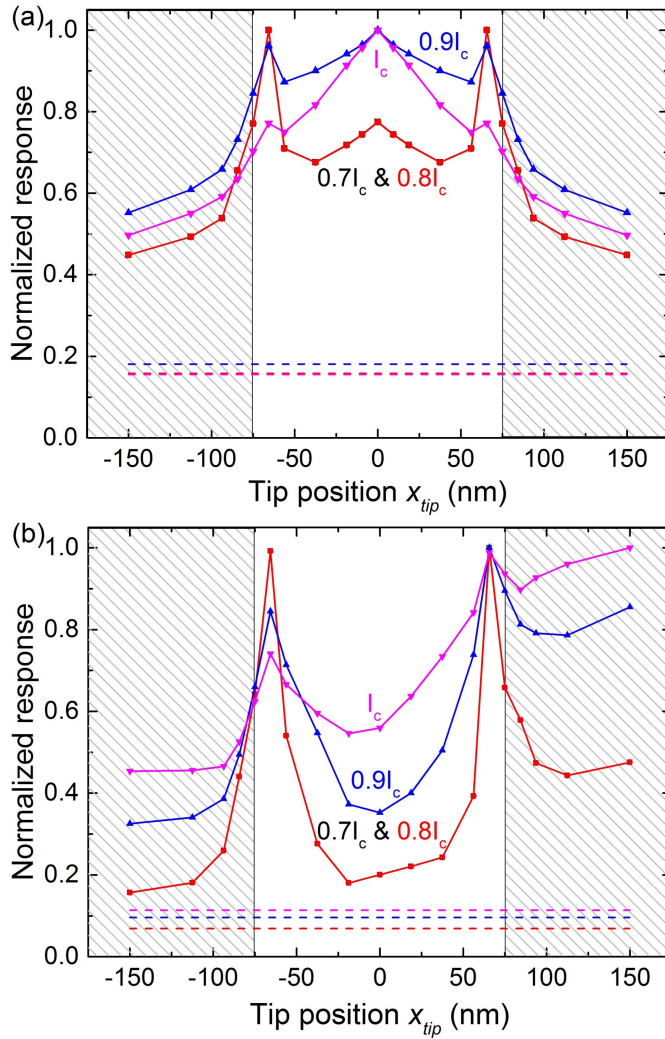


Figure 7.7: Detector response as a function of tip position  $x_{tip}$  for light incident from (a) the  $y$ -direction and (b) the  $x$ -direction. The unshaded area corresponds to the nanowire. The calculation uses the local detection efficiency  $LDE(x, I_b)$  in Fig. 7.6 at several bias currents. The dashed lines (background signal) are the detector response without tip in the system. Each curve is normalized to its maximum value to compare the shape of the response.

above the center of the detector. The maximum response, when the tip is at  $x_{tip} = \pm 65$  nm, is a tradeoff of these two factors with considering the very high detection efficiency close to the edges.

For higher bias currents ( $0.9I_c$  and  $I_c$ ), the contrast between the edge and the center of the nanowire becomes smaller. When the detector is biased at the critical current  $I_c$  the internal efficiency is uniform across the whole detector and the response curve (pink) in Fig. 7.7(a) at  $I_c$  reflects the optical absorption of the detector as a function of tip position.

For all the bias currents the detector response decreases as the tip position is far away from the nanowire. By moving the tip further away we expect the detector response to converge to the background level.

Figure 7.7(b) shows the detector response where the wave-vector of the incident light is along the  $x$ -axis, i.e., perpendicular to the nanowire. There are three differences from the data in Fig. 7.7(a): 1) The curves are asymmetric about the  $y$ -axis with the detector response becoming higher when the tip crosses the nanowire towards the positive  $x$ -axis. This is caused by reflected light, which leads to an increase in absorption or response as a function of tip position  $x$ . 2) At higher bias currents ( $0.9I_c$  and  $I_c$ ) the response with the tip above the edges is larger than that with the tip above the center of the wire despite the larger absorption area when  $x_{tip} = 0$  nm. Similarly to the parallel case, the absorption is localized within a narrow area when the tip is above the edges, but the field is more confined in the  $x$ -direction. As a result a larger response occurs when the tip is above the edges than when the tip is above the center. 3) Compared to the parallel case the contrast of the maximum and minimum value of the response is larger, and the half width of the peaks is narrower ( $\sim 20$  nm). As mentioned in the previous section, the local absorption response in the perpendicular case is similar to that of parallel case but is rotated  $90^\circ$  clockwise, see Fig. 7.5(a). Hence, when the tip scans over the edge of the nanowire, its localized electric field (with short axis of the absorption area along  $x$ -axis) moves from outside into the nanowire with a sharper transition, leading to the larger contrast and narrower response peaks.

In order to experimentally realize the proposed experiment, we discuss several nontrivial details. It is essential to remove the resist layer on top of the NbN nanowire that remains after detector fabrication. Preliminary results show that wet etching in a buffered HF solution can be used and that only  $\sim 6$  nm of HSQ (Hydrogen silsesquioxane) is left on a working NbN nanodetector. The roughness of the NbN plus remaining resist as measured by atomic force microscopy is 1.2 nm (FWHM) and is smaller than the gap of 5 nm and has minimal influence on the optical response.

For the sharp tip, we envisage a configuration similar to that reported in Ref. [44], where the gold tip is supported by a silicon pillar. Focused-Ion-Beam (FIB) milling allows fabrication of metal tips with lengths of 200 nm to several

tens of micrometers and a radius of curvature of 10 nm at the apex [44]. This tip needs to be illuminated from the side, which we believe can be done using an optical fiber with a graded-index lens which illuminates the detector at a grazing angle of incidence. A choice of a spot-size of 10–100  $\mu\text{m}$  covers the interesting tip-detector region. The mechanical stage needs to be carefully designed so that a difference in thermal expansion of different materials is compensated for. Ideally, the tip can be coarsely aligned to the detector at room temperature with the help of a CCD camera greatly reducing the problem of positioning the tip above the detector at cryogenic temperatures.

Finally, we note that current crowding effects are present in very short nanowires due to the tapered parts. We have calculated the current distribution in 150 nm wide NbN nanowires of different lengths. The difference in current density is less than 10% in the nanowire considered here and can be eliminated for nanowires longer than 500 nm.

## 7.6 Conclusions

We have numerically investigated a superconducting nanowire single-photon detector probed by a near-field, sharp gold tip, which is illuminated by a monochromatic light source. The tip above the detector functions as a nanoscale light source because of the localized electric field at the tip vertex. The tip behaves as a radiative electric dipole due to a surface plasmon resonance and a “lightning-rod” effect. For a wavelength of 1000 nm, the length of the tip is designed to be 200 nm to create significant resonant enhancement of the local electric field. The absorption of light by the detector is concentrated in an area of 50 nm around the tip, and it is not strongly influenced by the boundary of the wire.

According to a quasiparticle-diffusion and vortex-crossing model we predict that the intrinsic detector response is strongly enhanced near the edges of the nanowire for low bias currents. The detector response is calculated by taking into account this position-dependent local detection efficiency and the position dependence of optical absorption. At high bias currents close to the critical current the internal efficiency is constant and the response of the detector reflects the optical absorption profile when scanning the tip. At lower currents the response curve contains direct information of the intrinsic probability as a function of position. The detection response as a function of tip position exhibits two peaks on the edge of the nanowire due to the distribution of both internal efficiency and optical absorption near the edges. Based on our numerical simulations we estimate that these features can be resolved with a resolution of  $\sim 20$  nm. The best resolution is obtained for light incident perpendicular to the wire.



# Bibliography

- [1] H. Hertz. Ueber den einfluss des ultravioletten lichtes auf die electriche entladung. *Annalen der Physik*, 267:983, 1887.
- [2] A. Einstein. On a heuristic point of view about the creation and conversion of light. *Ann. Phys. (Leipz.)*, 17:132, 1905.
- [3] R. H. Hadfield. Single-photon detectors for optical quantum information applications. *Nat. Photonics*, 3:696, 2009.
- [4] M. D. Eisaman, J. Fan, A. Migdall, and S. V. Polyakov. Invited review article: Single-photon sources and detectors. *Rev. Sci. Instrum.*, 82:071101, 2011.
- [5] C. J. Chunnillall, I. P. Degiovanni, S. Kuck, I. Muller, and A. G. Sinclair. Metrology of single-photon sources and detectors: a review. *Opt. Eng.*, 53:081910, 2014.
- [6] T. Isoshima, Y. Isojima, K. Kikuchi, K. Nagai, and H. Nakagawa. Ultra-high sensitivity single photon detector using a silicon avalanche photodiode for the measurement of ultraweak biochemiluminescence. *Rev. Sci. Instr.*, 66:2922, 1995.
- [7] U. Lieberwirth, J. Arden-Jacob, K. H. Drexhage, D. P. Herten, R. Muller, M. Neumann, A. Schulz, S. Siebert, G. Sagner, S. Klingel, M. Sauer, and J. Wolfrum. Multiplex dye DNA sequencing in capillary gel electrophoresis by diode laser-based time-resolved fluorescence detection. *Anal. Chem.*, 70:4771, 1998.
- [8] A. Peacock, P. Verhoeve, N. Rando, A. van Dordrecht, B. G. Taylor, C. Erd, M. A.C. Perryman, R. Venn, J. Howlett, D. J. Goldie, J. Lumley, and M. Wallis. Single optical photon detection with a superconducting tunnel junction. *Nature*, 381:135, 1996.
- [9] C. B. McKitterick, D. E. Prober, and B. S. Karasik. Performance of graphene thermal photon detectors. *J. Appl. Phys.*, 113:044512, 2013.

- [10] A. D. Mora, A. Tosi, F. Zappa, S. Cova, D. Contini, A. Pifferi, L. Spinelli, A. Torricelli, and R. Cubeddu. Fast-gated single-photon avalanche diode for wide dynamic range near infrared spectroscopy. *IEEE J Sel Top Quantum Electron*, 16:1023, 2010.
- [11] N. Gisin, G. Ribordy, W. Tittel, and H. Zbinden. Quantum cryptography. *Rev. Mod. Phys.*, 74:145, 2002.
- [12] D. Stucki, S. Burri, E. Charbon, C. Chunnillall, A. Meneghetti, and F. Regazzoni. Towards a high-speed quantum random number generator. *Proc. SPIE*, 88990:88990R, 2013.
- [13] C. Silberhorn. Detecting quantum light. *Contemp. Phys.*, 48:147, 2007.
- [14] G. N. Gol'tsman, O. Okunev, G. Chulkova, A. Lipatov, A. Semenov, K. Smirnov, B. Voronov, A. Dzardanov, C. Williams, and R. Sobolewski. Picosecond superconducting single-photon optical detector. *Appl. Phys. Lett.*, 79:705, 2001.
- [15] T. Yamashita, S. Miki, K. Makise, W. Qiu, H. Terai, M. Fujiwara, M. Sasaki, and Z. Wang. Origin of intrinsic dark count in superconducting nanowire single-photon detectors. *Appl. Phys. Lett.*, 99:161105, 2011.
- [16] A. Pearlman, A. Cros, W. Slysz, J. Zhang, A. Verevkin, M. Currie, A. Korneev, P. Kouminov, K. Smirnov, B. Voronov, G. Gol'tsman, and R. Sobolewski. Gigahertz counting rates of nbn single-photon detectors for quantum communications. *IEEE Trans. Appl. Supercond.*, 15:579, 2005.
- [17] F. Marsili, V. B. Verma, J. A. Stern, S. Harrington, A. E. Lita, T. Gerrits, I. Vayshenker, B. Baek, M. D. Shaw, R. P. Mirin, and S. W. Nam. Detecting single infrared photons with 93% system efficiency. *Nat. Photonics*, 7:210, 2013.
- [18] F. Marsili, F. Najafi, E. Dauler, F. Bellei, X. Hu, M. Csete, R. J. Molnar, and K. K. Berggren. Single-photon detectors based on ultranarrow superconducting nanowires. *Nano Lett.*, 11:2048, 2011.
- [19] A. Divochiy, F. Marsili, D. Bitauld, A. Gaggero, R. Leoni, F. Mattioli, A. Korneev, V. Seleznev, N. Kaurova, O. Minaeva, K. G Lagoudakis, G. Gol'Tsman, M. Benkhaoul, F. Levy, and A. Fiore. Superconducting nanowire photon-number-resolving detector at telecommunication wavelengths. *Nat. Photonics*, 2:302, 2008.

- [20] R. H. Hadfield and N. Gemmell. Single photon imaging with superconducting nanowire single photon detectors. In *SPIE Optics + Optoelectronics, Prague*, number 9504-6, Prague, Czech, 2015. SPIE.
- [21] S. Miki, T. Yamashita, Z. Wang, and H. Terai. 64-pixel NbTiN superconducting nanowire single-photon detector array for spatially resolved photon detection. *Opt. Express*, 22:7811, 2014.
- [22] A. D. Semenov, G. Gol'tsman, and A. A. Korneev. Quantum detection by current carrying superconducting film. *Physica C*, 351:349, 2001.
- [23] L. Bulaevskii, M. Graf, C. Batista, and V. Kogan. Vortex-induced dissipation in narrow current-biased thin-film superconducting strips. *Phys. Rev. B*, 83:144526, 2011.
- [24] A. Engel and A. Schilling. Numerical analysis of detection-mechanism models of superconducting nanowire single-photon detector. *J. Appl. Phys.*, 114:214501, 2013.
- [25] A. Engel, J. Lonsky, X. Zhang, and A. Schilling. Detection mechanism in SNSPD: Numerical results of a conceptually simple, yet powerful detection model. *IEEE Trans. Appl. Supercond.*, 25:2200407, 2015.
- [26] H. L. Hortensius, E. F. C. Driessen, T. M. Klapwijk, K. K. Berggren, and J. R. Clem. Critical-current reduction in thin superconducting wires due to current crowding. *Appl. Phys. Lett.*, 100:182602, 2012.
- [27] R. Gaudio, K.M.P. op't Hoog, Z. Zhou, D. Sahin, and A. Fiore. Inhomogeneous critical current in nanowire superconducting single-photon detectors. *Appl. Phys. Lett.*, 105:222602, 2014.
- [28] J. S. Lundeen, A. Feito, H. Coldenstrodt-Ronge, K. L. Pregnell, Ch. Silberhorn, T. C. Ralph, J. Eiser, M. B. Plenio, and I. A. Walmsley. Tomography of quantum detectors. *Nat. Phys.*, 5:27, 2009.
- [29] J. J. Renema, G. Frucci, Z. Zhou, F. Mattioli, A. Gaggero, R. Leoni, M. J. A. de Dood, A. Fiore, and M. P. van Exter. Modified detector tomography technique applied to a superconducting multiphoton nanodetector. *Opt. Express*, 20:2806, 2012.
- [30] J. J. Renema, R. Gaudio, Q. Wang, Z. Zhou, A. Gaggero, F. Mattioli, R. Leoni, D. Sahin, M. J. A. de Dood, A. Fiore, and M. P. van Exter. Experimental test of theories of the detection mechanism in a nanowire superconducting single photon detector. *Phys. Rev. Lett.*, 112:117604, 2014.

- [31] H. C. van de Hulst. *Light Scattering by Small Particles*. Dover Publications, Amsterdam, 1981.
- [32] Q. Wang and M. J. A. de Dood. An absorption-based superconducting nano-detector as a near-field optical probe. *Opt. Express*, 21:3682, 2013.
- [33] A. J. Kerman, E. A. Dauler, W. E. Keicher, J. K. W. Yang, K. K. Berggren, G. Gol'tsman, and B. Voronov. Kinetic-inductance-limited reset time of superconducting nanowire photon counters. *Appl. Phys. Lett.*, 88:111116, 2006.
- [34] A. Feito, J. S. Lundeen, H. Coldenstrodt-Ronge, J. Eisert, M. B. Plenio, and I. A. Walmsley. Measuring measurement: theory and practice. *New J. Phys.*, 11:093038, 2009.
- [35] J. J. Renema, Q. Wang, R. Gaudio, I. Komen, K. op' Hoog, D. Sahin, A. Schilling, M. P. van Exter, A. Fiore, A. Engel, and M. J. A. de Dood. Position-dependent local detection efficiency in a nanowire superconducting single-photon detector. *Nano Lett.*, 15:4541, 2015.
- [36] M. K. Akhlaghi, A. H. Majedi, and J. S. Lundeen. Nonlinearity in single photon detection : modeling and quantum tomography. *Opt. Express*, 19:21305, 2011.
- [37] C. M. Natarajan, L. Zhang, H. Coldenstrodt-Ronge, G. Donati, S. N. Dorenbos, V. Zwiller, I. A. Walmsley, and R. H. Hadfield. Quantum detector tomography of a time-multiplexed superconducting nanowire single-photon detector at telecom wavelengths. *Opt. Express*, 21:893, 2013.
- [38] J. J. Renema, G. Frucci, Z. Zhou, F. Mattioli, A. Gaggero, R. Leoni, M. J. A. de Dood, A. Fiore, and M. P. van Exter. Universal response curve for nanowire superconducting single-photon detectors. *Phys. Rev. B*, 87:174526, 2013.
- [39] L. Maingaultg, M. Tarkhovg, I. Floryag, A. Semenovg, R. Espiau de Lamastreg, P. Cavalierg, G. Gol'tsmang, J.-P. Poizat, and J.-C. Villegier. Spectral dependency of superconducting single photon detectors. *J. Appl. Phys.*, 107:116103, 2010.
- [40] R. Lusche, A. Semenovg, K. Iling, M. Siegelg, Y. Korneevag, A. Trifonovg, A. Korneevg, G. Goltsmang, D. Vodolazov, and H.-W. Hubers. Effect of the wire width on the intrinsic detection efficiency of superconducting-nanowire single-photon detectors. *J. Appl. Phys.*, 116:043906, 2014.

- [41] J. R. Clem and K. K. Berggren. Geometry-dependent critical currents in superconducting nanocircuits. *Phys. Rev. B*, 84:174510, 2011.
- [42] V. Anant, A. J. Kerman, E. A. Dauler, J. K. W. Yang, K. M. Rosfjord, and K. K. Berggren. Optical properties of superconducting nanowire single-photon detectors. *Opt. Express*, 16:10750, 2008.
- [43] M. Burreli, D. van Oosten, T. Kampfrath, H. Schoenmaker, R. Heide-  
man, A. Leinse, and L. Kuipers. Mapping local charge recombination  
heterogeneity by multidimensional nanospectroscopic imaging. *Science*,  
23:5952, 2009.
- [44] F. Huth, A. Chuvilin, M. Schnell, I. Amenabar, R. Krutokhvostov,  
S. Lopatin, and R. Hillenbrand. Resonant antenna probes for tip-  
enhanced infrared near-field microscopy. *Nano Lett.*, 13:1065, 2013.
- [45] N. Rotenberg and L. Kuipers. Mapping nanoscale light fields. *Nat.*  
*Photonics*, 8:919, 2014.
- [46] C. H. Henry and R. F. Kazarinov. Quantum noise in photonics. *Rev.*  
*Mod. Phys.*, 68:801, 1996.
- [47] E. F. C. Driessen and M. J. A. de Dood. The perfect absorber. *Appl.*  
*Phys. Lett.*, 94:171109, 2009.
- [48] L. Novotny, R. X. Bian, and X. Xie. Theory of nanometric optical twee-  
zers. *Phys. Rev. Lett.*, 79:645, 1997.
- [49] J. I. Gersten. The effect of surface-roughness on surface enhanced raman  
scattering. *J. Chem. Phys.*, 72:5779, 1980.
- [50] H. Takesue, S. W. Nam, Q. Zhang, R. H. Hadfield, T. Honjo, K. Tamaki,  
and Y. Yamamoto. Quantum key distribution over a 40-db channel loss  
using superconducting single-photon detectors. *Nat. Photonics*, 1:343,  
2007.
- [51] A. Luis and L. L. Sanchez-Soto. Complete characterization of arbitrary  
quantum measurement processes. *Phys. Rev. Lett.*, 83:3573, 1999.
- [52] D. Mogilevtsev Z. Hradil and J. Řeháček. Biased tomography schemes:  
an objective approach. *Phys. Rev. Lett.*, 96:230401, 2006.
- [53] G. Brida, L. Ciavarella, I. P. Degiovanni, M. Genovese, L. Lolli, M. G.  
Mingolla, F. Piacentini, M. Rajteri, E. Taralli, and M. G A Paris. Quan-  
tum characterization of superconducting photon counters. *New J. Phys*,  
14:085001, 2012.

- [54] I. Muller, R. M. Klein, and L. Werner. Traceable calibration of a fibre-coupled superconducting nano-wire single photon detector using characterized synchrotron radiation. *Metrologia*, 51:S329, 2014.
- [55] K. Burnham and D. Anderson. *Model selection and multimodel inference- A Practical Information-Theoretic Approach*. Springer, New York, 1998.
- [56] A. Migdall et al. *Single-Photon Generation and Detection: Physics and Applications*. Academic Press, Oxford, 2013.
- [57] J. J. Renema. *The physics of nanowire superconducting single-photon detectors*. PhD thesis, Leiden University, Leiden, The Netherlands, 2015.
- [58] F. Marsili, M. J. Stevens, A. Kozorezov, V. B. Verma, C. Lambert, J. A. Stern, R. Horansky, M. D. Shaw S. D. Dyer, R. P. Mirin, and S. W. Nam. Hotspot relaxation dynamics in a current carrying superconductor. arXiv:1506.03129, 2015.
- [59] Gentec. Ph20-ge. <https://www.gentec-eo.com>.
- [60] L. N. Bulaevskii, M. J. Graf, and V. G. Kogan. Vortex-assisted photon counts and their magnetic field dependence in single-photon superconducting detectors. *Phys. Rev. B*, 85:014505, 2012.
- [61] C. Natarajan, M. Tanner, and R. Hadfield. Superconducting nanowire single-photon detectors: physics and applications. *Supercond. Sci. Technol*, 25:063001, 2012.
- [62] D. M. Boroson, J. J. Scozzafava, D. V. Murphy, B. S. Robinson, and H. Shaw. The lunar laser communications demonstration. In *Third IEEE International Conference on Space Mission Challenges for Information Technology*, volume Space Mission Challenges for Information Technology, California, USA, 2009. IEEE.
- [63] N. Gemmell, A. McCarthy, B. Liu, M. Tanner, S. Dorenbos, V. Zwiller, M. Patterson, G. Buller, B. Wilson, and R. H. Hadfield. Singlet oxygen luminescence detection with a fiber-coupled superconducting nanowire single-photon detector. *Opt. Express*, 21:5005, 2013.
- [64] D. Bitauld, F. Marsili, A. Gaggero, F. Mattioli, R. Leoni, S. Jahanmirinejad, F. Levy, and A. Fiore. Nanoscale optical detector with single-photon and multiphoton sensitivity. *Nano Lett.*, 10:2977, 2010.
- [65] E. F. C. Driessen, F. Braakman, E. Reiger, S. Dorenbos, V. Zwiller, and M. J. A. de Dood. Impedance model for the polarization-dependent optical absorption of superconducting single-photon detectors. *Eur. Phys. J. Appl. Phys.*, 47:10701, 2009.

- [66] V. Verma, F. Marsili, S. Harrington, A. Lita, R. Mirin, and S. Nam. A three-dimensional, polarization-insensitive superconducting nanowire avalanche photodetector. *Appl. Phys. Lett.*, 101:251114, 2012.
- [67] T. Yamashita, S. Miki, H. Terai, and Z. Wang. Low-filling-factor superconducting single photon detector with high system detection efficiency. *Opt. Express*, 22:27177, 2013.
- [68] M. K. Akhlaghi and A. H. Majedi. Semiempirical modeling of dark count rate and quantum efficiency of superconducting nanowire single-photon detectors. *IEEE Trans. Appl. Supercond.*, 19:361, 2009.
- [69] H. B. Coldenstrodt-Ronge, J. S. Lundeen, K. L. Pregnell, A. Feito, B. J. Smith, W. Mauerer, C. Silberhorn, J. Eisert, M. B. Plenio, and I. A. Walmsley. A proposed testbed for detector tomography. *J. Mod. Optic.*, 56:432, 2009.
- [70] J. J. Renema, G. Frucci, M. J. A. de Dood, R. Gill, A. Fiore, and M. P. van Exter. Tomography and state reconstruction with superconducting single-photon detectors. *Phys. Rev. A*, 86:062113, 2012.
- [71] RSoft. <http://optics.synopsys.com/rssoft/>.
- [72] D. Sahin. *Waveguide single-photon and photon-number resolving detectors*. PhD thesis, Eindhoven University of Technology, Eindhoven, The Netherlands, 2014.
- [73] M. Tinkham. *Introduction to superconductivity*. McGraw-Hill, New York, 2nd edition, 1996.
- [74] A. Semenov, A. Engel, H.-W. Hubers, K. Il'in, and M. Siegel. Spectral cut-off in the efficiency of the resistive state formation caused by absorption of a single-photon in current-carrying superconducting nano-strips. *Euro. Phys. J. B*, 47:495, 2005.
- [75] A. N. Tikhonov. *On the stability of inverse problems*, volume 39. Dokl. Akad. Nauk SSSR, 1943.
- [76] R. Ikuta, H. Kato, Y. Kusaka, S. Miki, T. Yamashita, H. Terai, M. Fujiwara, T. Yamamoto, M. Koashi, M. Sasaki, Z. Wang, and N. Imoto. High-fidelity conversion of photonic quantum information to telecommunication wavelength with superconducting single-photon detectors. *Phys. Rev. A*, 87:010301(R), 2013.
- [77] M. Sasaki, M. Fujiwara, H. Ishizuka, W. Klaus, K. Wakui, M. Takeoka, S. Miki, T. Yamashita, Z. Wang, A. Tanaka, K. Yoshino, Y. Nambu,

- S. Takahashi, A. Tajima, A. Tomita, T. Domeki, T. Hasegawa, Y. Sakai, H. Kobayashi, T. Asai, K. Shimizu, T. Tokura, T. Tsurumaru, M. Matsui, T. Honjo, K. Tamaki, H. Takesue, Y. Tokura, J. F. Dynes, A. R. Dixon, A. W. Sharpe, Z. L. Yuan, A. J. Shields, S. Uchikoga, M. Legre, S. Robyr, P. Trinkler, L. Monat, J.-B. Page, G. Ribordy, A. Poppe, A. Allacher, O. Maurhart, T. Langer, M. Peev, and A. Zeilinger. Field test of quantum key distribution in the Tokyo QKD Network. *Opt. Express*, 19:10387, 2011.
- [78] K. M. Rosfjord, J. K. W. Yang, E. A. Dauler, A. J. Kerman, V. Anant, B. M. Voronov, G. N. Gol'tsman, and K. K. Berggren. Nanowire single-photon detector with an integrated optical cavity and anti-reflection coating. *Opt. Express*, 14:527, 206.
- [79] J. D. Jackson. *Classical Electrodynamics*. Wiley & Sons, New York, 1983.
- [80] R. C. Dunn. Near-field scanning optical microscopy. *Chem. Rev.*, 99:2891, 1999.
- [81] K. Busch, S. Lölkes, R. B. Wehrspohn, and H. Föll. *Photonic Crystals: Advances in Design, Fabrication, and Characterization*. Wiley-VCH Verlag GmbH & Co. KGaA, Weinheim, 2006.
- [82] F. Keilmann and R. Hillenbrand. Near-field microscopy by elastic light scattering from a tip. *Phil. Trans. R. Soc. Lond. A.*, 362:787, 2004.
- [83] T. Kalkbrenner, M. Ramstein, J. Mlynek, and V. Sandoghdar. A single gold particle as a probe for apertureless scanning near-field optical microscopy. *J. Microsc.*, 202:72, 2001.
- [84] B. Hecht, U. P. Wild B. Sick, V. Decker, R. Zenobi, O. J. F. Martin, and D. W. Pohl. Scanning near-field optical microscopy with aperture probes: fundamentals and applications. *J. Chem. Phys.*, 112:7761, 2000.
- [85] E. Betzig and R. J. Chichester. Single molecules observed by near-field scanning optical microscopy. *Science*, 262:1422, 1993.
- [86] A. Rasmussen and V. Deckert. New dimension in nano-imaging: breaking through the diffraction limit with scanning near-field optical microscopy. *Anal. Bioanal. Chem.*, 381:165, 2005.
- [87] F. Zenhausern, M. P. O'Boyle, and H. K. Wickramasinghe. Apertureless near-field optical microscope. *Appl. Phys. Lett.*, 65:1623, 1994.
- [88] A. V. Zayats and V. Sandoghdar. Apertureless near-field optical microscopy via local second-harmonic generation. *J. Microsc.*, 202:94, 2001.

- [89] T. Vo-Dinh, J. P. Alarie, B. M. Cullum, and G. D. Griffin. Antibody-based nanoprobe for measurement of a fluorescent analyte in a single cell. *Nat. Biotechnol.*, 18:764, 2000.
- [90] Y. Zhang, A. Dhawan, and T. Vo-Dinh. Design and fabrication of fiber-optic nanoprobes for optical sensing. *Nanoscale Res Lett.*, 6:18, 2011.
- [91] J. Smajic and C. Hafner. Numerical analysis of a SNOM tip based on a partially cladded optical fiber. *Opt. Express*, 19:23140, 2011.
- [92] H. A. Bethe. Theory of diffraction by small holes. *Phys. Rev.*, 66:163, 1944.
- [93] I. S. Averbukh, B. M. Chernobrod, O. A. Sedletsy, and Y. Prior. Coherent near field optical microscopy. *Opt. Commun.*, 174:33, 2000.
- [94] B. Knoll and F. Keilmann. Enhanced dielectric contrast in scattering-type scanning near-field optical microscopy. *Opt. Commun.*, 182:321, 2000.
- [95] C. F. Bohren and D. R. Huffman. *Absorption and scattering of light by small particles*. Wiley & Sons, New York, 1983.
- [96] E. D. Palik. *Handbook of Optical Constants of Solids I*. Academic, San Diego, 1998.
- [97] M. Esslinger and R. Vogelgesang. Reciprocity theory of apertureless scanning near-field optical microscopy with point-dipole probes. *ACS Nano*, 6:8173, 2012.
- [98] A. J. L. Adam, N. C. J. van der Valk, and P. C. M. Planken. Measurement and calculation of the near field of a terahertz apertureless scanning optical microscope. *J. Opt. Soc. Am. B*, 24:1080, 2007.
- [99] L. Novotny and B. Hecht. *Principles of Nano-optics*. Cambridge University Press, New York, 2006.
- [100] K. H. Drexhage. Influence of a dielectric interface on fluorescence decay time. *J. Luminescence*, 1,2:693, 1970.
- [101] K. H. Drexhage. Interaction of light with monomolecular dye layers. *Prog. Optics*, 12:165, 1974.
- [102] R. R. Chance, A. Prock, and R. Silbey. Molecular fluorescence and energy transfer near interfaces. *Adv. Chem. Phys.*, 37:1, 1978.

- [103] K. Joulain, R. Carminati, J. Mulet, and J. Greffet. Definition and measurement of the local density of electromagnetic states close to an interface. *Phys. Rev. B*, 68:245405, 2003.
- [104] K. Tanabe, H. Asano, Y. Katoh, and O. Michikami. Ellipsometric and optical reflectivity studies of reactively sputtered NbN thin films. *J. Appl. Phys.*, 63:1733, 1988.
- [105] D. A. Bonnell, D. N. Basov, M. Bode, U. Diebold, S. V. Kalinin, V. Madhavan, L. Novotny, M. Salmeron, U. D. Schwarz, and P. S. Weiss. Imaging physical phenomena with local probes: From electron to photons. *Rev. Mod. Phys.*, 84:1343, 2012.
- [106] A. D. Rakic, A. B. Djuricic, J. M. Elazar, and M. L. Majewski. Optical properties of metallic films for vertical-cavity optoelectronic devices. *Appl. Opt.*, 37:5271, 1998.
- [107] Y. C. Martin, H. F. Hamann, and H. L. Wickramasinghe. Strength of the electric field in apertureless near-field optical microscopy. *J. Appl. Phys.*, 89:5774, 2001.
- [108] A. Hartschuh, M. R. Beverluis, A. Bouhelier, and L. Novotny. Tip-enhanced optical spectroscopy. *Phil. Trans.R. Soc. Lond. A*, 362:807, 2004.
- [109] N. Behr and M. B. Raschke. Optical antenna properties of scanning probe tips: plasmonic light scattering, tip-sample coupling, and near-field enhancement. *J. Phys. Chem. C*, 112:3766, 2008.
- [110] A. Alu and N. Engheta. Input impedance, nanocircuit loading, and radiation tuning of optical nanoantennas. *Phys. Rev. Lett.*, 101:043901, 2008.
- [111] A. Alu and N. Engheta. Tuning the scattering response of optical nanoantennas with nanocircuit loads. *Nat. Photonics*, 2:307, 2008.
- [112] J. J. Bowman, T. B. A. Senior, and P. L. E. Uslenghi. *Electromagnetic and Acoustic Scattering by simple Shapes*. North-Holland, Amsterdam, 1969.
- [113] P. Anger, P. Bharadwaj, and L. Novotny. Enhancement and quenching of single-molecule fluorescence. *Phys. Rev. Lett.*, 96:113002(1), 2006.
- [114] R. B. G. de Hollander, N. F. van Hulst, and R. P. H. Kooyman. Near field plasmon and force microscopy. *Ultramicroscopy*, 57:263, 1995.

- [115] J. Chen, M. Badioli, P. Alonso-Gonzalez, S. Thongrattanasiri, F. Huth, J. Osmond, M. Spasenovic, A. Centeno, A. Pesquera, P. Godignon, A. Z. Elorza, N. Camara, F. Javier Garca de Abajo, R. Hillenbrand, and F. H. L. Koppens. Optical nano-imaging of gate-tunable graphene plasmons. *Nature*, 487:77, 2012.
- [116] R. H. Hadfield, P. A. Dalgarno, J. A. O'Connor, E. Ramsay, R. J. Warburton, E. J. Gansen, B. Baek, M. J. Stevens, R. P. Mirin, and S. W. Nam. Submicrometer photoresponse mapping of nanowire superconducting single-photon detectors. *Appl. Phys. Lett.*, 91:241108, 2007.
- [117] J. A. O'Connor, M. G. Tanner, C. M. Natarajan, G. S. Buller, R. J. Warburton, S. Miki, Z. Wang, S. W. Nam, and R. H. Hadfield. Spatial dependence of output pulse delay in a niobium nitride nanowire superconducting single-photon detector. *Appl. Phys. Lett.*, 98:201116, 2011.
- [118] D. Lim, K. Jeon, J. Hwang, H. Kim, Su. Kwon, Y. Suh, and J. Nam. Highly uniform and reproducible surface-enhanced raman scattering from DNA-tailorable nanoparticles with 1-nm interior gap. *Nat. Nano*, 6:452, 2011.
- [119] R. W. Taylor, T. Lee, O. A. Scherman, R. Esteban, J. Aizpurua, F. Huang, J. J. Baumberg, and S. Mahajan. Precise subnanometer plasmonic junctions for sers within gold nanoparticle assemblies using cucurbit[n]uril 'glue'. *ACS Nano*, 5:3878, 2011.
- [120] R. Esteban, A. G. Borisov, P. Nordlander, and J. Aizpurua. Bridging quantum and classical plasmonics with a quantum-corrected model. *Nat. Commun.*, 3:825, 2012.
- [121] A. V. Goncharenko, M. M. Dvoynenko, H. Chang, and J. Wang. Electric field enhancement by a nanometer-scaled conical metal tip in the context of scattering-type near-field optical microscopy. *Appl. Phys. Lett.*, 88:104101, 2006.
- [122] Z. Yang, J. Aizpurua, and H. Xu. Electromagnetic field enhancement in TERS configurations. *J. Raman Spectrosc.*, 40:1343, 2009.
- [123] Q. Wang and M. J. A. de Dood. Near-field single-photon detection in a scattering SNOM. In *SPIE Optics + Optoelectronics, Prague*, number 9504-2, Prague, Czech, 2015. SPIE.
- [124] R. Hillenbrand, B. Knoll, and F. Keilmann. Pure optical contrast in scattering-type scanning near-field microscopy. *J. Microsc.*, 202:77, 2001.

- [125] T. Taubner, R. Hillenbrand, and F. Keilmann. Performance of visible and mid-infrared scattering-type near-field optical microscopes. *J. Microsc.*, 210:311, 2003.

# Summary

Light is one of the tools by which humans understand the world and nature surrounding them. For instance, what we see with our eyes is the scattered or reflected light from objects, which provides us with necessary information in daily life. Much of the understanding of the world around us can be gathered by using the classical description of light as an electromagnetic wave.

Light is also one of the tools in pioneering scientific research by which insight and understanding is obtained at a deeper level. Besides the classical behavior of light as a wave, light also shows features of a particle, usually called a photon. This particle description is essential for modern topics such as quantum optics and quantum information. Whatever description is applicable, ultimately the light will interact with a material object, be it the eye, a camera or a single-photon detector and the nature of this interaction is a research topic by itself. This thesis focusses on understanding light-matter interaction for nanoscale objects with a strong emphasis on superconducting nanowires capable of detecting single photons.

Superconductivity is a phenomenon where materials exhibit exactly zero electrical resistance when cooled below their characteristic critical temperature, provided that the current through the material does not exceed the critical current. The superconductor material in this thesis is NbN, which becomes superconducting for temperatures below 10 K. The NbN material is shaped as a single nanowire on a substrate, and a current just below the critical current is applied. Under these conditions absorption of the energy of a single photon is sufficient to drive the nanowire from the superconducting state to the normal state. Once the wire is in the normal, resistive state a voltage pulse is generated and amplified that signifies the detection of the triggering single photon. For lower bias currents multiple photons are needed to trigger the nanowire.

The typical dimensions of the nanowires studied in this thesis are 50-200 nm wide and  $\sim 5$  nm thick, being 5-20 times narrower and 200 times thinner than the wavelength of light. While the wave description of light provides an adequate description of light absorption for nanoscale objects the physical processes that take place on the nanoscale require further investigation. A direct observation of such a nanoscale light-matter interaction requires focusing light

to length scales smaller than the width of the nanowire, far below the diffraction limit. To gain access to these length scales scanning near-field optical microscopy (SNOM) techniques are necessary. Conventional SNOMs use a sharp metal tip or a subwavelength aperture to concentrate the light that is subsequently scattered to a far-field detector. The efficiency of such a SNOM is limited because the amount of light scattered from objects much smaller than the wavelength is exceedingly small.

The low efficiency of SNOMs makes it difficult to use them to explore physical phenomena at the single photon level. An idea, put forward in this thesis, is to use the NbN nanodetector to detect light directly in the near-field. Compared to a conventional SNOM, this configuration uses the much more efficient process of nanoscale absorption that scales with the volume of the nanoparticle. A NbN superconducting single photon detector can be small and can be integrated on top of a nanofabricated pyramid or pillar to create a scanning, single-photon sensitive probe. In this way a multi-photon probe with deep subwavelength resolution can be achieved. Based on the numerical simulations in Chapter 5 we estimate that a  $50 \times 50$  nm sized NbN detector can be used as a near-field scanning probe that is two orders of magnitude more sensitive than a conventional, aperture based probe. This high efficiency hints at a strong near-field light-matter interaction. However, the perturbation of the emission rate of a nearby quantum dot is smaller than with conventional SNOM probes.

New experiments that aim at investigating the detection mechanism of SSPDs can be designed by using the technique of quantum detector tomography. Most measurements that characterize SSPDs measure the count rate as a function of the power of the light incident on the detector and bias current applied to the detector. Detector tomography uses the measured count rate as a function of the mean photon number of the incident light to determine the absorption efficiency and the probabilities to detect exactly one, two, three etc. photons. The description of the detector response in this photon number basis is a complete quantum description of the detector and is an essential step in understanding the detection mechanism of SSPDs. The accuracy and robustness of this type of tomography is investigated in Chapter 2, showing that the parameters that characterize the quantum response of the detector can be estimated to an accuracy better than 2%.

Detector tomography separates the physical process of optical absorption from the process that leads to a measurable voltage pulse. The physics of this latter process is still under active investigation, but should not depend on the polarization of the incident light: once the photon is absorbed the energy is transferred to the electrons of the superconductor and the polarization information is lost. Surprisingly, our tomography experiments show that the probabilities to detect one photon after the absorption efficiency is factored

out **do** depend on the polarization of the incident light.

Repeating the polarization-dependent tomography experiment for various wavelengths and combining this information with the numerically calculated polarization and position dependent absorption of the wire allows us to recover the position-dependent internal detection efficiency of a single nanowire. The result shows that the edges of the wire are more photo-sensitive than the center. This qualitatively agrees with models of the detection process that include the effect of photon-assisted vortex entry. In these models photon detection at the edge is favored because absorption of the photon lowers the energy barrier for vortex entry. Once the vortex enters the superconducting material the dissipation of the moving vortex triggers the detector.

The experimentally determined local detection efficiency of a nanowire cannot be completely explained by the current models. However, good quantitative agreement with the measured polarization-dependent quantum efficiency of meandering wire SSPDs can be obtained if both the polarization-dependent optical absorption and the measured local detection efficiency is taken into account. This strengthens the emerging picture of a local detection efficiency for NbN detectors, but a direct experimental observation is still lacking.

As a first step towards a direct determination of the local detection efficiency we have numerically simulated the response of a NbN nanowire in a scattering SNOM using the local detection efficiency as input. In these simulations, a rounded, conical tip is placed above a NbN nanowire, with a fixed gap of 5 nm between the tip and the nanowire. The tip-nanowire system is illuminated from the side and the tip functions as an antenna that concentrates the light around its apex. In such a configuration the tip acts as a point-like light source scanning over the nanowire, and the tip-position dependent SSPD response is calculated. Because the absorbing detector functions as a resistive load to the antenna a question arises if the resonance required for a subwavelength resolution probe is degraded by the presence of the tip.

The simulation results show that, besides the intrinsic property of the position-dependent detection efficiency, the detector response in the SNOM also depends on the tip geometry and tip position. The localization of the incident light around the tip originates from the coupling of the light and the free electrons in the tip. Thus, the tip geometry plays an important role in the SSPD absorption. The tip with a smaller semi-angle and radius produces a higher free electron density and consequently a stronger electric field (or light) intensity at its apex. As a result more absorption occurs in the detector. The length of the tip determines the plasmonic response of the electrons in the metal tip, and the intensity of the light in between the apex and the detector shows a resonant behavior as a function of the tip length. A spatial resolution of  $\sim 20$  nm can be achieved when the tip moves across the edge of the nanowire where the signal is enhanced by a maximum in both the local

detection efficiency and the optical absorption of the tip-nanowire geometry.

With both photon number resolving ability and high spatial resolution of 20 nm, new types of near-field optical microscopy arise. A nanowire SSPD can be fabricated on top of a micrometer-sized pyramid or pillar, and the edge can be used as a sensor in near-field detection, with a spatial resolution of about 20 nm. By tuning the bias current we can make the detector work in different photon-number regimes, opening the possibility to extract quantum information (i.e., photon number states) in the optical near-field.

# Samenvatting

Licht stelt ons in staat om de wereld en de natuur om ons heen waar te kunnen nemen zodat we hiervan kunnen genieten en de door het licht gedragen informatie in het dagelijks leven kunnen gebruiken. Wat we met onze ogen waarnemen is het verstrooide of gereflecteerde licht van de voorwerpen. Voor het begrip van het alledaagse verschijnsel licht is een beschrijving van licht als een elektromagnetische golf afdoende.

In veel wetenschappelijk onderzoek wordt gebruik gemaakt van licht; het is in veel gevallen het gereedschap waarmee inzicht in en begrip van materie op zeer kleine schaal en/of een dieper niveau wordt verkregen. Naast het klassieke gedrag van licht als een golf vertoont het ook kenmerken die wij normaal toeschrijven aan een deeltje. Deze lichtdeeltjes worden fotonen genoemd. Deze beschrijving van licht is van essentieel belang bij onderzoek op het gebied van de kwantum optica en kwantum informatie. In dit proefschrift worden zowel de golf- als de deeltjesbeschrijving toegepast.

Ongeacht de beschrijving zal het licht wisselwerken met een voorwerp, hetzij het oog, een camera of een enkel-foton detector. Het begrijpen van deze wisselwerking is al vele jaren een onderwerp van wetenschappelijk onderzoek. Het onderzoek dat in dit proefschrift wordt beschreven heeft dit als thema met een sterke nadruk op de wisselwerking van één, twee, of meerdere fotonen met een supergeleidende nanodraad als microscopische detector.

Supergeleiding is een verschijnsel waarbij de elektrische weerstand van een materiaal volledig verdwijnt wanneer het wordt afgekoeld tot vlak bij het absolute nulpunt. Het materiaal dat in dit proefschrift wordt bestudeerd is Niobium Nitride (NbN) dat in de vorm van nanodraden op een oppervlak is neergelegd. Bij een temperatuur beneden de 10 K worden deze draden supergeleidend. De afmetingen van de draad en de stroom door de draad zijn zodanig gekozen dat de energie van één enkel foton voldoende is om de draad te schakelen van de supergeleidende naar de normale toestand. De elektrische weerstand in de normale toestand zorgt vervolgens voor een spanningsval die kan worden versterkt en vastgelegd. Een bijzondere eigenschap van deze nanodraden is dat de spanningsval ook bij lagere waarden van de stroom kan worden waargenomen. Dit wordt veroorzaakt door twee of meer fotonen die tegelijk worden geabsorbeerd

door de draad.

De nanodraden in mijn onderzoek zijn typisch 50–200 nm breed en 5 nm dik. Dat is 5–20 keer smaller en 200 keer dunner dan de golflengte van het licht dat ik gebruik. De beschrijving van licht als een golf volstaat om de absorptie van licht door de nanodraad te begrijpen. Wat gebeurt er daarna precies? Nader onderzoek is nodig om ook de fysische processen te begrijpen die leiden tot het schakelen van de draad. Nabije-veld microscopie is onontbeerlijk in dit onderzoek omdat met deze techniek licht kan worden gebundeld op een lengteschaal die veel kleiner is dan de golflengte van het licht. Nabije-veld microscopen gebruiken een scherpe metalen punt of een gat in een dunne laag metaal om licht op een oppervlak af te tasten. In beide gevallen wordt er licht verstrooid naar een foton-gevoelige detector. Het te meten signaal is echter verwaarloosbaar klein, omdat het fysische proces van lichtverstrooiing bijzonder inefficiënt is voor voorwerpen die veel kleiner zijn dan de golflengte van het licht.

Deze inherent lage efficiëntie maakt nabije veld microscopie met één enkel foton nagenoeg onmogelijk. In dit proefschrift wordt een nieuwe methode beschreven waarbij een NbN nanodetector wordt gebruikt als sonde in het nabije veld. Deze methode profiteert van het feit dat voor zeer kleine deeltjes de kans op absorptie van licht vele malen groter is dan de kans op verstrooiing. Op basis van de numerieke simulaties in hoofdstuk 5 schatten we dat een NbN detector van  $50 \times 50 \text{ nm}^2$  kan worden gebruikt als een sonde die 100 keer gevoeliger is dan een vergelijkbare sonde die gebruikt maakt van lichtverstrooiing. Tegelijkertijd is de versturende werking op de optische vervalstijd van een nabijgelegen kwantum dot veel kleiner.

Het onderliggende detectie mechanisme van een supergeleidende enkel-foton detector kan worden onderzocht met behulp van kwantum detector tomografie. Deze methode telt het aantal detectie gebeurtenissen per seconde als functie van het gemiddeld aantal fotonen dat op de detector valt. Deze gegevens worden gebruikt om het absorptie-rendement, en de kans op detectie van exact één, twee, drie etc. fotonen te bepalen. De beschrijving in termen van het aantal fotonen is een essentiële stap in het begrip van het detectiemechanisme omdat dit inzicht geeft in de detectiekans als functie van de totale energie van de fotonen. De methode en de nauwkeurigheid worden nader onderzocht in hoofdstuk 2.

Detector tomografie scheidt de kans op optische absorptie van de kans om na absorptie een meetbare spanningspuls te genereren. De fysica van dit laatste proces kan natuurlijk niet afhankelijk zijn van de polarisatie van het al geabsorbeerde foton want die informatie is al verloren. Het is daarom verrassend dat onze tomografie experimenten duidelijk laten zien dat de kans op het genereren van een spanningspuls na optisch absorptie toch afhangt van de polarisatie van het invallende licht.

De verklaring voor deze waarnemingen wordt gegeven in de hoofdstukken 3 en 4 van dit proefschrift. Berekeningen laten zien dat de absorptiekans in de draad op een polarisatie gevoelige manier afhangt van de transversale positie op die draad. Als ook de kans dat het absorberen van een foton resulteert in een klik van de detector afhangt van de positie waar het foton is geabsorbeerd, dan geeft dit een polarisatie afhankelijke respons. Door kwantum-detector tomografie te doen voor verschillende golflengtes van het licht kunnen we de positie-afhankelijke interne detectie efficiëntie van de nanodraad bepalen. Hieruit blijkt dat de randen van de nanodraad beter als foton detector werken dan het midden van de draad. Dit resultaat is in goede overeenstemming met al bestaande fysische modellen van het detectie proces die de detectie verklaren met behulp van magnetische vortices in de supergeleider. Deze vortices worden tegengehouden door een potentiaal barrière aan de randen van de draad. Absorptie van een foton verlaagt de barrière waardoor de vortex de draad kan oversteken. Bij het oversteken van de vortex wordt arbeid verricht waardoor de supergeleidende nanodraad schakelt.

Een vergelijking met metingen van de polarisatie-afhankelijke kwantumefficiëntie van een detector bestaand uit een meanderende draad laat zien dat de door ons experimenteel bepaalde lokale detectie efficiëntie ook het gedrag van deze detectoren goed voorspelt. Echter, de huidige theoretische modellen voorspellen een te groot verschil tussen de respons van de randen en het midden van de draad. Om deze impasse te doorbreken is een directe waarneming van de lokale detectie-efficiëntie van een NbN detector nodig.

Als een eerste stap in deze richting worden in dit proefschrift realistische simulaties van nabije-veld microscopie aan een NbN nanodraad beschreven. In deze simulaties wordt een scherpe metalen punt gebruikt om het licht te concentreren op de NbN detector. De kegelvormige metalen punt wordt daarbij op een afstand van 5 nm boven de nanodraad geplaatst waarbij licht vanaf de zijkant op de metalen tip valt. De metalen tip werkt als antenne waarmee het licht wordt geconcentreerd op het uiteinde van de tip waarbij een resolutie kan worden bereikt van 20 nm. Met een dergelijke puntbron kan de detector worden afgetast op de nanoschaal.

Nieuwe toepassingen van nabije-veld microscopie komen met dit onderzoek binnen bereik. Een nano-detector geplaatst op een piramide of pilaar kan worden gebruikt als een nieuwe sonde voor nabije-veld microscopie. Door de stroom door de detector in te stellen wordt het mogelijk om nabije-veld microscopie op één, twee, drie etc. foton niveau te bedrijven.



# List of publications

- Scientific Articles

- Q. Wang, and M. J. A. de Dood, *An absorption-based superconducting nano-detector as a near-field optical probe*, Opt. Express **21**, 3682, (2013). (Chapter 5 of this thesis).
- J. J. Renema, R. Gaudio, Q. Wang, Z. Zhou, A. Gaggero, F. Mattioli, R. Leoni, D. Sahin, M. J. A. de Dood, A. Fiore, and M. P. van Exter, *Experimental test of theories of the detection mechanism in a nanowire superconducting single photon detector*, Phys. Rev. Lett. **112**, 117604, (2014).
- J. J. Renema, R. J. Rengelink, I. Komen, Q. Wang, R. Gaudio, K. P. M. op 't Hoog, Z. Zhou, D. Sahin, A. Fiore, P. Kes J. Aarts, M. P. van Exter, M. J. A. de Dood, E. F. C. Driessen, *The effect of magnetic field on the intrinsic detection efficiency of superconducting single-photon detectors*, Appl. Phys. Lett. **106**, 092602, (2015).
- J. J. Renema, Q. Wang, R. Gaudio, I. Komen, K. op't Hoog, D. Sahin, A. Schilling, M. P. van Exter, A. Fiore, A. Engel, and M. J. A. de Dood, *Position-dependent local detection efficiency in a nanowire superconducting single-photon detector*, Nano Lett. **15**, 4541, (2015). (Chapter 3 of this thesis).
- Q. Wang, J. J. Renema, A. Engel, M. P. van Exter, and M. J. A. de Dood, *Local detection efficiency of a NbN superconducting single photon detector explored by a scattering scanning near-field optical microscope*, Opt. Express **23**, 24873, (2015). (Chapter 7 of this thesis).
- Q. Wang, J. J. Renema, A. Gaggero, F. Mattioli, R. Leoni, M. P. van Exter, and M. J. A. de Dood, *How noise affects quantum*

- detector tomography*, accepted for publication by J. Appl. Phys. (Chapter 2 of this thesis).
- **Q. Wang**, et al., *Optimal design of NbN superconducting single photon detectors*, (in preparation for publication, Chapter 4 of this thesis).
  - Conference proceedings
    - **Q. Wang**, S. Qu, S. Li, C. Wang, and X. Xu, *Improvement of internal efficiency of InGaN QWs with asymmetrical quantum barriers*, The 7th International Forum on Solid State Lighting, Shenzhen, China (2010).
    - **Q. Wang**, J. J. Renema, G. Frucci, Z. Zhou, A. Gaggero, F. Mattioli, R. Leoni, A. Fiore, M. P. van Exter, and M. J. A. de Dood, *Accurate characterization of a superconducting nanowire single photon detector*, QOT\_OR\_006, NEW-RAD 2014, Helsinki, Finland, (2014).
    - **Q. Wang**, and M. J. A. de Dood, *Near-field single-photon detection in a scattering SNOM*, proceeding 9504-2, SPIE Optics + Optoelectronics, Prague, Czech Republic, (2015). (Chapter 6 of this thesis).
  - Patents:
    - *A LED with an electron-blocking layer including gradual Al component*, Publication No.: CN102820394A, (2012).
    - *A method of fabricating high quantum efficient GaN LEDs with AlInN quantum barrier*, Publication No.: CN102738340A, (2012).

# Curriculum vitae

Qiang Wang was born on the 15th of October 1985 in Dezhou, China. He graduated from Yucheng No.1 Middle School in 2004 and went on to study physics at the School of Physics of Shandong University. In July 2008, he obtained his BSc diploma after submission of a bachelor thesis "*Study of SiO<sub>2</sub> thin film deposited by PECVD*". He then joined the research group of Prof. Xiaobo Hu for a master program at the Institute of Crystal Materials of Shandong University. In July 2011, he obtained his MSc degree with the thesis titled "*Study of the polarization effect in GaN LEDs*". In August 2011, he started his PhD research at the Leiden Institute of Physics, Leiden University in the Netherlands on near-field optics with superconducting single-photon detectors supervised by Prof. Eric Eliel and Dr. Michiel de Dood. As of November 1 he will work as a postdoctoral researcher in the group of Prof. Andreas Schilling at the University of Zürich.



# Acknowledgement

This thesis would not have been possible without the help from many people. First and foremost, I would like to acknowledge and extend my heartfelt gratitude to my supervisors Michiel de Dood and Eric Eliel. I thank my daily supervisor Michiel for his patient guidance, kind encouragement and invaluable advice. My promotor Eric I thank for his critical reading of every detail through the entire thesis and for many constructive comments.

Secondly, my special thanks go to my colleagues: I thank Jelmer Renema for his extensive knowledge and important contributions to the measurements described in Chapter 3. I thank Martin van Exter for many insightful discussions. I also thank Marc van Kralingen, Bob Rengeling and Irina Komen for inspiring discussions. I want to say many thanks to all the Quantum Optics group members for all the wide-ranging discussions during the group seminars.

For coworkers at TU Eindhoven, I owe much gratitude to Rosalinda Gaudio for her conscientious efforts on sample preparation. Many thanks go to Döndü Sahin for discussions on the optical properties of NbN. I thank Andrea Fiore, Zili Zhou and Saeedeh Jahanmirinejad for useful discussions on my research and Alessandro Gaggero, Francesco Mattioli and Roberto Leoni from CNR-IFN Rome for sample preparation. Chapters 3, 4 and 7 would not be possible without the calculations from Andreas Engel from the University of Zürich.

At LION, I thank Henriette van Leeuwen for her secretarial work. I express my appreciation to Fred Schenkel, Emiel Wieggers, Arno van Amersfoort, Raymond Koehler, Rene Overgaw, Marcel Hesselberth and Daan Boltje for their efforts to solve all the technical problems efficiently. I would also like to thank Stefano Voltan and Klara Uhlírova for their guidance on the PPMS.

I thank Dapeng Ding, Shuo Mi, Ke Liu, Lei Hou, Yujie Zhou and Mengzi Huang for many inspiring discussions on fundamental physics problems.

I thank Cora Tu, Yu Dong, Her Gao and all my friends in Leiden for their sincere concern. I thank Jianfei Yang, Shaoying Wang, Mingsheng Xu, Zhaozhen Shao and Jian Qi for their genuine encouragement.

Last but not least, my thanks also go to my beloved parents and elder sister for their boundless love and whole-hearted support over all the past years.

